Spin Asymmetry in Muon-Deuteron Deep Inelastic Scattering on a Transversely Polarized Target

Dissertation der Fakultät für Physik

der

Ludwig-Maximilians-Universität München

vorgelegt von

Latchezar Betev

aus

Sofia, Bulgarien

München, den 17 Mai 2002

Spin Asymmetry in Muon-Deuteron Deep Inelastic Scattering on a Transversely Polarized Target

Dissertation der Fakultät für Physik

der

Ludwig-Maximilians-Universität München

vorgelegt von

Latchezar Betev

aus

Sofia, Bulgarien

München, den 17 Mai 2002

Erstgutachter: Prof.Dr. Arnold Staude

Zweitgutachter: Prof.Dr. Martin Faessler

Tag der mündlichen Prüfung: 22 Juli 2002

Ludwig-Maximilians-Universität München

Faculty of Physics

Spin Asymmetry in Muon-Deuteron Deep Inelastic Scattering on a Transversely Polarized Target

Dissertation

submitted by

Latchezar Betev

from

Sofia, Bulgaria

supervised by

Prof. Dr. Arnold Staude

May 2002

Kurzfassung

Das wissenschaftliche Ziel der Spin-Myon-Kollaboration (SMC) war die genaue Messung der spinabhängigen Strukturfunktionen g_1^p und g_1^d von Proton bzw. Deuteron durch tiefinelastische Streuung longitudinal polarisierter Myonen an longitudinal polarisierten Wasserstoff- und Deuteriumtargets. SMC setzte das Programm seiner Vorgängerin, der Europäischen Myon-Kollaboration (EMC), die die Strukturfunktion g_1^p maß, fort und erweiterte es. Das Ziel der SMC war nicht nur, die Strukturfunktionen für einen größeren kinematischen Bereich in x und Q^2 zu bestimmen, sondern auch, die systematischen Unsicherheiten erheblich zu verringern. Eine von ihnen wird durch die transversale Spinasymmetrie A_2 hervorgerufen, die in die Berechnung der Strukturfunktion g_1 eingeht:

$$g_1 = \frac{F_1}{1 + \gamma^2}(A_1 + \gamma A_2),$$

wobei F_1 eine unpolarisierte Strukturfunktion und A_1 die von SMC gemessene longitudinale Spinasymmetrie sind. Der Wert von γ ist durch die Kinematik gegeben. In früheren Analysen, solange A_2 unbekannt war, wurde g_1 unter Vernachlässigung von A_2 berechnet und anschließend, bei der Bestimmung des ersten Momentes $\Gamma_1 = \int g_1(x)\mathrm{d}x$ der Strukturfunktion, wurde dies durch einen systematischen Fehler berüchsichtigt, der sich aus dem maximal möglichen Beitrag des Terms γA_2 ergab. Eine Grenze für A_2 folgt aus der Positivitätsbedingung $|A_2| \leq \sqrt{R}$, wobei $R = \sigma_L/\sigma_T$ das Verhältnis von longitudinalem zu transversalem Photonabsorptionswirkungsquerschnitt ist.

Die Vernachlässigung von A_2 in der Berechnung des ersten Momentes Γ_1 war eine der größten Quellen für die systematische Unsicherheit des Experimentes. Um diese Situation zu verbessern, führte SMC eine Messung von A_2 mit longitudinal polarisiertem Strahl und transversal polarisiertem Target für das Proton (A_2^p) und das Deuteron (A_2^d) durch. Die vorliegende Dissertation hat die Messung von A_2^d zum Inhalt. Sie behandelt auch Verbesserungen am Apparat, die zu einer besseren zeitlichen Stabilität führten. Davon profitierten alle Messungen, auch die von g_1.

Die Analyse zeigt, daß die Asymmetrie A_2^d viel kleiner als ihre Positivitätsgrenze ist, sie ist sogar im ganzen untersuchten x-Bereich $0.0015 \leq x \leq 0.6$ mit Null veträglich. Ein Vergleich mit der Messung des E-143-Experimentes, das A_2^d für $0.03 \leq x \leq 0.8$ bestimmte, zeigt gute Übereinstimmung im Überlappungsbereich der x-Regionen. Beide Datensätze wurden deshalb kombiniert und zu einem gemeinsamen Q_0^2 extrapoliert, um den Beitrag von A_2^d zum ersten Moment der Strukturfunktion g_1^d zu berechnen.

Die hier dargestellte Messung verringert die durch die Vernachlässigung von A_2^d hervorgerufene Unsicherheit von Γ_1^d um einen Faktor 2 - von 0.0025 auf 0.0011 (der Fehler durch allen anderen Quellen ist 0.0036). Sie erlaubt auch Aussagen über die spinabhängige Strukturfunktion g_2^d, die ihrerseits über Quark-Gluon-Korrelationen im Nukleon informiert. Die Ergebnisse sind vereinbar mit dem Wandzura-Wilczek-Modell für g_2 und geben Grenzen - allerdings keine strengen, wegen der begrenzten statistischen Genauigkeit der Messung, - für verschiedene Summenregeln für das erste Moment Γ_2 von g_2, nämlich der von Burkhardt und Cottingham sowie der von Efremov, Leader und Teryaev.

Abstract

The scientific goal of the Spin Muon Collaboration (SMC) was to measure with high precision the spin-dependent structure functions g_1^p of the proton and g_1^d of the deuteron through deep inelastic scattering of longitudinally polarized muons off longitudinally polarized hydrogen and deuteron targets. SMC followed and expanded the programme of its predecessor, the European Muon Collaboration (EMC), which measured the structure function g_1^p.

The SMC goal was not only to evaluate the structure functions over a broader kinematical range in x and Q^2, but also to substantially decrease the systematic uncertainties. One of them arises from the contribution of the transverse spin asymmetry A_2, which enters in the calculation of the structure function g_1 through:

$$g_1 = \frac{F_1}{1 + \gamma^2}(A_1 + \gamma A_2)$$

where F_1 is an unpolarized structure function and A_1 the longitudinal spin asymmetry, measured by SMC. The value of γ is determined by kinematics.

In previous analyses, until A_2 remained unknown, the evaluation of g_1 was performed neglecting A_2 and subsequently, in the calculation of the first moment of the structure function $\Gamma_1 = \int g_1(x)\mathrm{d}x$, this was cited as a systematic error, computed for the maximum possible contribution from the term γA_2. The limits on A_2 are set by the existing positivity condition $|A_2| \leq \sqrt{R}$, where $R = \sigma_L/\sigma_T$ is the ratio of longitudinal to transverse photon absorption cross-section.

The neglect of A_2 in the evaluation of the first moment Γ_1 was one of the biggest sources of systematic uncertainty in the experiment. To improve this situation, SMC performed a measurement of A_2 with longitudinally polarized beam and transversely polarized target for proton (A_2^p) and for deuteron (A_2^d). This thesis covers the measurement of A_2^d. It also covers improvements done to the apparatus, which resulted in a better time stability. From this all measurements profited, also that of g_1.

The analysis shows, that the asymmetry A_2^d is much smaller than its positivity bound and is compatible with zero throughout the measured interval in x: $0.0015 \leq x \leq 0.6$. A comparison with the results of the E143 experiment, which measured A_2^d for $0.03 \leq x \leq 0.8$ display a good agreement in the overlapping x region. Both sets of data, combined together and scaled to a common Q_0^2, are used to estimate the contribution of A_2^d to the first moment of the structure function g_1^d.

The presented measurement reduces the systematic uncertainty on Γ_1^d, due to the neglect of A_2^d, by a factor of 2 - from 0.0025 to 0.0011, while the combined error from all other sources is 0.0036. It also provides information for the spin dependent structure function g_2^d, which carries information about the quark-gluon correlations in the nucleon. The results are compatible with the Wandzura-Wilczek model for g_2 and give weak bounds, due to the limited statistical accuracy of the measurement, for several sum rules for the first moment of g_2, Γ_2, namely the Burkhardt-Cottingham sum rule and the Efremov-Leader-Teryaev sum rule.

Contents

1 Nucleon spin structure in DIS

1.1 Introduction

For the past 30 years deep inelastic lepton-nucleon scattering (DIS) proved to be one of the most important experimental methods to study the internal structure of the nucleon. The first experiment at the Stanford Linear Accelerator (SLAC) [1] in 1969 with an electron beam of 20 GeV found evidence of the scale invariance of the experimental cross-section of the nucleon, an effect predicted by Bjorken [2] on the basis of the parton model. The pointlike objects 'partons' off which the electrons scattered were later postulated as quarks by Gell-Mann and Zweig [3]. Since the early days, DIS experiments have provided a substantial amount of data on the internal structure of the nucleon, covering a broad kinematical range and providing high statistical precision and sometimes unexpected results. One example is the measurement of the spin-dependent structure function g_1 of the proton, carried out by the European Muon Collaboration (EMC) in the mid 1980's.

Existing theoretical predictions based on the quark-parton model, notably the Ellis-Jaffe sum rule [4], implied that the nucleon spin is carried by the valence (u, d) quarks and the quark sea polarization is negligible. The EMC data on g_1^p showed a violation of this sum rule, and within the errors the valence quarks contribution to the nucleon spin was consistent with zero. This surprising result prompted further theoretical and experimental effort. A decomposition of the nucleon spin content, stemming from the perturbative QCD, accounts in addition to the quark spin $\Delta\Sigma$ the contributions from gluon spin Δg and quark $< L_q >$ and gluon $< L_g >$ orbital angular momenta:

$$S_z = \frac{1}{2}\Delta\Sigma + < L_q > + \Delta g + < L_g > = \frac{1}{2} \tag{1.1}$$

According to recent theoretical models [9,10,11] the large discrepancy between the findings of EMC and the Quark Parton Model (QPM) predictions may be explained by a gluon spin contribution to the nucleon spin. The models are tested with data collected by several experiments: at SLAC - E-142 [7], E-143 [8] and E-154 - using polarized electron beams with energies from 9 to 48 GeV and polarized proton, deuteron and neutron targets, at CERN - SMC - using polarized muon beam with energies of 100 and 190 GeV and polarized proton and deuteron targets and at DESY - HERMES - with polarized positron beam with energy of 28 GeV and polarized proton and neutron targets. These complementary experiments provide high precision data on the spin-dependent structure functions g_1^p, g_1^n and g_1^d. The measurement of g_1^n and g_1^d permitted for the first time to verify experimentally another fundamental theoretical prediction, the Bjorken sum rule,

which derives the value of the difference of the first moments of g_1^p and g_1^n: $\Gamma_1^p - \Gamma_1^n$ in the framework of perturbative QCD (pQCD), making only very general assumptions. Verification of this sum rule is considered to be a major direct test of pQCD.

Deep inelastic scattering with polarized leptons and nucleons is described by the spin-dependent structure functions g_1, which carries information on the longitudinal quark spin distribution and g_2 which, in combination with g_1, carries information on the transverse quark spin distribution. While the initial physics goal of the SMC experiment was to measure g_1, a short period of the data taking in 1995 was devoted to a measurement of the virtual photon-nucleon asymmetry A_2 for deuteron, related to g_2^d and also entering in the calculation of g_1^d. This thesis concentrates on the gathering and analysis of the data obtained on A_2^d and the implication of the result on the structure function g_1^d and its first moment Γ_1^d. It is organized in 5 chapters and an appendix. The first chapter includes theoretical background relevant to the analysis, including principles and variables used to define deep inelastic scattering, a short overview of the theoretical methods used to calculate the cross-sections of the process and the sum rules for the nucleon structure functions. The second chapter contains the description of the SMC apparatus: polarized target, spectrometer and beam polarimeter and the methods applied for the beam polarization measurements. Chapter three deals with specifics of the data analysis software, its parameters and tuning. The formalism and the experimental methods, used to extract and evaluate the spin asymmetry A_2 are introduced in chapter four. The fifth chapter contains the results, interpretation and impact on the evaluation of g_1^d and Γ_1^d. The appendix contains a description of an efficiency stabilization system for two of the detector groups in the SMC spectrometer.

1.2   Deep Inelastic Scattering (DIS)

1.2.1   Kinematic variables

The SMC experiment studies the internal spin structure of the nucleon through the process of deep inelastic scattering of high energy polarized muons off polarized target nucleons. The analysis regards only the inclusive process, where the final hadron state is not measured. At leading order, the cross-section in DIS has contributions from a single photon exchange (electromagnetic interaction) and a Z^0 vector boson exchange (weak interaction). At the momentum transfers of the SMC experiment, the contribution from Z^0 exchange to the cross-section is suppressed by its high mass ($Q^2 << M_Z^2$), therefore we shall only discuss DIS in the limit of one photon exchange (Fig.1.1).
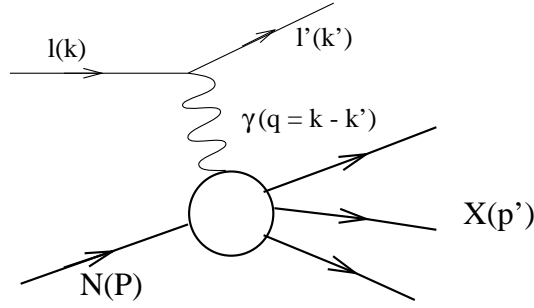
Figure 1.1: *One photon exchange diagram of deep inelastic lepton-nucleon scattering.*

Here $k = (E, \vec{k})$, $k' = (E', \vec{k'})$, $q = (\nu, \vec{q})$ are the four momenta of the incoming lepton, scattered lepton and exchanged virtual photon, respectively. Initial nucleon and final hadron state have the four momenta $P = (M, \vec{0})$ and $p' = (M + \nu, \vec{q})$. It is convenient to construct the following Lorentz invariants, using these variables and the nucleon mass M:

$$Q^2 = -q^2 = (k - k')^2 \overset{lab}{=} 4EE' \sin^2 \frac{\Theta}{2} \tag{1.2}$$

is the modulus of the squared four momentum transfer of the virtual photon and Θ is the lepton scattering angle in the laboratory system. In this equation the lepton mass is neglected with respect to $\sqrt{Q^2}$, E and E'.

$$\nu = \frac{Pq}{M} \overset{lab}{=} E - E' \tag{1.3}$$

is the exchanged energy or the energy of the virtual photon, and

$$W^2 = (P + q)^2 = M^2 + 2M\nu - Q^2 \tag{1.4}$$

is the squared invariant mass of the hadronic final state X.
The cross-section, introduced in the next section, can also be expressed as a function of

two dimensionless scaling variables x and y, $0 \leq x, y \leq 1$:

$$x = \frac{Q^2}{2Pq} \overset{lab}{=} \frac{Q^2}{2M\nu} \tag{1.5}$$

$$y = \frac{Pq}{Pk} \overset{lab}{=} \frac{\nu}{E}, \tag{1.6}$$

where x is the Bjorken scaling variable and y is the relative energy transfer of the lepton to the nucleon.

The regime of deep inelastic scattering is characterized by $Q^2 >> \Lambda_{QCD}^2$ [1] and the invariant mass of the hadronic final state W above the region of the nucleon resonances, $W \geq 2.5\ GeV$.

1.2.2   Lepton-nucleon scattering cross-section

In the one photon exchange approximation the Born cross-section for inclusive lepton-nucleon scattering can be expressed as a product of a leptonic tensor $l^{\mu\nu}$ and a hadronic tensor $W_{\mu\nu}$:

$$\frac{d^2\sigma}{dx\,dy} = \frac{\alpha^2}{Q^4} \frac{y}{2} l^{\mu\nu} W_{\mu\nu}, \tag{1.7}$$

where $\alpha(=1/137)$ is the electromagnetic fine-structure constant. The leptonic tensor describes the lepton-photon interaction (upper vertex in Fig.1.1) and can be calculated exactly using the Feynman rules of QED [12,13]. Upon summation over the lepton spin in the final state it is given by:

$$l^{\mu\nu} = 2\left(k^\mu k'^\nu + k^\nu k'^\mu - g^{\mu\nu}(k\,k' - m_l^2) + im_l\epsilon^{\mu\nu\alpha\beta}q_\alpha s_{l\beta}\right), \tag{1.8}$$

where m_l is the lepton mass, $g^{\mu\nu}$ is a metric tensor and $\epsilon^{\mu\nu\alpha\beta}$ is the fully antisymmetric Levi-Civita tensor. The term containing the lepton spin $s_{l\beta}$ is the only term which is anti-symmetric in the indices μ and ν. Therefore $l^{\mu\nu}$ is a sum of symmetric and antisymmetric terms and only the last one contains the spin dependence of the tensor.

The hadronic tensor calculation is more complicated due to the unknown nucleon structure. In its most general form [14], constructed from the four vectors P^μ, q^μ and S^μ, where P and q are the four-moments of the nucleon and the virtual photon and S is the nucleon polarization vector, it is under the assumption of P and T invariance:

$$W_{\mu\nu} = \frac{1}{4\pi} \sum_X (2\pi)^4 \delta^4(P + q - p_X)\langle P, S|J_\mu(0)|X\rangle\langle X|J_\nu(0)|P, S\rangle$$

$$= \frac{1}{4\pi} \int d^4z e^{iq\cdot z}\langle P, S|[J_\mu(z), J_\nu(0)]|P, S\rangle \tag{1.9}$$

In the second step of the equation, after summation over X, the tensor exhibits independence over the final hadronic state. The space-time interval z determines the scale of the distance probed in deep inelastic scattering, between the points where the hadronic currents J_μ, J_ν act.

---

[1] the hadronic mass scale $\Lambda_{QCD} \approx 300\ MeV$

Similarly to the leptonic tensor, $W_{\mu\nu}$ can be split into spin independent (symmetric) and spin dependent (antisymmetric) part. Furthermore, it can be parametrized [15,16,17] by two unpolarized (F_1, F_2) and two polarized (g_1, g_2) dimensionless structure functions. For the case of spin $\frac{1}{2}$ it reads:

$$W_{\mu\nu} = -\left(g_{\mu\nu} - \frac{q_\mu q_\nu}{q^2}\right)F_1 + \left(P_\mu - \frac{(Pq)q_\mu}{q^2}\right)\left(P_\nu - \frac{(Pq)q_\nu}{q^2}\right)\frac{F_2}{Pq}$$

$$- i\epsilon_{\mu\nu\alpha\beta}q^\alpha\left(\frac{MS^\beta}{Pq}(g_1 + g_2) - \frac{M(Sq)P^\beta}{Pq}g_2\right) \tag{1.10}$$

The first two terms in the equation represent the symmetric part of the tensor, which is spin independent and the third is the antisymmetric part, which is spin dependent.
Finally, the differential cross-section can be expressed as a spin-average part by the symmetric (indice S) and a spin-dependent part by the antisymmetric (indice A) tensors:

$$\frac{\mathrm{d}^2\sigma}{\mathrm{dx\,dy}} = \frac{\alpha^2}{Q^4}\frac{y}{2}\left(l^{\mu\nu}_{(S)}W_{\mu\nu(S)} - l^{\mu\nu}_{(A)}W_{\mu\nu(A)}\right). \tag{1.11}$$

There are no cross-terms with only lepton or only nucleon spin, therefore spin dependent effects can be studied only if both the lepton and the nucleon are polarized.
It is convenient to express the cross-section using the Lorentz invariant kinematic variables introduced in section 1.2.1. In the following formalism, we will consider a fully polarized target nucleon and a longitudinally polarized incoming lepton. Denoting with $\bar\sigma$ the spin independent part of the total cross-section, $\sigma_\parallel$ the spin dependent part of the cross-section for longitudinal nucleon spin orientation and $\sigma_\perp$ the spin dependent part of the cross-section for transverse nucleon spin orientation, the differential cross-section reads:

$$\frac{\mathrm{d}^2\sigma}{\mathrm{dx\,dQ^2}} = \frac{\mathrm{d}^2\bar\sigma}{\mathrm{dx\,dQ^2}} - H_l\cos\psi\frac{\mathrm{d}^2\Delta\sigma_\parallel}{\mathrm{dx\,dQ^2}} - H_l\sin\psi\cos\phi\frac{\mathrm{d}^2\Delta\sigma_\perp}{\mathrm{dx\,dQ^2}}, \tag{1.12}$$

where H_l is the lepton helicity, ϕ is the azimutal angle between the scattering plane and the plane containing the lepton and target spin ($-\pi \leq \phi \leq \pi$), ψ is the angle between the incoming lepton momentum and the target spin ($0 \leq \psi \leq \pi$) (see Fig.1.2(a)). The notation $\Delta\sigma_\parallel$ refers to the difference of the cross-sections for nucleon spin parallel or antiparallel to the lepton spin, $\Delta\sigma_\perp$ to the difference of the cross-section the nucleon spin orthogonal to the lepton spin and angles ϕ and $\pi - \phi$ respectively (see Fig.1.2(b)). The spin independent part of the cross-section as a function of the unpolarized structure functions $F_1(x,Q^2)$ and $F_2(x,Q^2)$ is given by:

$$\frac{\mathrm{d}^2\bar\sigma}{\mathrm{dx\,dQ^2}} = \frac{4\pi\alpha^2}{Q^4 x}\left(xy^2F_1(x,Q^2) + (1 - y - \frac{\gamma^2 y^2}{4})F_2(x,Q^2)\right). \tag{1.13}$$

The kinematic factor $\gamma = \frac{\sqrt{Q^2}}{\nu} = \frac{2Mx}{\sqrt{Q^2}}$ is small for high energy experiments, since either Q^2 is large or x is small [1].

---

[1] for the SMC experiment with beam energy $E_\mu = 190~GeV$ the central value of γ is 0.008
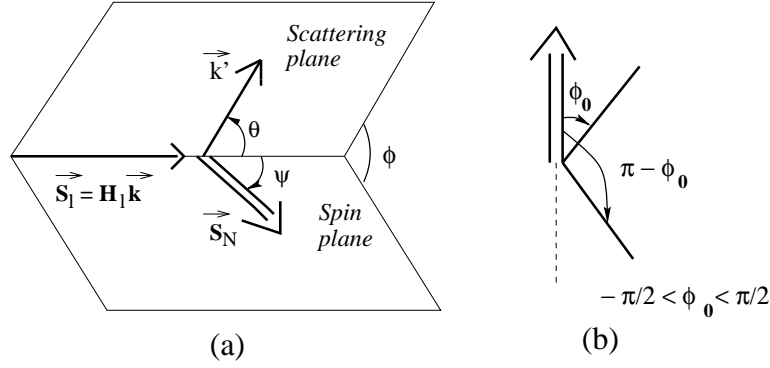
Figure 1.2: *(a) Kinematic variables for deep inelastic lepton-nucleon scattering on a fixed polarized nucleon target. (b) Definition of the azimutal angle $\phi = \phi_0$ and $\phi = \pi - \phi_0$ for evaluation of cross-section $\Delta\sigma_\perp$.*

The structure functions $F_2(x, Q^2)$ and $F_1(x, Q^2)$ are related through

$$F_1(x, Q^2) = F_2(x, Q^2) \frac{(1 + \gamma^2)}{2x(1 + R(x, Q^2))} \qquad (1.14)$$

which is the extended Callan-Gross relation ($2xF_1 = F_2$) [18], involving the ratio $R = \sigma_L/\sigma_T$ of the photon-nucleon absorption cross-sections σ_L and σ_T for longitudinally and transversely polarized photons.

From Eq.1.12 it is evident, that experimentally the cross-section $\Delta\sigma_\parallel$ can be studied by: (a) measuring it for $H_l = \pm 1$ and keeping the nucleon spin in parallel or antiparallel direction, or (b) for a fixed lepton helicity, change the nucleon spin between $\psi = 0$ and $\psi = \pi$. For practical reasons, SMC uses the second method, for which the differential cross-section as a function of the structure functions g_1 and g_2 is reduced to:

$$\frac{d^2\Delta\sigma_\parallel}{dx\, dQ^2} = \frac{8\alpha^2 y}{Q^4} \left((1 - \frac{y}{2} - \frac{\gamma^2 y^2}{2}) g_1(x, Q^2) - \frac{\gamma^2 y}{2} g_2(x, Q^2) \right). \qquad (1.15)$$

The structure function $g_1(x, Q^2)$ can be extracted from this relation, since the contribution from $g_2(x, Q^2)$ to the cross-section is highly supressed by the factor γ^2.

$\Delta\sigma_\perp$ is measured with nucleon spin orthogonal to the lepton spin ($\psi = \frac{\pi}{2}$) as a difference between the cross sections at angles $\phi = \phi_0$ and $\phi = \pi - \phi_0$ [1] and expressed in terms of g_1 and g_2 is:

$$\frac{d^2\Delta\sigma_\perp}{dx\, dQ^2} = \frac{8\alpha^2 y}{Q^4} \gamma \sqrt{1 - y - \frac{\gamma^2 y^2}{4}} \left(\frac{y}{2} g_1(x, Q^2) - g_2(x, Q^2) \right) \qquad (1.16)$$

In this equation both spin dependent structure functions enter with similar weight, therefore g_2 can be extracted only after g_1 has been determined. $\Delta\sigma_\perp$ itself is suppressed by the factor γ and its contribution to the spin dependent cross-section is small.

---

[1] Two other methods exist, as discussed in section 4.4, but this one is the best from experimental point of view.

6

1.2.3 Forward Compton scattering, helicity amplitudes.

A physical interpretation of the structure functions, defined in the previous section, can be obtained by the introduction of helicity amplitudes for virtual photon-nucleon Compton scattering. The hadronic tensor $T_{\mu\nu}$ describing the Compton scattering of a virtual photon on a nucleon has the same symmetry properties as $W_{\mu\nu}$ and can be parametrized, using similar structure functions. The Optical theorem formally relates the two tensors [21]:

$$W_{\mu\nu} = \frac{1}{\pi} Abs(T_{\mu\nu}), \tag{1.17}$$

where Abs stands for the absorptive part of the Compton amlitude.

The Compton scattering is represented by $\gamma_h + N_H \rightarrow \gamma_{h'} + N_{H'}$ where h and H are the helicities of the photon and the nucleon in the initial state and h' and H' are the helicities in the final state, projected along the incident lepton direction. The tensor $T_{\mu\nu}$ contracted with the photon polarization vectors $\epsilon_{h'}^{\mu}$ and ϵ_h^{ν} gives the helicity amplitudes $\mathcal{A}_{h,H;h',H'} = \epsilon_{h'}^{\mu} \epsilon_h^{\nu} T_{\mu\nu}$. Due to parity, current and angular momentum conservation, only four of the amplitudes are independent [22]:

$$\sigma_T^{\frac{1}{2}} \sim \quad \mathcal{A}_{+1,-\frac{1}{2};+1,-\frac{1}{2}} \quad = F_1 + g_1 - \gamma^2 g_2$$

$$\sigma_T^{\frac{3}{2}} \sim \quad \mathcal{A}_{+1,+\frac{1}{2};+1,+\frac{1}{2}} \quad = F_1 - g_1 + \gamma^2 g_2$$

$$\sigma_L^{\frac{1}{2}} \sim \quad \mathcal{A}_{0,+\frac{1}{2};0,+\frac{1}{2}} \quad = -F_1 + \frac{(1+\gamma^2)F_2}{2x}$$

$$\sigma_{TL}^{\frac{1}{2}} \sim \quad \mathcal{A}_{+1,-\frac{1}{2};0,+\frac{1}{2}} \quad = \gamma(g_1 + g_2) \tag{1.18}$$

where $\frac{1}{2}$ and $\frac{3}{2}$ denote the total angular momenta of the photon-nucleon system along the incoming lepton direction. The indices in $\mathcal{A}_{i,j;i',j'}$ stand for initial and final photon polarization (i, i') and initial and final target polarization (j, j'). The first two cross-sections are the absorption cross-sections for transversely polarized virtual photons (T), the third one is for longitudinally polarized virtual photons (L) and the last is the interference (TL) cross-section, which changes the photon helicity. The total transverse cross-section σ_T is entirely determined by F_1:

$$\sigma_T = \frac{1}{2}(\sigma_T^{1/2} + \sigma_T^{3/2}) = cF_1, \tag{1.19}$$

where $c = \frac{4\pi\alpha}{MK}$ and $K = \nu - Q^2/2M$. σ_L is the absorption cross-section of the longitudinaly polarized virtual photon and σ_{TL} describes the interference between an incoming photon with transverse polarization and an outgoing photon with longitudinal polarization.

Two virtual photon-nucleon asymmetries are of interest for the analysis and can be formally related to the cross-section, defined in 1.18 and the structure functions F_1, F_2, g_1 and g_2:

$$A_1 = \frac{\sigma_T^{1/2} - \sigma_T^{3/2}}{\sigma_T^{1/2} + \sigma_T^{3/2}} = \frac{1}{F_1}(g_1 - \gamma^2 g_2) \qquad A_2 = \frac{\sigma_{TL}}{\sigma_T} = \frac{\gamma}{F_1}(g_1 + g_2) \tag{1.20}$$

7

The asymmetry A_1 is directly related to the structure function g_1, since the contribution from g_2 is highly supressed by the γ^2. The interpretation of g_2 is not so straightforward, since it depends on the cross-section σ_{TL}, which describes a process involving absorption of photon with helicity $+1$ by a quark with helicity $-\frac{1}{2}$. This causes a helicity flip of the quark and emission of a helicity 0 photon. The process violates the helicity conservation law for massless fermions. Mechanisms, which permit this process, without violating conservation laws, are discussed later is the section.

The following positivity constraints are fullfilled by A_1 and A_2:

$$|A_1| \leq 1 \tag{1.21}$$

$$|A_2| \leq \sqrt{R} \tag{1.22}$$

1.21 is derived from $|\sigma_T^{1/2} - \sigma_T^{3/2}| \leq \sigma_T^{1/2} + \sigma_T^{3/2}$ and 1.22 from $|\sigma_{TL}| \leq \sqrt{\sigma_T \sigma_L}$ [24].

Generalization for spin-1 targets

The helicity amplitudes and asymmetries defined in the previous section are valid for a spin-$\frac{1}{2}$ target. In case of spin-1 nucleon target, the helicity amplitudes are eight, and consequently there are four more inclusive structure functions: b_1 b_2 b_3 and b_4. They contribute to the symmetric part of $W_{\mu\nu}$, therefore they can be measured with an unpolarized lepton beam. It is shown in [17] that in the limit of DIS the structure functions b_2, b_3 and b_4 can be neglected, since b_3 and b_4 are suppressed by a factor M/Q. b_2 is defined as $b_2 = 2xb_1 + \mathcal{O}(M^2/Q^2)$ and b_1 is expected to be very small. The total transverse and longitudinal cross-sections take the form:

$$\sigma_T = \sigma_T^0 + \sigma_T^1 + \sigma_T^2 \qquad\qquad \sigma_L = 2\sigma_L^1 + \sigma_L^0 \tag{1.23}$$

The indices 0, 1 and 2 denote the initial angular momentum of the photon-hadron system in the incoming lepton direction. It is equal to the final angular momentum due to angular momentum conservation.

The virtual photon absorption asymmetries A_1 and A_2 are given by:

$$A_1 = \frac{3}{2}\frac{\sigma_T^0 - \sigma_T^2}{\sigma_T} \qquad\qquad A_2 = \frac{3}{2}\frac{\sigma_{TL}^0 - \sigma_{TL}^1}{\sigma_T} \tag{1.24}$$

In the limit of $b_{1-4} = 0$ the relations between the asymmetries in Eq.1.24 and the structure functions g_1 and g_2 are the same as in Eq.1.20, therefore the method of extraction of the structure functions is equivalent for both, spin-$\frac{1}{2}$ and spin-1 targets [23].

The deuteron bound state

In the present analysis the deuteron is treated as an incoherent sum of one proton and one neutron, since the scattering occurs on partons and not on a nucleus. Nuclear effects, such as shadowing and anti-shadowing are neglected. The deuteron has a wave function dominated by the S-state (orbital angular momentum $L = 0$) for which the spins of the proton and the neutron are parallel to the spin of the deuteron. There is a small D-state

admixture ($L = 2$) for which the nucleon spins are antiparallel to the deuteron spin. The following relation takes into account the correction for the D-state:

$$g_1^p + g_1^n = \frac{2g_1^d}{1 - \frac{3}{2}\omega_D} \tag{1.25}$$

where ω_D is the D-state probability. The factor $\frac{3}{2}$ is a combination of several Clebsch-Gordon coefficients. The value of the probability $\omega_D = 0.05 \pm 0.01$ has been determined in [25].

1.2.4 Cross-section asymmetries

Experimentally, the measurement of the spin dependent cross-section differences $\Delta\sigma_\parallel$ and $\Delta\sigma_\perp$ by a straightforward determination of cross-sections is difficult since they are small compared to the spin independent cross-section $\overline{\sigma}$. Far easier is to determine the longitudinal $A_\parallel$ and transverse $A_\perp$ cross-section asymmetries, defined as:

$$A_\parallel = \frac{\Delta\sigma_\parallel}{2\overline{\sigma}} = \frac{1}{2}\frac{\sigma^{\leftarrow\Rightarrow} - \sigma^{\leftarrow\Leftarrow}}{\sigma^{\leftarrow\Rightarrow} + \sigma^{\leftarrow\Leftarrow}}, \tag{1.26}$$

$$A_\perp = \frac{\Delta\sigma_\perp}{2\overline{\sigma}} = \frac{1}{2\cos\phi_0}\frac{\sigma^{\leftarrow\Uparrow}(\phi_0) - \sigma^{\leftarrow\Uparrow}(\pi - \phi_0)}{\sigma^{\leftarrow\Uparrow}(\phi_0) + \sigma^{\leftarrow\Uparrow}(\pi - \phi_0)}, \tag{1.27}$$

where $\overline{\sigma}$ is the spin-averaged total differential cross-section, $\leftarrow$ and $\Rightarrow$ are the incoming lepton and target polarization orientations respectively. In the SMC experiment the incoming muons have helicity -1 and the asymmetry $A_\parallel$ is measured by inverting the longitudinal target polarization. $A_\perp$ is obtained by comparing event yields in the upper and lower part of the scattering plane and keeping the transverse target polarization orientation fixed.

The cross-section asymmetries for fixed x and Q^2 depend on the beam energy via y, as can be seen from the definition of $\overline{\sigma}$, $\Delta\sigma_\parallel$ and $\Delta\sigma_\perp$ in Eqs.1.13, 1.15, 1.16. It is inconvenient to use them in the data presentation, since different experiments collect data at various beam energies and thus cannot be compared directly. More suitable are the virtual photon absorption asymmetries A_1 and A_2, introduced in section 1.2.3, which are functions of x and Q^2 only.

The relation of the longitudinal and transverse cross-section asymmetries to A_1 and A_2 is given by:

$$A_1 = \frac{1}{1 + \xi\eta}\left(\frac{A_\parallel}{D} - \eta\frac{A_\perp}{d}\right) \qquad A_2 = \frac{1}{1 + \xi\eta}\left(\frac{A_\perp}{d} - \xi\frac{A_\parallel}{D}\right). \tag{1.28}$$

$$A_\parallel = D(A_1 + \eta A_2) \qquad A_\perp = d(A_2 - \xi A_1) \tag{1.29}$$

The kinematic factors ξ and η are defined as follows:

$$\xi = \gamma(1 - \frac{y}{2}) \qquad \eta = \gamma\frac{1 - y}{1 - y/2}. \tag{1.30}$$

D and d are kinematic depolarization factors, which describe the polarization transfer from the incident lepton to the virtual photon and the fact, that the photon does not hit the proton in the direction of its spin. They depend on the angle between the lepton and photon momenta vectors through y and also on R:

$$D = \frac{y(2-y)(1+\frac{\gamma^2 y}{2})}{(1+\gamma^2)y^2 + 2\left(1-y-\frac{\gamma^2 y^2}{4}\right)(1+R)}, \tag{1.31}$$

$$d = \frac{\sqrt{1-y-\frac{y^2\gamma^2}{4}}}{1-\frac{y}{2}}D. \tag{1.32}$$

Most favorable for studying longitudinal spin effects are events with high relative energy transfer y for which $D = 1$ [1], while for transverse spin studies, the optimal region of y is between $0.6 < y < 0.9$, where d has a maximum. d becomes 0 at $y = 1$[1].
The spin-dependent structure functions g_1 and g_2 are related to the virtual photon-nucleon asymmetries through:

$$g_1 = \frac{F_1}{1+\gamma^2}(A_1 + \gamma A_2) \qquad g_2 = \frac{F_1}{1+\gamma^2}(\frac{A_2}{\gamma} - A_1). \tag{1.33}$$

To evaluate g_1 and g_2 both asymmetries have to be measured. Until recently no data was available on A_2 and in the calculations of g_1 this lack of knowledge was taken into account by using the positivity condition on A_2: $|A_2| < \sqrt{R}$. The resulting contribution was treated as a systematic uncertainty. Expressed in terms of the experimentally measurable cross-section asymmetry $A_{\parallel}$, g_1 is:

$$g_1 = \frac{F_1}{1+\gamma^2}\left(\frac{A_{\parallel}}{D} + (\gamma - \eta)A_2\right) \approx \frac{F_1}{1+\gamma^2}\left(\frac{A_{\parallel}}{D}\right) \tag{1.34}$$

At high energies, this approximation is justified, since the contribution of A_2 to g_1 is suppressed by the small kinematic factor $\gamma - \eta$.
In the extraction of the structure function g_2 no such approximation is possible, since in the cross-section of the process both structure functions enter with similar weight (Eq.1.16). Therefore both $A_{\parallel}$ and $A_{\perp}$ have to be measured and g_2 is extracted from:

$$g_2 = \frac{F_1}{(1+\gamma^2)(1+\eta\xi)}\left(\frac{A_{\perp}}{d}(\eta + \frac{1}{\gamma}) - \frac{A_{\parallel}}{D}(1 - \frac{\xi}{\gamma})\right) \tag{1.35}$$

The unpolarized structure function F_1 is evaluated from the extended Callan-Gross relation (Eq.1.14), where the NMC parametrization [19] of F_2 and the SLAC parametrization [20] of R are used.

1.2.5   The Quark-Parton model prediction for g_2

Within the framework of the naive Quark-Parton model [26,27], the nucleon is assumed to be composed of colinear non-interacting quarks, the so-called partons. In this model the structure functions can be expressed as sums of quark distribution functions $q_i(x)$,

---

[1]in the limit of $R = 0$ and $\gamma = 0$

which are functions only of the fraction of the momentum of the nucleon carried by the quark:

$$F_1(x) \;=\; \frac{1}{2} \sum_i^{n_f} e_i^2 \, [q_i^\uparrow(x) + q_i^\downarrow(x) + \bar{q}_i^\uparrow(x) + \bar{q}_i^\downarrow(x)] \tag{1.36}$$

$$F_2(x) \;=\; x \sum_i^{n_f} e_i^2 \, [q_i^\uparrow(x) + q_i^\downarrow(x) + \bar{q}_i^\uparrow(x) + \bar{q}_i^\downarrow(x)] \tag{1.37}$$

$$g_1(x) \;=\; \frac{1}{2} \sum_i^{n_f} e_i^2 \, [q_i^\uparrow(x) - q_i^\downarrow(x) + \bar{q}_i^\uparrow(x) - \bar{q}_i^\downarrow(x)] \tag{1.38}$$

$$g_2(x) \;=\; 0, \tag{1.39}$$

where $q_i^\uparrow(\bar{q}_i^\uparrow)$ and $q_i^\downarrow(\bar{q}_i^\downarrow)$ are the distribution functions of quarks(antiquarks) with spin parallel and antiparallel to the nucleon spin, i runs over all quark flavours and e_i is the quark charge in units of e. In this representation g_2 vanishes, since the masses and the transverse momenta of the quarks are neglected.

Non-zero values for the structure function g_2 can be obtained by allowing the quarks to have an intrinsic transverse momentum $p_\perp$ [31]. In this case g_2 depends on the quark masses m_i and can be written as:

$$g_2(x) = \frac{1}{2} \sum_i^{n_f} e_i^2 \left(\frac{m_i}{xM} - 1 \right) [q_i^\uparrow(x) - q_i^\downarrow(x) + \bar{q}_i^\uparrow(x) - \bar{q}_i^\downarrow(x)]. \tag{1.40}$$

In the limit of the naive QPM $m_i = xM$ one recovers the previous result $g_2 = 0$. The helicity amplitude σ_{TL}, introduced in section 1.2.3 can be expressed in terms of quark distribution functions, using Eq.1.40 and Eq.1.38:

$$\sigma_{TL} \sim g_T(x) = g_1(x) + g_2(x) = \frac{1}{2} \sum_i^{n_f} e_i^2 \, \frac{m_i}{xM} [q_i^\uparrow(x) - q_i^\downarrow(x) + \bar{q}_i^\uparrow(x) - \bar{q}_i^\downarrow(x)], \tag{1.41}$$

where $g_T(x)$ is the structure function in Feynman's derivation of the parton model for transverse spin [32]. The definitions for the quark distribution functions are as above.

A non-zero interference term σ_{TL} resulting from this equation permits a process in which a longitudinally polarized photon is absorbed by a quark, causing its helicity to flip, followed by an emisson of transversely polarized photon. This process does not violate the angular momentum conservation law and has an explicit contribution to the structure function g_2.

A problem in this approach, however, is the extreme sensitivity of g_2 on the assumptions made for the quark mass. Several authors [28,29] claim, that based on Eq.1.41, g_T is small. If the massless limit is taken, one indeed obtains $g_T = 0$. This limit is inconsistent with the nucleon's rest mass. It is consistent to set $m_i = xM$, in which case when applying Eq.1.41 in the nucleon's rest frame, the $g_2(x)$ becomes zero due to rotational invariance, wich leads again to the naive model result (Eq.1.38, 1.39).

Based on such shortcomings of the QPM, [31,33,34] argue, that it is not possible to make purely QPM calculations of g_2 without introducing complicated parton transverse momentum distributions and resolving the contributions to g_2 from the mass operator. At present, there is no nucleon model which treats the transverse spin physics associated with g_2 in a coherent way.

1.2.6 The Operator Product Expansion

Perturbative QCD permits the direct derivation of model-independent sum rules of the structure functions using a parametrization of the hadronic tensor $W_{\mu\nu}$ (Eq.1.9). The method is based on the Wilson's Operator Product Expansion (OPE)[35]. The hadronic tensor is given by the Fourier transform of the nucleon matrix elements of the commutator of electromagnetic currents $J_\mu(z)$:

$$W_{\mu\nu} = \frac{1}{2\pi} \int \mathrm{d}^4z \, \mathrm{e}^{\mathrm{iq}\cdot\mathrm{z}} \langle \mathrm{P}, \mathrm{S} | [\mathrm{J}_\mu(\mathrm{z}), \mathrm{J}_\nu(0)] | \mathrm{P}, \mathrm{S} \rangle \tag{1.42}$$

where S is the covariant spin vector specifying the state of the nucleon with momentum P. Using OPE, the product of the currents $[J_\mu(z), J_\nu(0)]$ can be expressed in the light cone limit $z^2 \to 0$, $Q^2 \to \infty$ [1] as a sum of local operators $\mathcal{O}_i^n(0)$, multiplied by the Wilson's coefficients $C_i'^n(\mathrm{z})$:

$$\lim_{z^2 \to 0} J_\mu(z) J_\nu(0) = \sum_{i,n} C_i'^n(z) \mathcal{O}_i^n(0) \tag{1.43}$$

Substituting this expression in Eq.1.42 yields for the hadronic tensor:

$$W_{\mu\nu} = \frac{1}{2\pi} \int \mathrm{d}^4z \, \mathrm{e}^{\mathrm{iq}\cdot\mathrm{z}} \langle \mathrm{P}, \mathrm{S} | \sum_{\mathrm{i},\mathrm{n}} \mathrm{C}_\mathrm{i}'^\mathrm{n}(\mathrm{z}) \mathcal{O}_\mathrm{i}^\mathrm{n}(0) | \mathrm{P}, \mathrm{S} \rangle$$

$$= \frac{1}{2\pi} \sum_{i,n} C_i^n(Q^2) \langle P, S | \mathcal{O}_i^n(0) | P, S \rangle. \tag{1.44}$$

The Wilson's coefficients, where $C_i^n(Q^2)$ is the Fourier transform of $C_i'^n(z)$, can be calculated, using perturbative QCD. The indices n are the spin of the operators and indices i distinguish different operators of the same spin and take the values $i = 1, 2..., 8, \psi, G$, where $i = 1, 2...., 8$ are flavour non-singlet, $i = \psi, G$ are quark flavour singlet and gluon operators.

In [36] the matrix elements for the non-singlet operators are written in the form:

$$\langle PS | \mathcal{O}_{1,i}^{\sigma\mu_1\ldots\mu_{n-1}} | PS \rangle = \frac{-2a_n^i}{n} [S^\sigma P^{\mu_1}\ldots P^{\mu_{n-1}}]_S \tag{1.45}$$

$$\langle PS | \mathcal{O}_{1,i}^{\lambda\sigma\mu_1\ldots\mu_{n-2}} | PS \rangle = d_n^i (S^\sigma P^\lambda - S^\lambda P^\sigma) P^{\mu_1}\ldots P^{\mu_{n-2}}, \tag{1.46}$$

where the symbol S implies symmetrization and a_n^i, d_n^i are the reduced matrix elements of the operators. Substituted in the expression for the hadronic tensor $W_{\mu\nu}$ the operators give rise to expansion of the order of $(1/q^2)^{t-2}$ where $t = d - n$ is the 'twist' of the related operator and is defined as difference between its mass dimension and spin. The lowest twist operators in QCD have twist-2 (dimension 3, spin 1) and they determine Eq.1.45. Twist-3 operators determine Eq.1.46. It can be shown that only the twist operators with spin n contribute to the n-th moment of the structure function. The resulting equations

---

[1] The equation 1.42 receives contributions from the region, where $q \cdot z$ is finite. In the DIS limit, where $\nu \to large$ and $Q^2 \to large$, while Q^2/ν is finite this implies that $z^2 \sim 1/Q^2$

for the moments of g_1 and g_2 in terms of the factors a_n^i, d_n^i and the coefficient functions $C_{1,i}^n$ for the n-th moment are given by:

$$\int_0^1 dx\ x^{n-1} g_1(x, Q^2) = \frac{1}{2} \sum_i a_n^i(Q^2) C_{1,i}^n(Q^2) \qquad n = 1, 3, 5... \quad (1.47)$$

$$\int_0^1 dx\ x^{n-1} g_2(x, Q^2) = \frac{1-n}{2n} \sum_i \left(a_n^i(Q^2) C_{1,i}^n(Q^2) - d_n^i(Q^2) C_{2,i}^n(Q^2) \right) \quad n = 3, 5, 7... \quad (1.48)$$

where only twist-2 contributions enter in leading order into the moments for g_1 and there are twist-2 and twist-3 contributions in leading order for g_2. For the first moment of g_1 there are exact QCD calculations for the Wilson's coefficients C_1 up to $\mathcal{O}(\alpha_s)^2$ and $\mathcal{O}(\alpha_s)^3$ for the flavour singlet and non-singlet terms [37]. A theoretical study of the coefficients C_2 is made in [36]. Theoretical calculations exist also for the twist-3 matrix elements d_n from QCD sum rules [38,39] and Bag model [40,41]. Those predictions can be tested by evaluating the moments of the structure functions g_1 and g_2.

The gluonic field contributions entering in OPE calculations provide a mechanism in which the spin-flip Compton amplitude σ_{TL} has a non-zero value. It involves coherent parton scattering where a scalar virtual photon flips the momentum and the spin of the quark is flipped by a gluon. In this process both angular momentum and helicity are conserved and no assumptions are made for the quark mass.

1.2.7 Relations and Sum Rules for g_2

The statistical accuracy of the measurement of the structure function g_2, presented in this thesis, is insufficient to prove or disprove any of the currently existing models and sum rules. Furthermore, in different references the validity of the models and the sum rules is questioned on the grounds of the assumptions made in their derivation or the correctness of the approximations made to the different contribution to g_2. Nevertheless, the existing models currently found in the literature are summarized briefly below, without details on their derivation.

Wilczek-Wandzura relation

The relation, presented in [42], is based on the following operator product:

$$\int_0^1 dx\ x^{n-1} \left[g_1(x, Q^2) + g_2(x, Q^2) \right] = \frac{1}{2} \sum_i a_n^i(Q^2) C_{1,i}^n(Q^2) \qquad (1.49)$$

$$+ \frac{n-1}{2n} \sum_i d_n^i(Q^2) C_{2,i}^n(Q^2)$$

under the assumption that it is valid for all integer n. From 1.49 they obtain:

$$g_1(x, Q^2) + g_2(x, Q^2) = \int_x^1 \frac{dt}{t} g_1(t, Q^2) + [twist - 3]. \qquad (1.50)$$

If the structure function g_2 is decomposed into twist-2 and twist-3 components, where g_2^{WW} is the twist-2 component:

$$g_2(x, Q^2) = g_2^{WW}(x, Q^2) + \overline{g_2}(x, Q^2), \qquad (1.51)$$

13

and neglecting the twist-3 term $\overline{g_2}(x, Q^2)$, g_2 becomes completely determined from g_1:

$$g_2^{WW}(x, Q^2) = -g_1(x, Q^2) + \int_x^1 g_1(t, Q^2) \frac{dt}{t}, \tag{1.52}$$

This relation gives a direct connection between g_1 and g_2. Formally, the initial assumption, that eq.1.49 is valid for $n = 1$ is not correct, since the OPE does not give direct information on the first moment of g_2.

[31] argue, that the correct way to treat 1.47 and 1.48 is in the limits of OPE - for $n \geq 3$, which yields an equation for the twist-3 contributions to the structure functions:

$$\int_0^1 dx\, x^{n-1} \left[g_1(x, Q^2) + \frac{n}{n-1} g_2(x, Q^2) \right] = \frac{1}{2} \sum_i d_n^i(Q^2) C_{2,i}^n(Q^2) \quad n = 3, 5, 7... \tag{1.53}$$

where $d_n^i(Q^2)$ are the matrix elements and $C_{2,i}^n(Q^2)$ are the Wilson coefficients, introduced in section 1.2.6. Further theoretical calculations [36,38] show that the twist-3 operators, entering in the expression for $\overline{g}_2(x, Q^2)$ depend on quark masses, quark-gluon interactions and are not zero. Following these arguments and using 1.53, a measurement of g_2 could provide information on quark-gluon correlations in the nucleon.

Burkhard-Cottingham sum rule

The Burkhard-Cottingham sum rule [43] states, that the first moment of the structure function $g_2(x, Q^2)$ vanishes:

$$\Gamma_2(Q^2) = \int_0^1 dx\, g_2(x, Q^2) = 0. \tag{1.54}$$

This result does not follow from the OPE, since it requires knowledge on the first moment of g_2, which is not defined, since Eq.1.48 is not valid for $n = 1$. The Burkhardt-Cotthingam derivation is based on Regge theory and is expected to be valid for both proton and neutron. However, there is a criticism in [44] as to the validity of the derivation of the sum rule and in particular of the behavior of g_2 as $x \to 0$. It is shown, that in this limit g_2 behaves as:

$$g_2(x) \propto \frac{1}{x^{1+\alpha}} \qquad 0 < \alpha < 1 \tag{1.55}$$

in which case the integral 1.54 diverges.

Efremov-Leader-Teryaev sum rule

The Efremov-Leader-Teryaev sum rule [45] is derived from Eq.1.48 for the case of $n = 2$, under certain model-dependent assumptions, presented in [31]. It states, that:

$$\int_0^1 dx\, x \left[g_1(x) + 2g_2(x) \right] = 0. \tag{1.56}$$

It should be noted, that like the Burkhardt-Cottingham sum rule this result does not follow strictly from OPE. Analogous to the criticism presented in [44], this sum rule will fail, because of the divergence of the integral $xg_2(x)$ if g_2 behaves as $1/x^2$ as $x \to 0$.

14

Second moment of g_2, twist-3 matrix elements

The QCD based sum rules for g_2 are derived from OPE for $n = 3, 5, 7....$ Following Eq.1.48 the valid sum rule involves evaluation of the moments of both g_1 and g_2:

$$\int_0^1 dx\ x^{n-1} \left[g_1(x) + \frac{n}{n-1} g_2(x) \right] = \frac{1}{2} d_n C_2^n \qquad n = 3, 5, 7... \qquad (1.57)$$

Theoretical calculations are limited to the case $n = 3$, which defines the second moment of g_2. The twist-3 matrix elements d_n for the same case were calculated from QCD sum rules by [39] for both proton and neutron for free quark fields. More recent calculations by [38] take into account a gluon field contribution. Bag model predictions for d_3 were made by [40,41].

Using experimental results for g_1 and g_2 they can be tested through:

$$\int_0^1 dx\ x^2 \left[g_1(x) + \frac{3}{2} g_2(x) \right] = \frac{1}{2} d_3 C_3^2, \qquad (1.58)$$

which through the Wandzura-Wilczek relation (Eq.1.51), can be further reduced to:

$$\int_0^1 dx\ x^2 \overline{g}_2(x) = \frac{1}{3} d_3 C_3^2. \qquad (1.59)$$

The preditctions for d_3^p and d_3^d are much smaller than the sensitivity of the present experiments which therefore cannot distinguish between the different models. Table 1.1 lists the results from the QCD sum rules and Bag model calculations.

	QCD ref.[39]	QCD ref.[38]	Bag ref.[40]	Bag ref.[41]
d_3^p	-0.003 ± 0.003	-0.006 ± 0.003	0.0176	0.0060
d_3^d	-0.013 ± 0.005	-0.017 ± 0.005	0.0066	0.0029

Table 1.1: *Theoretical predictions for the twist-3 matrix elements d_3 for proton and deuteron. The Bag model results are for $Q_0^2 = 5\ GeV^2$, the QCD calculations are for $Q_0^2 = 1\ GeV^2$.*

2 SMC experimental apparatus

2.1 Introduction

The experimental setup of the Spin Muon Collaboration (SMC) is located in the CERN experimental area North and has four main elements: polarized muon beam, polarized solid target, muon spectrometer and beam polarimeter. The spectrometer is the upgraded version of the one used by the European Muon Collaboration (EMC) and the New Muon Collaboration (NMC), who performed experiments in the same experimental area, studying the nucleon structure in deep inelastic muon-nucleon scattering. A substantial part of the apparatus and the data acquisition system was inherited from the NMC [47], with aged components replaced or renewed. Some of the major modifications include:

- New polarized target.

- New muon identification part, comprising of streamer chambers and, close to the beam, proportional chambers.

- Modification and repositioning of the small angle triggers.

- A beam polarimeter.

These modifications are discussed later in this chapter.

2.2 The polarized muon beam

The CERN M2 beam line was designed [48] to provide beam with typical intensity 4.5×10^7 muons per 2.4 *sec* pulse, repeated each 14.4 *sec* at high energies 100 GeV $< E_{\text{beam}} <$ 225 GeV. The beam line consists of three stages: the front end, a decay channel and the back end.

At the **front end** the extracted proton beam with energy of 450 GeV and intensity of about 50×10^{11} particles per pulse is directed onto a beryllium target of 50 cm thickness. The produced secondary pions and kaons of the desired momentum are selected with a momentum bite of $\Delta p/p = 10$ % and directed into a 600 meters long **decay channel** where for $p = 190$ GeV about 4 % of the hadrons, mainly pions, decay into muons through $\pi \to \mu\nu_\mu$. The muons are naturally polarized due to the parity violating nature of the

weak process [49]. The muon polarization is related to the muon and parent pion energy ratio:

$$P_\mu = \frac{m_\pi^2 + (1 - 2E_\mu/E_\pi)m_\mu^2}{m_\pi^2 - m_\mu^2} \qquad (2.1)$$

and the highest polarization is obtained for E_μ/E_π close to unity. Though a high value of polarization is desired, it has to be compromised with the muon beam intensity. The optimum value for obtaining a high polarization and a reasonable muon intensity turned out to be $E_\mu/E_\pi = 0.91$. For this value the polarization of the positive muons is -0.8 [79]. The momentum selection is performed at the end of the decay channel in a bending magnet, which selects muons with momentum bite $\Delta p/p = 3$ %. A 9.9 m long berillium absorber, placed in the same magnet removes the remaining hadrons from the beam.

In the **back end**, the angular spread of the muons is limited in a series of quadrupole magnets. The amount of stray muons (halo) around the beam is reduced, using a set of magnetized collimators, placed in a dipole magnet, to about 2.5 % outside a radius of 5 cm around the beam. The momentum of each muon, registered by the experimental triggers, is measured in a dedicated spectrometer, the so called Beam Momentum Station (BMS). After the BMS, another bending magnet brings the beam into the experimental area.

2.2.1 Momentum measurement of the beam muons - BMS.

Since the momentum of the beam muons enters directly in the calculation of the experimental asymmetry and the momentum spread is relatively wide (Fig.2.2), it is necessary to measure the momentum of each incoming muon. This task is performed by a magnetic spectrometer, made of four fast scintillator hodoscopes, two of them placed upstream and the other two downstream of a bending magnet (B6). The current of B6 is adjusted with respect to the beam energy, such that the bending angle is always 33.7 mrad. For a beam energy of 190 GeV the magnet has a bending power of 21.34 Tm, which was constantly monitored by Hall probes and kept stable within 0.05%. The schematic layout of the BMS is given in Fig.2.1.
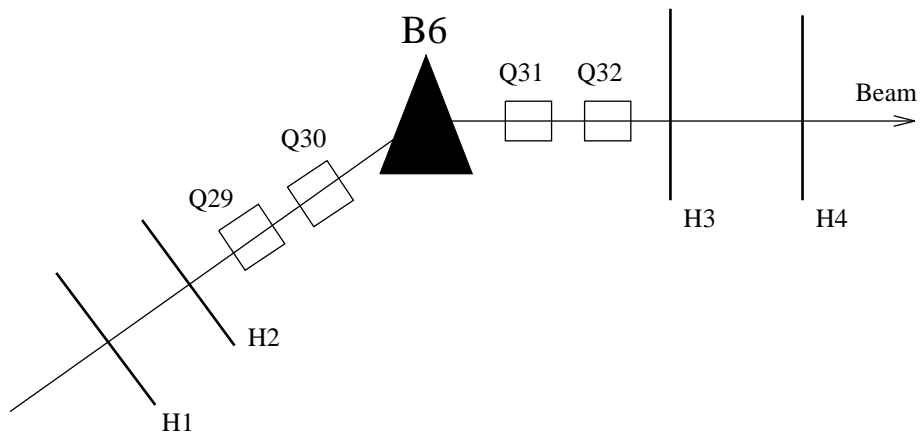

Figure 2.1: *Layout of the beam momentum station. H1 to H4 - planes of fast scintillation hodoscopes, Q29 to Q32 - focusing quadrupoles, B6 - bending magnet.*

Each of the hodoscopes consists of 64 scintillator elements 5 *mm* wide, placed horizontally in the bending plane of the magnet. There is a small spatial overlap between the adjacent strips to ensure full beam phase space acceptance. The strips are of variable length, chosen such that the individual rates do not exceed 3×10^7 muons per second, resulting in an allowed maximum rate of 10^9 muons per second on each plane. The thickness of the strips along the beam is 20 *mm*, which gives large output signal, necessary for accurate timing [51]. Individual photomultiplier signals are processed by an array of LeCroy TDC's with 50 ps timing step and a common start, given by the experiment's triggers. The momentum calculation requires at least one hit in three of the BMS planes and is based on the relation

$$p_{true} = p_0 + \delta p \; , \tag{2.2}$$

where p_0 is equal to the nominal mean momentum of the beam and corresponds to a particular muon passage through the BMS planes. δp is calculated from the difference between the actual passage and the particular one. Since the detector itself only measures a deviation from a central p_0, it needs an external absolute calibration. A calibration was made by the NMC collaboration, using a dedicated beam calibration spectrometer [52]. For muon energy of 190 GeV the precision of the BMS is $\Delta p_0/p_0 = 0.005$. A typical spectrum of the reconstructed beam momentum is given in fig.2.2.
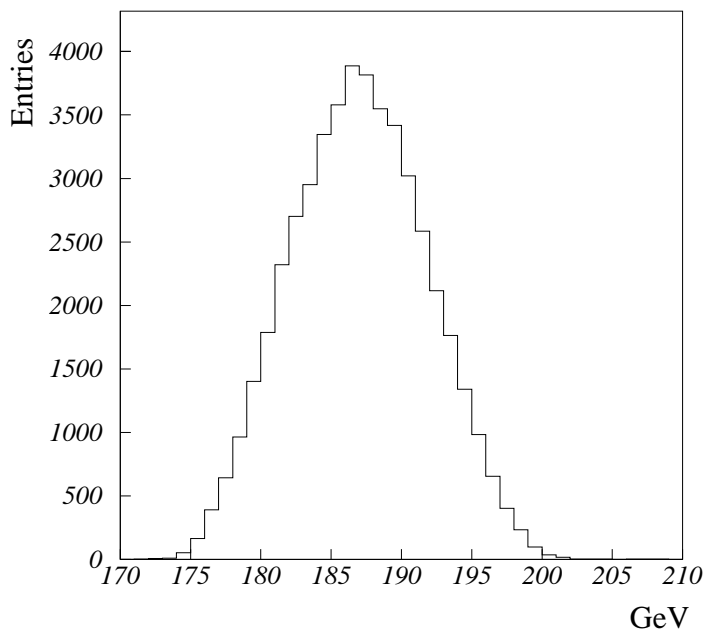

Figure 2.2: *Momentum spectrum for beam energy of* 190 *GeV.*

In the year 1992 the SMC took control of the BMS equipment from the CERN beam instrumentation group. This transition was done in order to improve the reliability and reconstruction efficiency of the apparatus. A major overhaul of all four planes was done, during which the pulseheight spectra of the 256 photomultipliers was tested and the high voltages readjusted to values at which the individual efficiencies were above 99 %. Elements with deteriorated photocatode efficiency were replaced. As a result of this adjustment, the BMS reconstruction efficiency was raised from 93 % to 98 %, which is a

direct 5 % gain of events.

The working status of the BMS was checked several times during each data taking period and the faulty elements were replaced immediately. Through this procedure a high overall reconstruction efficiency was ensured for the entire duration of the experiment from 1992 to 1996.

2.3 The polarized target

This section contains a description of the components of the SMC polarized target for the year 1995, physics principles of the polarization process, target operation and the method of obtaining transverse spin orientation. Detailed references on the subject are [53,54,55, 56] and [57]. Differences in the construction and operation procedures for the duration of the SMC experiment can also be found there.

2.3.1 Target construction and material

SMC uses a thick, solid state dual target with the following major parts:

- Dilution refrigerator, capable of delivering 1 W cooling power at $T = 0.4$ K.

- Superconducting magnet system, consisting of a solenoid with a nominal longitudinal field of 2.5 T, parallel to the beam axis, and a dipole with field of 0.5 T, perpendicular to the beam axis. The dipole field is used to obtain a transverse target polarization and as holding field during a polarization reversal.

- Microwave system for dynamic nuclear polarization.

- Two target cells, 64 cm long, 5 cm diameter, total volume of 2×1280 cm^3. The cells are separated by a 20 cm gap, filled with microwave absorbing material, which allows the target material in the two halfs to be polarized with opposite spin direction at the same time.

- Polarization measurement system, consisting of 10 Nuclear Magnetic Resonance (NMR) coils, 5 in each half, placed at various longitudinal and radial positions.

The schematical drawing of the polarized target is shown in Fig.2.3

The target dilution refrigerator circulates a $^3He/^4He$ mixture, precooled by a separate ^4He evaporation refrigerator. At temperatures below 0.7 K the mixture of ^3He and ^4He separates into a ^3He rich phase and the so called dilute phase, where ^3He is dissolved with low concentration in superfluid ^4He. The dilute phase is pumped and the evacuated gas contains mostly ^3He, due to its higher vapor pressure compared to ^4He. This causes ^3He 'evaporation' from the rich phase into the dilute phase. Heat, needed for this evaporation is taken from the chamber, where the separation occurs. The chamber contains the target material. The dilution refrigerator is similar in principle to an evaporation refrigerator, but here the vapor phase is substituted by the dilute phase. The difference is, that at

absolute zero, there is still a finite amount (6.5 %) of ^3He in the dilute phase and conse-
quently, cooling continues down to very low temperatures, which cannot be reached with
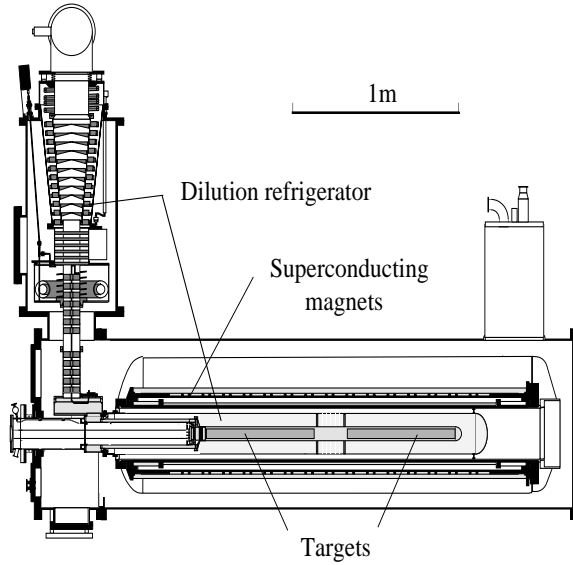an evaporation refrigerator due to the decreasing vapor pressure.

Figure 2.3: *Side sectional view of the SMC polarized target. The muon beam enters the target from the left.*

The superconducting magnet system was designed to provide highly homogenuous
magnetic fields - solenoidal and dipole for longitudinal and transverse target polarization.
The transverse dipole is also used as a tool for a quick rotation of the longitudinal polari-
zation. The polarization rotation is performed by reversing the field sign in the solenoid.
The dipole field is applied when the solenoid field is between $0.5\ T$ and $-0.5\ T$ in order
to avoid transition through zero field, which would destroy the polarization. Changing
the orientation of the solenoid field does not change the sign of the nuclear polarization,
which is defined with respect to the magnetic field, but is does change the orientation of
the nucleon spins with respect to the beam muon spins. For data taking periods with
longitudinal spin orientation, the procedure of spin rotation was performed five times per
day and is one of the most important steps for the reduction of the systematic error due
to acceptance variations in the spectrometer with time.
For the period P2E95 with transverse polarization, the target was polarized longitudi-
nally, which took 8 hours, then the polarization process was stopped and the spins are
rotated in perpendicular direction and held in the $0.5\ T$ dipole filed. In order to avoid
retuning of the beam transport, the dipole field was kept pointing always in one direction
and the target polarization was reversed with microwaves in average once in three days.

Two independent microwave generators are used to polarize the target halfs. The sources
are two Extended-Interaction-Oscillator tubes wich provide microwaves of about $70\ GHz$
and $20\ W$ power. The mechanism of target polarization is described in section 2.3.2.
The frequencies are tuned to be slightly above (below) the electron Larmor frequency,
$\omega_e \sim 2\pi \times 70\ GHz$, which at $2.5\ T$ provides a negative (positive) polarization of the tar-
get halfs. By additionally modulating the microwave frequencies by $30\ MHz$ at $1\ KHz$

rate leads to increase of the build-up rate and the maximum values of the polarization by factor of 2 and 1.7, respectively for deuteron and 0.2 and 0.6 for proton. The method of frequency modulation is described in [58].

The target polarization is measured by means of nuclear magnetic resonance (NMR). The measuring system consists of 10 NMR coils (5 in each target half), placed in the target material and connected to 10 series Q-meters. The NMR coils are distributed along the target axis and 2 smaller coils are placed at different radii at the same longitudinal position. No significant radial dependence of the value of the polarization was found.
Material polarization is proportional to the integrated NMR absorption signal, with the Q-curve subtracted from it. A Q-curve is the response of the Q-meter in the absence of signal, measured by shifting the Larmor frequency out of the resonance of the circuit by increasing the magnetic field. This curve is measured during field rotation. The integrated NMR signal is calibrated several times per year in a special run by measuring the small natural polarization of the material in a strong magnetic field at thermal equilibrium ($T = 1\ K$). The natural polarization for spin-$\frac{1}{2}$ and spin-1 particles is known from the Curie law:

$$P_{\frac{1}{2}} = \tanh\left(\frac{\mu B}{2kT}\right) \qquad\qquad P_1 = \frac{4\tanh\left(\frac{\mu B}{2kT}\right)}{3 + \tanh^2\left(\frac{\mu B}{2kT}\right)}, \qquad (2.3)$$

where μ is the magnetic moment and k is the Bolzmann constant. In a magnetic field of 2.5 T and temperature of 1 K the polarization is 0.9×10^{-3} for the deuteron and 4.5×10^{-3} for the proton.

As a target material, SMC uses hydrogenic (C_4H_9OH) or deuterated (C_4D_9OH) butanol with added 4 % chemical dopant [1] EHBA-Cr(V) or EDBA-Cr(V) in case of deuterated butanol. The choice of material is justified by the reasonable fraction of protons or deuterons, the required solid state properties and the absence of other polarizable nuclei. Since the butanol is non-magnetic, with electron spins coupled to zero, to make it suitable for polarization some unpaired electrons have to be added. The EHBA-Cr(V) (EDBA-Cr(V)) complex provides paramagnetic centers with partially unpaired electrons. In addition the material contains 4.6 % of water (H_2O or D_2O). This addition is needed to produce the butanol in glassy beads, otherwise it will become crystalline during freezing and the paramagnetic centers will not be evenly distributed. The beads are made by imersing drops of material in liquid nitrogen bath. Beads with diameter of about 1.8 mm are selected and loaded into the two target holders.

2.3.2   Basic principles of Dynamic Nuclear Polarization (DNP)

The method of Dynamic Nuclear Polarization permits to enhance the small natural polarization of the target material many times above the termal equilibrium value. For the process to work, the butanol must contain a small amount of unpaired electrons, with magnetic properties resembling those of free electrons. In the 2.5 T magnetic field of the target and at temperatures about 1 K these free electrons are highly polarized [2]. DNP

---

[1] Chemical formula of the radicals is $Na^+[C_{12}H_{20}O_7Cr \cdot H_2O]^-$ or $Na^+[C_{12}D_{20}O_7Cr \cdot D_2O]^-$
[2] Calculated electron polarization for $T = 1\ K$ and $B = 2.5\ T$, using Eq.2.3 is 0.98

transfers part of the electron polarization to the nucleon by supplying the right microwave frequency. Consider a system of electron-proton pair in a 2.5 T magnetic field. The energy splitting of the electron and the proton in the four possible states is shown in Fig.2.4, and is given by the Larmor frequencies of the electron $\omega_e/2\pi = 70\ GHz$ and the proton $\omega_p/2\pi = 160\ MHz$. Microwave fields are used to stimulate simultaneous spin flips of the coupled electron-nucleon pairs. The relaxation time of the electrons is shorter than of the nucleon ($10^{-3}\ s$ compared to $10^3\ s$), leading to an overalll build-up of the nucleon polarization. After some time all nucleon spins near the paramagnetic centers will be polarized and the polarization will stop. However, due to nucleon spin-spin diffusion the polarization is distributed throughout the target material. Using frequencies $\omega_e + \omega_p$ and $\omega_e - \omega_p$ the polarization can be enhanced with negative or positive sign. Typical achieved polarization values are $P_p \geq \pm 90$ % for proton and $P_p \geq \pm 50$ % for deuteron.
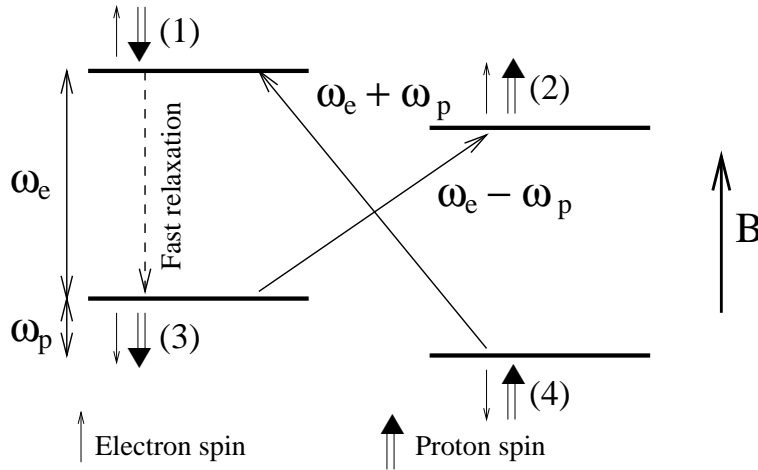

Figure 2.4: *Energy levels of an electron-proton pair in a strong magnetic field, given in terms of frequency ω. The forbidden transitions (3) $\to$ (2) and (4) $\to$ (1) are simulated by the microwave field - DNP process.*

2.3.3   Target polarization in transverse spin mode

While in a transverse polarization mode, due to the dipole magnetic field, the measurement of the target polarization could not be performed. To do so would require retuning and extensive calibration of the NMR system Q-meters. Furthermore, due to the somewhat larger inhomogeneity of the transverse field compared to the solenoid field, the quality of the measurement would be impaired. Instead of retuning the NMR system, a method of estimation of the polarization was devised. It is based on a study [59] of the spin relaxation which is the polarization decay over time as a function of lattice temperature and magnetic field. At temperatures in the range of tens of mK (base temperature) and magnetic field strength of 2.5 T the relaxation time is of the order of thousand hours. Since the target polarization is performed at temperatures $0.5 - 1.0\ K$, the base temperature is reached only after 8 to 12 hours after the microwave irradiation is switched off. The biggest losses of polarization occur during that period of cooling.

Relaxation dependence was studied under a scenario, representing the actual data taking

conditions. First, the target polarization is build up to a certain value with microwaves. After that, with microwave power off, a rapid cooling is performed, the polarization is measured and the solenoid field is ramped down from 2.5 T to 0.5 T (the strength of the dipole field). The latter step is important, since the relaxation time is shorter by about factor of 10 at 0.5 T field [61]. Over a period of time, the temperature in the target is monitored continuously, and several times during that interval, the polarization is measured again. Using the information on the temperature T and polarization it was concluded, that the relaxation time has an exponential temperature dependence:

$$\tau(T) = e^{(a-bT)} \tag{2.4}$$

The parameters a and b were varied to fit the curves to the data. No difference in the relaxation times between negative and positive polarization was found.

The actual target polarization P during data taking as a function of time was calculated, using Eq.2.4 and the temperature database from the target slow control computer:

$$P(t + \Delta t) = P(t)e^{\frac{-\Delta t}{\tau T(t)}}, \tag{2.5}$$

where $P(t)$ is the measured polarization value at the beginning of the data taking subperiod.
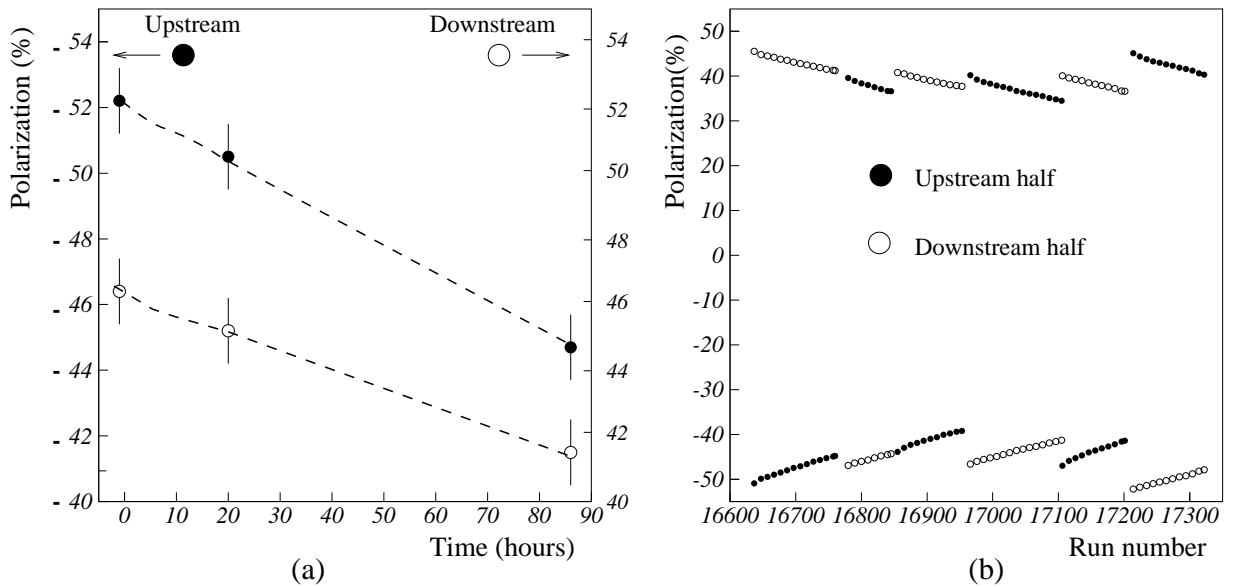
Figure 2.5: *(a) Upstream and downstream target polarization for the first subperiod of period P2E95. The black and open circles represent measured polarization, with its statistical accuracy. The dashed line is the interpolated polarization. (b) Target polarization in P2E95 as a function of run number.*

Another polarization measurement is performed at the end of the subperiods, and in case of pauses in data taking for at least one hour, also during the subperiods. Fig.2.5(a) shows the interpolated polarization of the two target halfs in subperiod 1 as a function of

23

time, Fig.2.5(b) shows the polarization for all 6 subperiods as a function of run number. The error on the polarization measurement is $\Delta P/P = 0.02$ [60]. An additional error, resulting from the fitting procedure is estimated by calculating the average deviation from the linear interpolate between the measured points and is quadratically added to the measurement error. Thus, the error on the target polarization in transverse spin mode increases to 0.021.

2.4   Spectrometer overwiev

The SMC spectrometer was designed to determine with high precision the trajectories of the incident and scattered muon. From this information and the interaction point in the target the kinematics of the scattering can be determined. A large redundancy in the number of detector planes makes the spectrometer as a whole insensitive to efficiency variations in individual detectors, thus the acceptance ratio for the upstream and the downstream target cell between polarization reversals remains stable, which is of particular importance since the value of the measured asymmetry $A_\perp$ is a fraction of a percent. A side view of the SMC spectrometer is shown in Fig.2.6. Individual parts of the spectrometer are discussed later in this chapter.
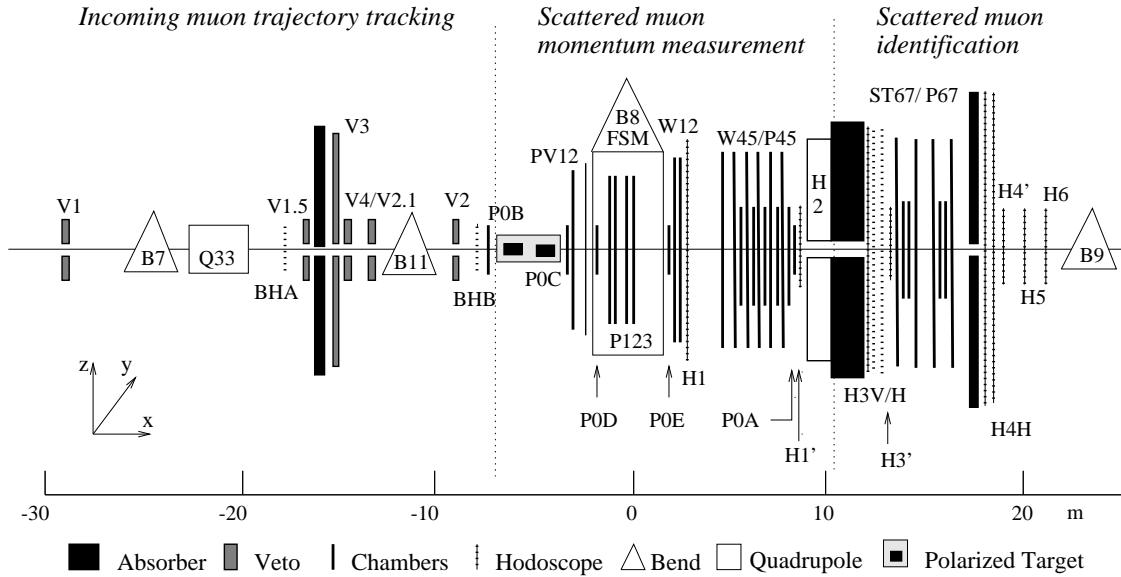
Figure 2.6: *Schematic view of the SMC spectrometer. The three main parts are separated with vertical dotted lines. The muon beam enters the picture from the left.*

2.4.1   Veto system

The function of the veto is to define the beam phase space that can be used for a trigger and to reject spurious triggers, caused by halo muons entering the apparatus. There are 5 independent veto counters, situated in the apparatus area before the polarized target:

- V1, V1.5 - positioned before and after the final bending magnets in the beamline. They consist of four scintillator elements each, total covered area of 50 $cm \times$ 50 cm, and have a circular hole for the beam of diameter 13 cm. The purpose of this counters is to veto near-beam halo muons.

- V3 - positioned after a 50 cm iron absorber. This is a large veto wall with dimensions 6.5 $m \times 4.0$ m with a central beam hole of 40 $cm \times 40$ cm. Its purpose is to suppress large angle halo muons far from the beam.

- V2, V2.1, V4 - positioned before the polarized target, each consists of four scintillator elements, total covered area of 25 $cm \times 25$ cm, with a circular hole for the beam of diameter 6 cm. Depending on the type of measurement, either V2 and V2.1 (longitudinal target magnetic field), or V2 and V4 (transverse target magnetic field) define the useful beam.

The signals from all vetoes, after discriminators and shapers, are logically OR-ed in a single $\Sigma \, V$ signal, which enters as $\overline{\Sigma \, V}$ in all physics triggers as an inhibit signal. The need of a sophisticated veto system is due to a high flux of halo muons, compared to the interaction rate. The accidentally rejected amount of beam by the veto system is about 5%.

2.4.2 Definition of the triggers

Trigger	Description	Type
T1	Large angle scattered muons	Physics
T2	Small angle scattered muons	Physics
T5	Beam muons	Alignment, calibration
T7	Near to the beam halo muons	Alignment, calibration
T8	Far from the beam halo muons	Alignment, calibration
T9	Random trigger from pulser	Background studies, calibration
T10	Random trigger from radioactive source	Beam flux normalization
T11	Halo muons	T1 efficiency determination
T12	Halo muons	T2, T14 efficiency determination
T13	Start of spill, end of spill	CAMAC scalers readout
T14	Small x region	Physics
T15	Calorimetric	Physics

Table 2.1: *SMC triggers.*

The readout and data recording to a magnetic tape from various detectors is initiated by a trigger pulse from the triggers. SMC experiment has 12 triggers, of which 4 are for

physics. The non-physics triggers are used for alignment and calibration of the apparatus. The physics triggers recognize the scattered muon off the target and do not include the beam muon. Table 2.1 presents a general description of the triggers.

2.4.2a   Large angle trigger T1

T1 is formed from a triple coincidence of the signals in the large aperture hodoscopes H1, H3 and H4. These hodoscopes are made of rather big scintillating strips - 7 *cm wide* × 130 *cm long* in H1, 15 *cm wide* × 340 *cm long* in H3 and 15 *cm wide* × 435 *cm long* in H4. All strips are equipped with photomultipliers on each side for accurate timing.

H3 and H4 are placed behind a hadron absorber, which only muons can penetrate. Triggers, which are interesting for the experiment are selected using a series of programmable coincidence matrices [62], whose coincidence pattern defines which combinations of hodoscope elements are allowed. These patterns are obtained from a Monte-Carlo simulation of the hits in the hodoscopes [63]. Matrices M0 to M3 define a rough target pointing. Matrix M6 defines a minimum scattering angle with respect to the beam axis, filtering out events with low Q^2. Matrix M7 defines a minimum scattering angle and minimal displacement in the bending direction of the magnet, thus rejecting events with low Q^2 and large ν which require large radiative corrections. The trigger collects events with scattering angle, $15 mrad < \Theta < 150 mrad$, it is reasonably clean and the fraction of reconstructable events is about 60% of the total sample. The T1 logic is shown in Fig.2.7.

2.4.2b   Small angle trigger T2

T2 is formed by the 'primed' hodoscopes H1', H3' and H4'. These hodoscopes partially cover the region excluded by the holes in the large trigger hodoscopes. The strips are 1.4 *cm wide* × 50 *cm long*, much smaller than those of the T1 hodoscopes, which allows them to operate closer to the high rate environment of the beam. The trigger position and hardware was modified several times during the period of operation of SMC in order to optimize the x and Q^2 acceptance and reconstruction efficiency. The layout of T2 for the data taking period of year 1995 is shown in Fig.2.8. Similarly as for T1, the H3' and H4' hodoscopes are placed after the hadron absorber, which makes them sensitive only for muons. Geometrically, the hodoscopes have an up-down symmetry around the beam and are placed to have a rough target pointing. The logic of the trigger requires at least one hit in each plane either in the upper or the lower half. T2 has an angular acceptance of $5 mrad < \Theta < 20 mrad$ and contributes to the statistics at low Q^2. Its fraction of reconstructable events is about 50%.
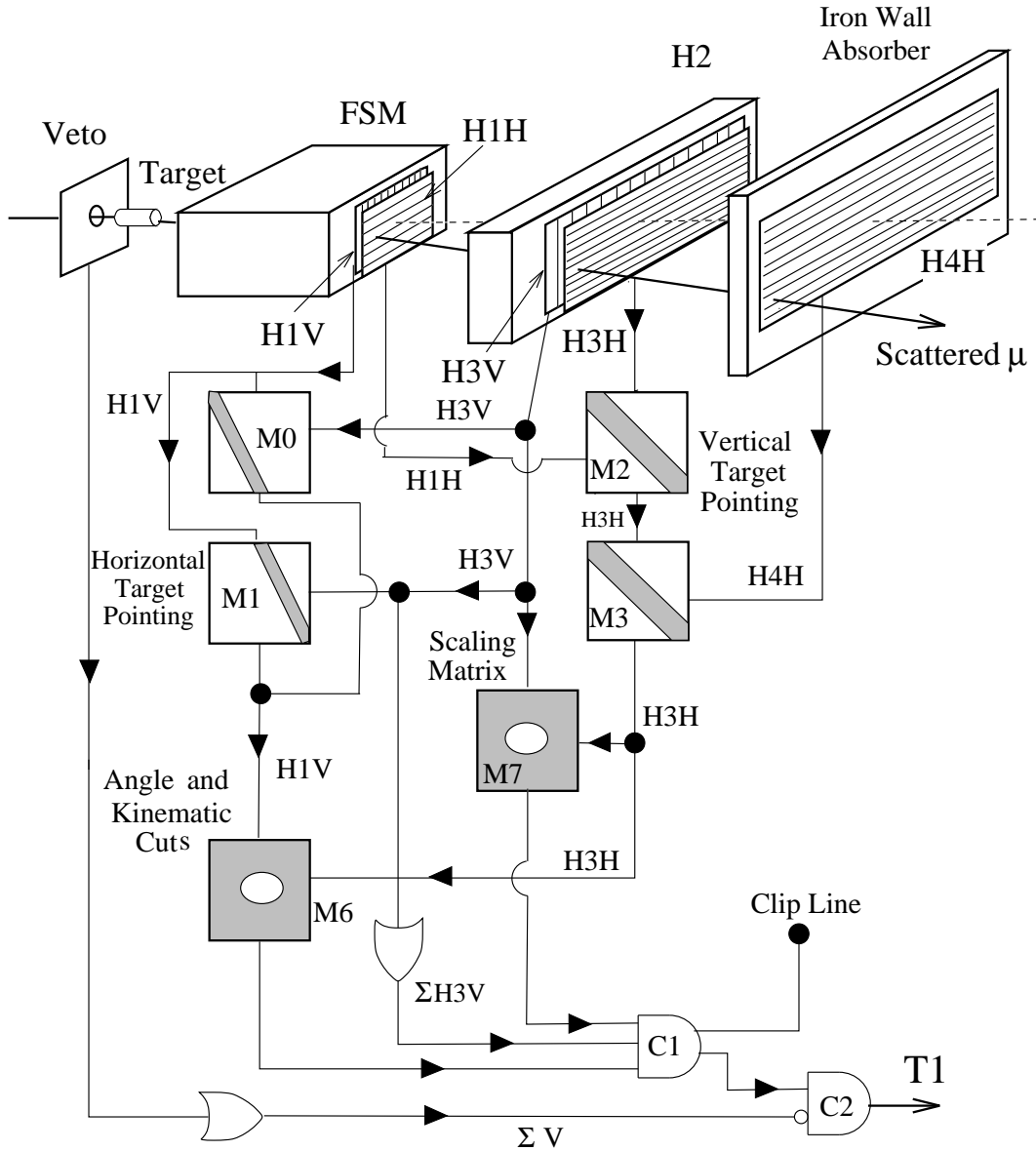
Figure 2.7: *Logic of the large angle trigger T1. The indices H and V after the hodoscope plane names denote the orientation of the scintillator strips, horizontal and vertical respectively. The matrices functions are also explained.*

2.4.2c Small x trigger T14

T14 is a simple trigger, made of 3 planes, each consisting of two scintillator pads, placed symmetrically around the beam. The planes, shown in Fig.2.8, are at the same x-position as the T2 planes, but are closer to the beam. A tripple coincidence in the upper or the lower pads is required for a valid trigger. Events from T14 are mostly in the low x, low Q^2 range.

All three physics triggers provide data, which overlap in the $x - Q^2$ plane to a certain degree allowing for a cross-check. This overlap is also used to determine the trigger

hodoscope efficiency stability over time. The acceptance in x - Q^2 plane for each of the triggers, before any physics cuts, is given in Fig.2.9.
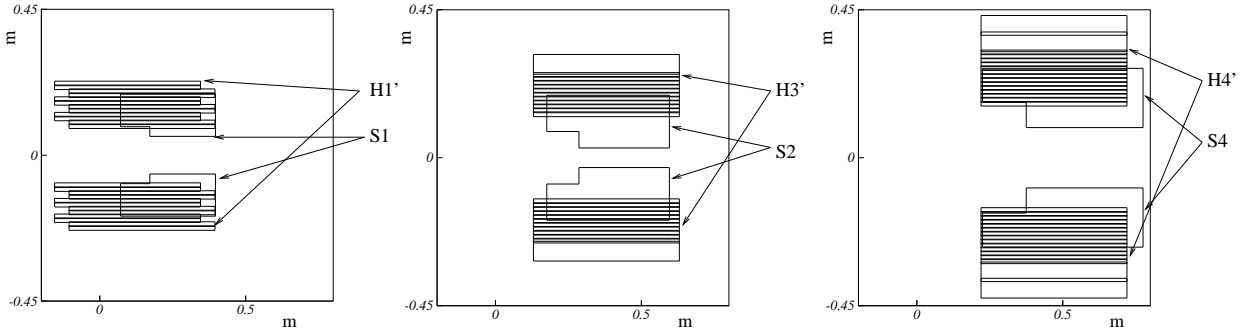

Figure 2.8: *Front view of T2 (H1', H3' and H4') and T14 (S1, S2 and S4) counters in the SMC coordinate frame. The beam center is at position (0,0). Note the overlap between the segmented strips of T2 counters.*

2.4.2d Alignment and calibration triggers T5, T7 and T8

The alignment and calibration procedure of the SMC apparatus involves three triggers, each of them illuminating different area of the spectrometer chambers and hodoscopes [64]. Alignment is done with straight beam and halo tracks, with beam intensity typically 10^5 muons per spill. The low intensity is required because of the relative simplicity of the triggers. In these conditions the hit multiplicity in the chambers and the hodoscopes is practically 1, leading to unambiguous and simple track reconstruction allowing an automatized procedure for the alignment.

T5 is used to align the beam chambers P0's and the beam hodoscopes BHA and BHB. It requires a coincidence between the two planes of the hodoscope H5. The same trigger is used at nominal beam intensity to calibrate the TDC's of the Beam hodoscopes (BHA, BHB) and the Beam momentum station (BMS).

T7 and T8 are used to align the large spectrometer chambers. T7 is defined as a hit in in the central elements of the veto wall V3 and the inner strips of the hodoscopes H3H and H4H. T8 uses the external elements of V3, H3H and H4H.The triggers cover respectively the inner and the outer regions of the proportional chambers PV1, PV2, P123, P47; of the drift chambers W12, W45 and of the streamer chamber ST67. The same data sample is used to perform a drift time calibration of W12 and W45.

2.4.2e Hodoscope efficiency triggers T11 and T12

An independent determination of the physics triggers efficiency is made using T11 - efficiency of T1, and T12 - efficiency of T2 and T14.
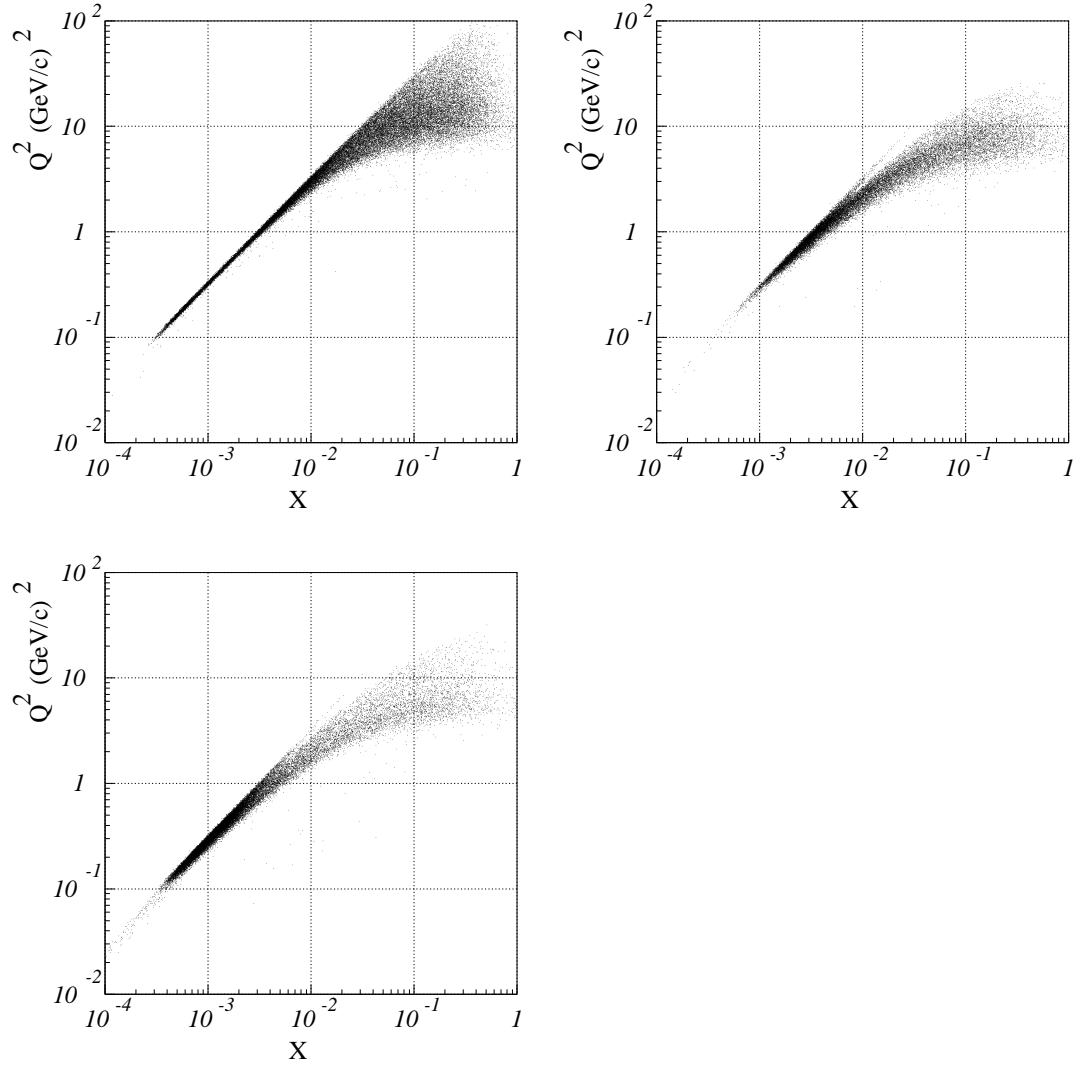
Figure 2.9: *Acceptance of the physics triggers T1, T2 and T14 in* $x - Q^2$ *plane. No cuts are applied to the data. The event sample plotted is from the period P2E95 (transverse target polarization).*

T11 is defined as a coincidence of the elements of the veto wall V3 and alternatively[1] the elements of the hodoscopes H3H and H4H. This trigger allowed unbiased calculation of the efficiencies of each individual plane of the T1 hodoscopes.

T12 uses independant hardware. Two planes of scintillator hodoscopes (H3'V and H4'V) are placed behind H3' and H4', covering geometrically all elements used in T2 and T14. The trigger is defined as a coincidence between H3'V and H4'V. This particular solution allowed to record the data for the efficiency determination of all hodoscopes used in T2 and T14 parallel to normal data taking.

The data for the triggers efficiency determination is taken at the same beam intensity as for a normal data taking in order to avoid a possible intensity dependent bias.

2.4.2f   Other triggers

T9 is a random trigger, based on a pulser. Its purpose is to study beam uncorellated effects in the spectrometer chambers - electronic noise, readout problems. Subsequently it is used in the check programs of the experiment slow control to verify the working state of the readout electronics for the Beam hodoscopes (BHA, BHB) and the Beam momentum station (BMS).

2.4.3   The beam muon tracking

The SMC spectrometer can be schematically divided in three parts: beam muon tracking (before the polarized target); magnetic spectrometer (after the polarized target and before the iron absorber) and scattered muon identification (after the iron absorber) (see Fig.2.6).

Beam muon tracking is the first spectrometer section. It consists of two beam hodoscopes - BHA and BHB and the proportional chamber P0B. The parameters of the detectors are listed in Table 2.2.

Name	Detector type	Planes and orientation	Active area	Pitch [cm]
BHA	Scintillator hodoscopes	8 *planes total* $2 \times T^+, 2 \times T^-, 2 \times Y, 2 \times Z$ $T^\pm = \pm 45^\circ$	8×8 *cm*	0.4
BHB	Scintillator hodoscopes	8 *planes total* $2 \times T^+, 2 \times T^-, 2 \times Y, 2 \times Z$ $T^\pm = \pm 45^\circ$	8×8 *cm*	0.4
P0B	Proportional chamber	8 *planes total* $2 \times T^+, 2 \times T^-, 2 \times Y, 2 \times Z$ $T^\pm = \pm 60^\circ$	*circular* $r = 7$ *cm*	0.1

Table 2.2: *Properties of the beam muon tracking detectors.*

---

[1]Conditions changed automatically at the beginning of each tape.

The task of these detectors is to determine the incoming beam muon trajectory with good spatial and timing precision. The BHA and BHB effective spatial resolution is 2 mm due to the staggering of the planes by 2 mm. It is further improved by P0B, wich has a 1 mm wirespacing. The combined angular resolution of the detectors is ≈0.1 mrad. Major refurbishment of BHA and BHB was done in year 1993, when it was discovered [67], that some photomultipliers showed a strong intensity dependent behaviour - the signal amplitude decreased considerably at low beam intensity. About forty elements, showing the worst dependence were changed. Those showing lesser effect were moved to the wings of the inclined ($T^{\pm}$) planes of BHA, which have a very small influence on the beam track reconstruction. The readout of the beam hodoscopes is based on a standard LeCroy TDC's, with common start supplied by all the triggers in the experiment. To minimize the readout time, a zero suppressor module is placed in the chain.

The readout of the P0B chamber is based on a RMH (Receiver Memory Hybrid) system developed at CERN [68] for multi wire proportional chambers.

For the period P2E95, the transverse target magnetic field deflects the beam horizontally by -1.66 mrad. This requires a correction of the beam transport line, otherwise the high intensity beam would pass through the sensitive area of the spectrometer chambers. A bending magnet (Bend 11) was placed in front of the polarized target to compensate for the deflection, caused by the target dipole. Additionally, the bend at the entrance of the experimentall hall (Bend 7) was run with a different current setting in order to minimize the displacement of the beam at the entrance of the target. Schematically, the corrections of the beam transport are shown in Fig.2.10. The solid line on the figure represents the beam path in the area before the polarized target for the period P2E95, the period with transversely polarized target. The dashed line represents the beam path for data taking with longitudinal target polarization. This modification required changes in the reconstruction scheme for the beam tracks. They are discussed in section 3.4.1.
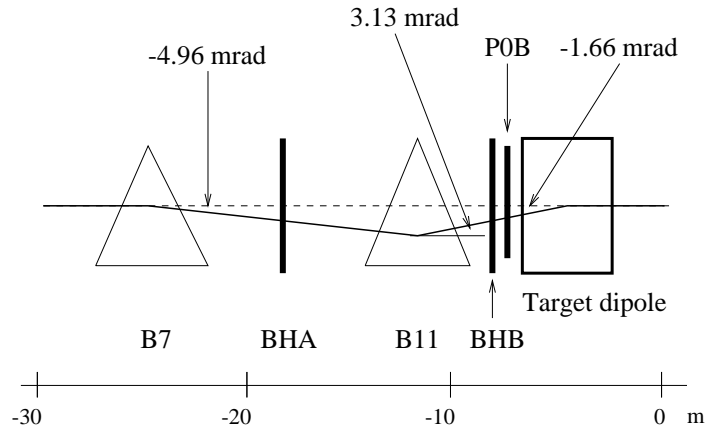

Figure 2.10: *Changes of the beam transport line for the period P2E95 (transverse target polarization) for a beam energy of 190 GeV. Same setup was used for periods P3A93 and P3B93 (transverse target polarization, measurement of A_2^p), but with different magnet current settings, due to the lower beam energy of 100 GeV.*

2.4.4   Magnetic spectrometer section

The spectrometer section downstream of the polarized target and before the hadron absorber is designed to provide the angle and momentum measurement of the final state particles and the scattered muon and, in combination with the information from the beam muon tracking section, the interaction vertex position. It consists of chambers placed in front, inside and behind a large-aperture dipole magnet (the Forward Spectrometer Magnet - FSM). The parameters of the detectors are given in Table 2.3.

There are three proportional chambers in front of the FSM, which provide the upstream lever arm for the momentum, angle and vertex measurement. PV1 and PV2 are large and cover the whole aperture of the magnet. P0C is a small chamber, which covers the deadened beam zones of PV1 and PV2 and therefore ensures that there are no regions with poor tracking efficiency. Proportional chambers are used in this area mainly because of the high particle flux immediately after the target. Particles with low momenta are removed by the FSM, which allows the use of chambers with lower channel density after the magnet.

The FSM is an air-core dipole magnet with the following dimensions: $2\ m \times 1\ m$ aperture and $4.3\ m$ lenght. It provides the necessary bending of the charged particles for momentum analysis. For the beam energy of 190GeV the magnet was operated at coil current $I = 4000\ A$, which results in bending power of $\int B\mathrm{d}l = 4.4\ Tm$. The magnetic field was mapped [69] with an accuracy of $\int B\mathrm{d}l < 2 \times 10^{-3}\ Tm$. During data taking the stability of the field was constantly monitored with Nuclear Magnetic Resonance (NMR) and Hall probes and kept within $\pm 0.03\%$.

Four proportional chambers, P1A, P1B, P2 and P3 are placed in the magnet, covering most of its aperture. They provide information about the track curvature in the magnetic field. Similarly to PV1 and PV2, they have a deadened beam region, which is covered by P0D - a small proportional chamber, placed immediately after the magnet. At the beginning of the SMC experiment, only three chambers were located in the magnet. During the analysis of the data from 1992 run, it was realized that the redundancy of the magnet chambers was marginal and the variation of the reconstruction efficiency versus time due to that was the biggest source of false asymmetries. In 1993 a fourth chamber, P1B, identical to the other three was installed in the magnet, thus lowering the single plane efficiency dependence of the global reconstruction efficiency [70]. The readout electronics from the most upstream chamber P1A was redistributed between P1A and the new chamber P1B, without sacrifice in acceptance for scattered muons [71]. Together with the addition of the fourth chamber, a system to stabilize the chamber efficiencies was installed (see App.6.3).

An array of drift and proportional chambers downstream of the FSM provides information for the second lever arm of the momentum measurement. Immediately after the FSM is the W12 drift chamber. It comprises 16 planes in various orientations with 2 cm drift cell and has a deadened region around the beam with $r = 6$ cm, covered by the P0E chamber, which has an active area with $r = 7$ cm. The readout of W12 consists of preamplifiers, mounted on the chamber and the CERN system DTR (Drift Time Recorder) [72]. The preamplifiers proved to be very sensitive to electronics pickup noise, therefore they were operated at high threshold. In order to obtain plane efficiencies in the range of $96 - 98$ %, the chambers were operated at high gas gain. Several planes of W12 suffered anode wire ageing in the region close to the beam ($r < 20$ cm). In six months

of beam exposure the efficiency in this region dropped to $40 - 50$ %. Since only 5 out of 16 planes suffered from this effect, the global reconstruction efficiency of W12 in the central region did not suffer considerably. Each year, after the end of data taking, the central wires of the planes showing ageing effects were replaced. An attempt was made in 1995 to preserve the planes from ageing by running W12 at lower threshold and lower anode high voltage after an improvement in the grounding and the threshold circuitry. Although this caused some planes to have lower overall efficiency (98 % in 1994 to 94 % in 1995), it reduced largely the ageing in the central regions and improved the stability of the global reconstruction efficiency. The effect of ageing on the efficiency of one of the affected planes is shown in Fig.2.11(a). The second plot, Fig.2.11 (b) shows the average efficiency of the central region ($r < 20$ cm) of the same plane versus time. The effect of ageing is clearly visible. The net effect on the global reconstruction efficiency of W12 is negligible due to the large plane redundancy.
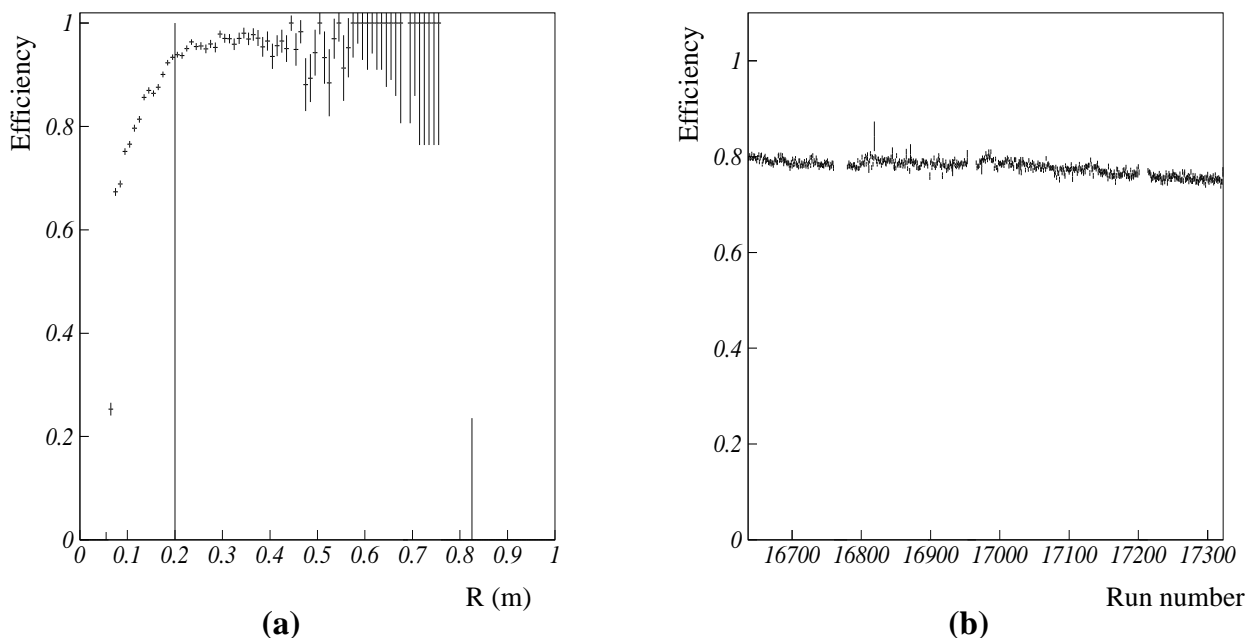

(a)   **(b)**

Figure 2.11: *(a) Radial dependence of the efficiency of W1 plane Y1 for RUN 16700 in data taking period P2E 1995.*
(b)Average efficiency of the central region ($r < 20$ cm) of plane Y1 versus run number for the period P2E 1995, last data taking period of the year. The run interval corresponds to 19 days of beam exposure. Central region efficiency at the beginning of 1995 was 95%.

The W45 drift chamber is situated 5 m further downstream of W12. It is a set of 6 separate modules, 4 planes each, with preamplifier cards mounted on the chamber and a DTR readout. The central regions of W45 planes suffers from low efficiency, related to the beam intensity, and are backed up by the proportional chamber array P45. P45 consists of 5 modules with two planes each, sandwiched between the W45 modules, with a circular active area with $r = 45$ cm. Like the other proportional chambers in the spectrometer it has a preamplifier mounted on the chamber and is read out by a RMH system.

Name	Detector group	Detector type	Planes and orientation	Active area	Pitch [cm]
PV1	Vertex chambers	Proportional chamber	4 *planes total* $2 \times Z, 1 \times T^-, 1 \times T^+$ $T^{\pm} = \pm 10.2^o$	$154 \times 80\ cm$	0.2
PV2		Proportional chamber	6 *planes total* $2 \times Z, 2 \times T_1^{\pm}, 2 \times T_2^{\pm}$ $T_1^{\pm} = \pm 18.4^o, T_2^{\pm} = \pm 45^o$	$280 \times 100\ cm$	0.2
P0C		Proportional chamber	8 *planes total* $2 \times Z, 2 \times T^+, 2 \times T^-, 2 \times Y$ $T^{\pm} = \pm 60^o$	*circular* $r = 7\ cm$	0.1
P1A, P1B, P2, P3	Magnet chambers	Proportional chamber	12 *planes total* $4 \times Z, 2 \times T^-, 2 \times T^+, 4 \times Y$ $T^{\pm} = \pm 20^o$	$182 \times 80\ cm$	0.2
P0D		Proportional chamber	8 *planes total* $4 \times Z, 1 \times T^+, 1 \times T^-, 2 \times Y$ $T^{\pm} = \pm 60^o$	*circular* $r = 7\ cm$	0.1
W12	Lever arm chambers	Drift chamber	16 *planes total* $4 \times Z, 4 \times T^-, 4 \times T^+, 4 \times Y$ $T^{\pm} = \pm 10.2^o$	$230 \times 124\ cm$	2.0
P0E		Proportional chamber	8 *planes total* $2 \times Z, 2 \times T^+, 2 \times T^-, 2 \times Y$ $T^{\pm} = \pm 60^o$	*circular* $r = 7\ cm$	0.1
W45		Drift chamber	24 *planes total* $8 \times Z, 8 \times T^+, 8 \times Y$ $T^+ = 60^o$	$520 \times 260\ cm$	4.0
P45		Proportional chamber	10 *planes total* $3 \times T^+, 2 \times T^-, 5 \times Y$ $T^{\pm} = \pm 30^o$	*circular* $r = 45\ cm$	0.2
P0A		Proportional chamber	8 *planes total* $2 \times Z, 2 \times T^+, 2 \times T^-, 2 \times Y$ $T^{\pm} = \pm 60^o$	*circular* $r = 7\ cm$	0.1

Table 2.3: *Properties of the detectors in the magnetic spectrometer. The role of the P0 chambers is to cover the deadened areas of the big chambers in each detector group, thus assuring that there are no regions of low reconstruction efficiency.*

2.4.5 Identification of the scattered muon

The chambers of the muon section were a completely new addition to the SMC spectrometer and will be discussed below in some details.

The choice of detectors in this region was dictated by the following factors:

- necessity of a large sensitive area - $3.5 \times 3.5 \ m^2$.

- large degree of redundancy to ensure stability of the reconstruction efficiency over time.

- low cost of the chambers and the readout electronics.

- ability to work in high intensity beam environment.

Plastic streamer tubes were choosen as a detector which meets the necessary requirements. In the high-rate close to the beam region the streamer tubes are supported by a set of small proportional chambers.

Name	Detector group	Detector type	Planes and orientation	Active area	Pitch [cm]
ST67	Muon chambers	Streamer tubes	$32 \ planes \ total$ $8 \times Z, 8 \times T_1^\pm, 8 \times T_2^\pm, 8 \times Y$ $T_1^\pm = \pm 67.5^o, T_2^\pm = \pm 112.5^o$	$400 \times 400 \ cm$	1.0
P67		Proportional chamber	$8 \ planes \ total$ $4 \times T^\pm, 4 \times Y$ $T^\pm = \pm 30^o$	$circular$ r = 45 cm	0.2

Table 2.4: *Properties of the detectors in the muon section. P67 is a backup of the central region of ST67.*

The first part in the muon identification section is a passive steel hadron absorber, $2 \ m$ long with a $20 \ cm$ diameter beam hole. Behind the absorber tracks are reconstructed in two detector groups. Table 2.4 lists their characteristics. The main detector in the section is the streamer tubes array ST67. It consists of four modules, spaced $1 \ m$ apart along the beam direction. Each module has four planes of streamer tubes, two of them mounted horizontally and two vertically. Unlike other detectors, where the signal readout is performed directly off the sense wire, the streamer signal is induced on two pickup planes on either side of the tubes. The construction of the array is highly modular. There are 48 replaceable streamer tubes in each plane, held in a separate sleeves. Each tube has eight $100 \ \mu m$ thick wires, made of silver coated $Cu - Be$ alloy. The tubes are made of two parts, a $400 \times 8 \times 1 \ cm$ PVC body and 8 open $400 \times .9 \times .9 \ cm$ wire cells made of the same material and coated with carbon DAG[1]. A sectional view of a tube is shown in Fig.2.12. All eight wires in one tube are connected with 220 Ω current limiting resistors through an end cap to the HV power supply. A removal of a tube from its sleeve can be performed easily and with no loss of positioning accuracy since they fit tightly in and are constrained on both sides.

Readout pickup strips are cut in a copper covered Vetronite[2] sheets with high precision and the sheets are glued on each side of the tube sleeves, one side of the strips running

---

[1] Colloidal graphite in methyl isobutyl keytone (MIBK) manifactured by Acheson Colloiden B.V., Holland.

[2] Glass-fiber - epoxy resin compound.

along the wire orientation (X or Y coordinate), the other running with 22.5 *deg.* angle with respect to the wire ($T^{\pm}$ coordinates). Thus in one module, for the 4 planes of streamer tubes, there are 8 readout coordinates. The efficient area of a plane is 85 % of the total area, therefore the tube planes in the module are staggered with respect to each other by 0.5 *cm* in order to cover the inefficient regions of the walls of the wire cells and the sleeves at least once.
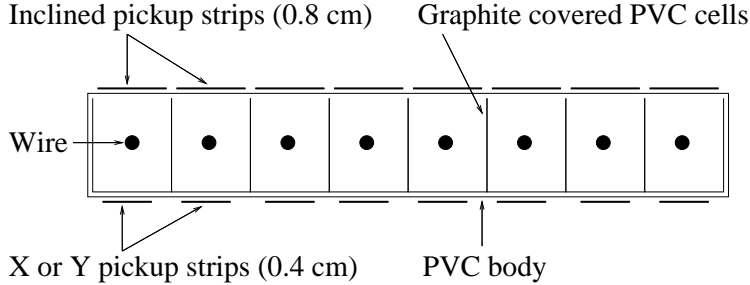

Figure 2.12: *Sectional view of a ST67 streamer tube and the signal readout strips. The wire spacing is 1 cm, readout strips run along the wire (X or Y coordinate) and with an angle of 22.5 deg. with respect to the wire ($T^{\pm}$) coordinates and are 0.4 cm and 0.8 cm wide, respectively.*

The electronics readout of ST67 consists of three modules which were developed specially for a streamer tubes system [73]. The first component of the readout are the front end cards, physically attached to the pick-up strips through twisted pair cables. Each card reads 32 contiguous strips and there are twelve chained cards for each plane (384 channels total). The card is built around the SGS D779[1] amplifier and shift register chip, which has 4 analog inputs with impedance of 100 Ω.

The chains are connected to a CAEN[2] SY480 splitter boards [74]. The splitter board serves four purposes. It acts as a cable driver for the cable connecting the front end cards to the CAMAC data aquisition modules located 15 m away, provides a threshold signal and a trigger signal for the input chips and separates the ground between the chamber electronics and the CAMAC modules through optocouplers. This last function is of particular importance, since in the first design of the system, used in year 1992, the noises transmitted through the ground from the CAMAC to the front end electronics caused a large amount of false signals.

The third component of the readout is the CAEN C267 STAS (Streamer Tube Acquisition System) module. C267 is a single width CAMAC module [75], which reads the information accumulated by the front end cards and transmits it to the experiment's data acquisition system. There is one STAS for eight ST67 readout strip planes.

2.4.5a ST67 High voltage plateaus and efficiency stability

The operation of a streamer tube array in a high beam intensity environment of the experiment represented a major challenge in two ways - attaining a high detector efficiency

---

[1]SGS-Thompson proprietary design.

[2]Costruzioni Apparecchiature Elettroniche Nucleari, Viareggio, Italy

and keeping it stable over the period of data taking.

The efficiency curve of the streamer tubes is shown in Fig.2.13. It was measured at beam intensity of $1 \times 10^6 \, \mu/spill$, which is substantially lower than the nominal ($4.5 \times 10^7 \, \mu/spill$). The plateau of high efficiency is attained at an anode voltage above 4700 V for both strip orientations. For the nominal intensity of $4.5 \times 10^7 \, \mu/spill$, operating at the middle of the plateau (4800 V) was shown to be impractical for two main reasons. First, most of the streamer tubes in the central region draw excessive current, which wears them down in a short time interval leading to a high failure rate. This decreases the efficiency stability of the system and requires a large amount of spares and time for replacement. Second, there is a significant increase in the number of adjacent strips clusters, giving a signal for a single muon passing through the chamber, worsening the spatial resolution. Also the number of noise hits increased.
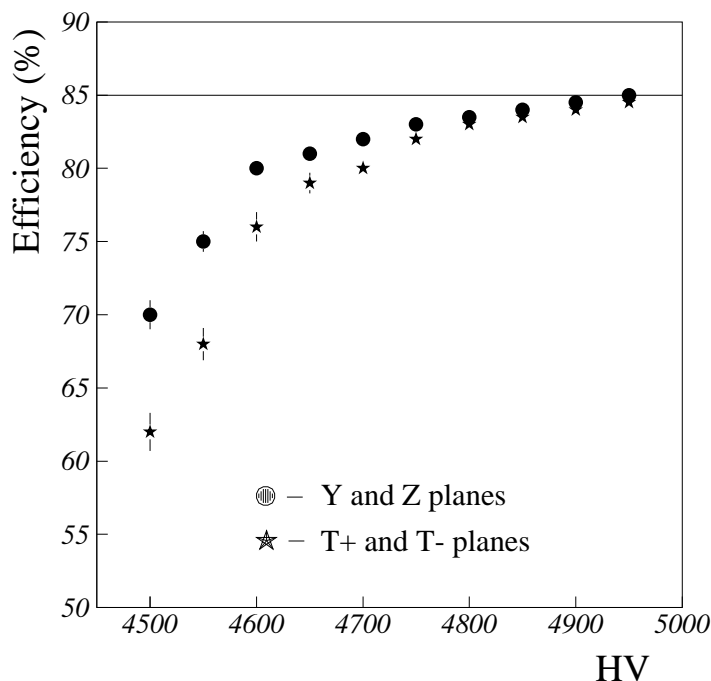

Figure 2.13: *Measured high voltage efficiency curve of ST67. The line at* 85 % *represents the maximum plane efficiency, which is restricted to* 85 % *by the geometry of the plane.*

As a compromise, during the 1992 data taking the streamer tubes were operated at $HV = 4600 \, V$, a point on the knee of the efficiency curve. This led to a lower overalll reconstruction efficiency and made the ST67 array susceptible to efficiency variations over time. To stabilize the chamber response a monitor and control system was developed and implemented. The system, called the 'feedback loop' measures the streamer charge, which for a given voltage is a function of the gas density, influenced by external factors such as ambient temperature and atmospheric pressure. Subsequently, it adjusts the high voltage of the system such that the mean charge remains constant within certain limits. This ensures that the amplitude distribution of the induced signal on the pickup strips is constant with time and since the threshold cutoff of the readout electronics does not

change, the efficiency of system remains stable. After a period of studies on the response of the streamer charge on the temperature and pressure, the stabilization system was put into operation in 1993. As a result,the plane and track reconstruction efficiency of ST67 were stabilized to 1.5 % and 0.9 % respectively. Extensive description of the 'feedback loop' is given in App.6.2.

2.4.5b   Proportional chambers array P67

A part in the muon identification system, added in year 1993, is the proportional chamber array P67. It was installed as a backup of the central region of ST67, where due to the dead time of the readout electronics, the efficiency is lower. P67 is a classical proportional chamber with cathode planes made of carbonized Capton[1], stretched on a frame and wire[2] anode planes with wire spacing of 2 *mm* and the gap between the wires and the catode plane of 6 *mm*. The chambers have a 12 angular structure, and one module consists of 2 anode wire planes, two cover planes and three cathode planes, with the central one common to the two wire planes. A schematic drawing of the chamber is shown in Fig.2.14.
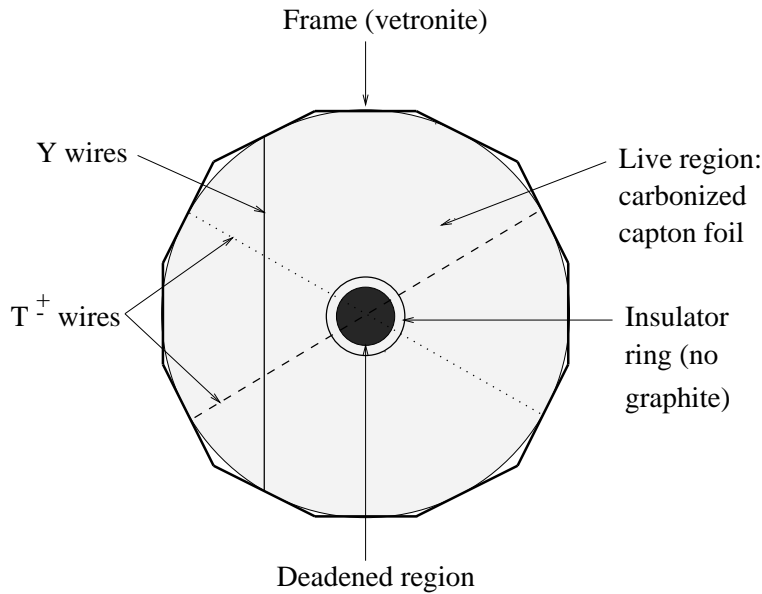

Figure 2.14: *Front view of the proportional chamber P67. The diameter of the sensitive area is* 90 *cm, the diameter of the deadened region is* 9 *cm. Insulation between the live and deadened region is obtained by removing the graphite layer. The width of the ring is* 0.6 *cm.*

There are four P67 modules, 8 wire planes in total, sandwiched between the modules of ST67. The chambers have a deadened central beam region with radius of 9 *cm*. This region is kept at lower voltage, such that the gas amplification is very low.
A special HV control system was developped for the chambers [76]. The controller increases the HV slowly, keeping a constant difference between the voltage applied to the

---

[1]Polymer sheets, 100 μm thick
[2]Made of gold plated $Cu - Be$ alloy, wire diameter 20 μm

live zone and the deadened region of the chamber. Safety devices were implemented to make sure, that: (1) the the difference does not become higher than 530 V, which would result in destruction of the insulator between the two zones, (2) in case of a malfunction of the HV system, to discharge the system to ground through a resistor and not through the chamber and (3) a fast ramp-down of the HV is made when the current in the chamber exceeds the preset maximum value. The last feature was implemented as a safeguard against a sudden change in the instantaneous beam intensity during spill. In such spills, the intensity could reach 2 to 3 times the average value.

The gas mixture for the chamber is a slight modification of the so called 'magic gas' to 74.69 % *Ar*, 24.1 % *Isobutane*, 0.42 % *Freon* and 0.79 % *Isoprophylic alcohol*. The alcohol acts as a cleansing agent for the wires and as a moisture absorber.

The chamber readout is based on the RMH system with preamplifier cards, which also act as a cable driver for the 120 m long delay cables, mounted on the chambers. The lenght of the cables, delaying the signal by 600 ns, is determined by the arrival time of the trigger, which opens the event gate. The last readout stage consists of 112 units of 32 channel RMH receiver cards grouped in 6 special crates. The total number of channels in P67 is 8064.

During the 4 years of operation, the P67 system was extremely stable, with plane efficiency above 95 %. Due to the sophisticated HV control system, it had never a broken wire.

2.4.6   Data acquisition and on-line control

The backbone of the SMC data aquisition is the ROMULUS readout standard [77]. It is a read-only CAMAC based system, with a communication protocol wich uses a subset of the standard CAMAC functions. The major modification over CAMAC consists of reading only significant (zero suppressed) data off the modules. This is made to speed up the readout time.

The ROMULUS crates in SMC are organized in a tree-like structure, with four branches. The branches have almost equal readout time and are read simultaneously. Each branch feeds the acquired information into an event buffer, housed in a FASTBUS crate. The only exclusion from this system is the ST67 readout, which due to the design properties of its STAS cards has to be housed in CAMAC and is independently connected to the FASTBUS. The data accumulated in the event buffers is processed after the beam spill has ended by a computer in the same FASTBUS crate, called the Event Builder. Through a interface module, the events are transferred to the main data acquisition computer (Micro VAX-III, DX) and written to a Exabyte 8 mm magnetic tape. Simultaneously, the same information is transferred to a second Micro VAX computer (EX) for online checks of several equipment parameters, the most important of them being:

- calculation of chamber and hodoscope efficiencies, made by the programs EFFY (for the big spectrometer chambers) and EFFYP0 (for the P0 chambers and the Beam hodoscopes).

- comparison of the hit frequencies of the wires in all chambers, TDC and ADC spectra to a reference distributions, made by the program FASTMON.

- the raw event structure is monitored by the program EQCHECK.

Some equipments have their dedicated check tasks, which verify the readout electronics and the data consistency.

The slow control of the SMC spectrometer is performed by a third Micro VAX (UX), which operates in the spill pauses. Programs monitor the working state of the low and high voltage power supplies, trigger matrices, readout modules. For example:

- the SCANNER program reads the output and compares to a preset values of almost all high and low voltage power supplies for the chambers. It also monitors the trigger crates low voltage supplies.

- HV units, usually CAEN type, which are not monitored by the SCANNER have their separate check programs.

- magnetic fields of the most critical magnets in the beam line are measured and compared to a set of default values by the program HALCHK.

- the trigger and veto hodoscope HV supplies are monitored by the NHVCHK program.

- the trigger matrix patterns are verified by the NHMT program. By pulsing LEDs, embedded in the trigger scintillators, the task checks the response of the photomultipliers in the trigger and veto hodoscopes.

Several programs verify in the pauses between the spills the status of the readout for single detectors by pulsing electronically the inputs of the front end cards and reading out the resulting pattern. These programs are used to debug readout malfunctions and for setting up the electronics before a data taking period, in the absence of beam.

The policy behind the check programs is to analyze as many parameters as possible and to compare them to a preset nominal values in order to assure stability of the spectrometer equipment over time. Wherever possible the same information is gathered in different ways by more than one program. Some of it is stored on disk or magnetic tape for subsequent off-line analysis.

2.5 Beam polarimeter

The SMC muon beam polarization is calculable by a Monte-Carlo simulation of the magnet transport. The program HALO [78] which was used to define the muon beam line setting also gives an estimation of the polarization of the muons at the entrance of the experimental hall, which at beam energy of 190 GeV is -0.785 ± 0.07. The error in this calculation is difficult to estimate, but stems mainly from the uncertainty of the momentum of the kaons and pions and their unknown proportions in the parent beam. Description of the physics principles, used for the simulation, are given in [79] and [80].

For the SMC experiment, the error on the beam polarization as estimated in the Monte-Carlo would have been the dominant source of systematic uncertainty, therefore a measurement of the beam polarization was carried out by a dedicated beam polarimeter with the aim to reduce the error on the polarization below ± 0.04. Two different experimental methods were used:

- **Decay method** - based on the dependence of the energy of decay positrons on the polarization of the parent muon from the process $\mu^+ \rightarrow e^+ + \bar{\nu}_\mu + \nu_e$.

- **Scattering method** - muon polarization is obtained through a measurement of the cross-section asymmetry for the process $\mu^+ + e^- \rightarrow \mu^+ + e^-$, elastic scattering of longitudinally polarized muons on longitudinally polarized electrons in a magnetized iron foil.

The beam polarimeter is located downstream of the main spectrometer and took data simultaneously with it. Figure 2.15 shows the experimental setup used for both methods.
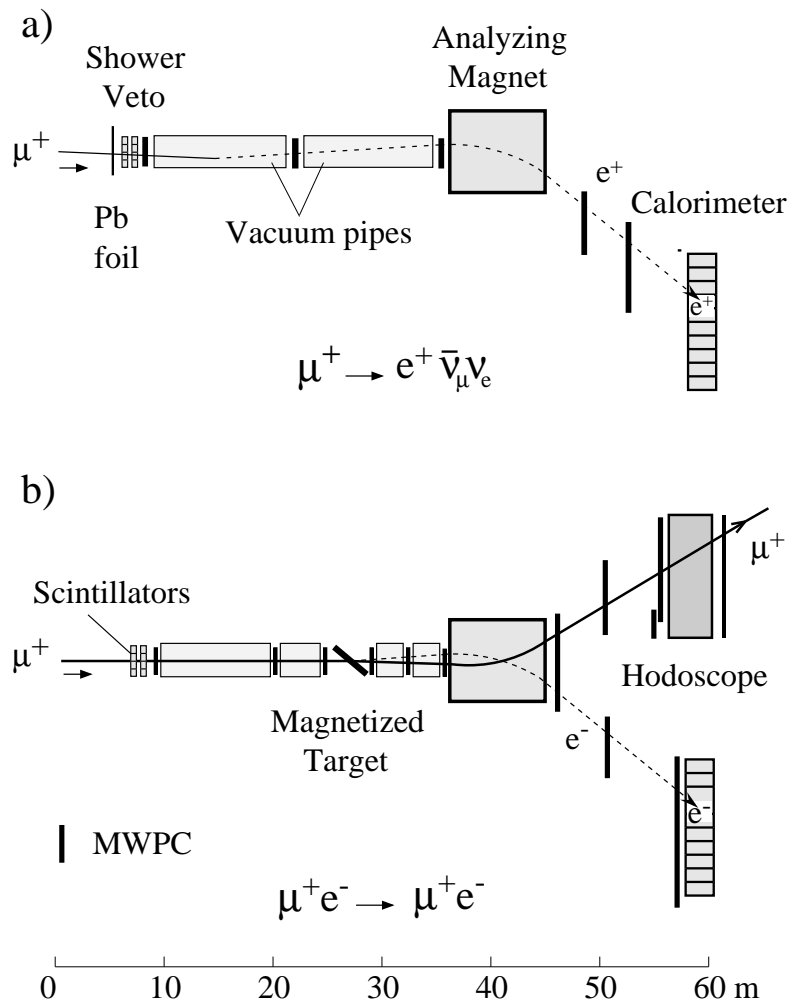

Figure 2.15: *Beam polarimeter setup used for the* **decay method** *(a) and for the* **scattering method** *(b). Most of the detectors are common for both methods.*

2.5.1 Measurement of the beam polarization through muon decay

The positron energy spectrum wich results from decay of muons with energy E_μ and longitudinal polarization P_μ is called Michel Spectrum [81,82] and, expressed in terms of positron to muon energy ratio $y = E_e/E_\mu$, is in laboratory frame:

$$\frac{dN}{dy} = N_0 \left[\frac{5}{3} - 3y^2 + \frac{4}{3}y^3 - P_\mu \left(\frac{1}{3} - 3y^2 + \frac{8}{3}y^3 \right) \right], \tag{2.6}$$

where N_0 is the number of muon decays and P_μ the muon polarization. The polarization dependence of the Michel spectrum results from the fact, that in the rest frame of the muon the positron is preferentially emitted in the direction of the muon spin. The muon polarization is measured through the ratio y, where both E_μ and E_e are determined for each event. The incoming muon energy is measured by the BMS (see section 2.2.1) and the muon track and the positron energy is measured by the polarimeter apparatus.

There are 5 main detector groups in the experimental setup for the decay method. The **Shower veto (SV)** consists of a 8 mm thick lead foil and two hodoscope planes with strips oriented in vertical and horizontal direction. It distinguishes between electrons and muons entering the polarimeter. Electrons interact with the lead and show a high multiplicity and thus large energy deposit in the scintillators while muons only show a minimum ionizing trail. Signals from both planes of the SV are required in the trigger and the pulse-height information is used to discriminate positrons, produced upstream of the detector. Following the SV is a 35 meters long **Vacuum pipe** in which a fraction of the beam muons decay. The absence of air reduces the probability of bremsstrahlung background. Three 1 mm pitch proportional chambers are placed in the beginning, the middle and at the end of the pipe to track the muon and the decay positron. Behind the vacuum pipe is the **Analyzing magnet** in which the positron is bent towards a spectrometer. The magnet is a 6 m long air-core dipole with precisely mapped magnetic field. The deflected positrons enter an array of 2 mm pitch proportional chambers, used for tracking and subsequently their energy is measured in a **Lead glass calorimeter (LG)**. The calorimeter consists of a 10×3 array of lead glass blocks, each of them $10 \times 10 cm$ and 30 radiation lengths long. The last element in the setup is the **Veto lead counter (VLC)**, which is a 20 cm thick lead wall followed by a 16 element scintillator hodoscope. Its function is to identify muons, which deposit some of their energy in the LG and may be confused with electrons.

The beam polarization is determined from the shape of the positron Michel spectrum, after several corrections to the raw spectrum: (1) the acceptance of the spectrometer, determined from a detailed Monte-Carlo simulation which takes into account the chamber layout and efficiencies and the muon beam polarization and phase space; (2) the radiative corrections to the decay process which turned out to be quite important, decreasing the polarization value by 0.07.
A fit to the corrected Michel spectrum in the y range $0.3 \leq y \leq 0.65$, where the acceptance variations are estimated to be smaller than 5 %, yields for the muon beam polarization:

$$P_\mu = -0.777 \pm 0.024 \text{ (stat.)} \pm 0.030 \text{ (syst.)} \tag{2.7}$$

Full description of the analysis procedure and the contributing systematic errors in the measurement are given in [83,84,85].

Figure 2.16(a) shows the theoretical curves for the positron energy spectrum for three different longitudinal muon polarizations. Figure 2.16(b) shows the measured and corrected positron energy spectrum for 190 GeV beam energy with the fit to the data, from which the actual muon polarization is determined.
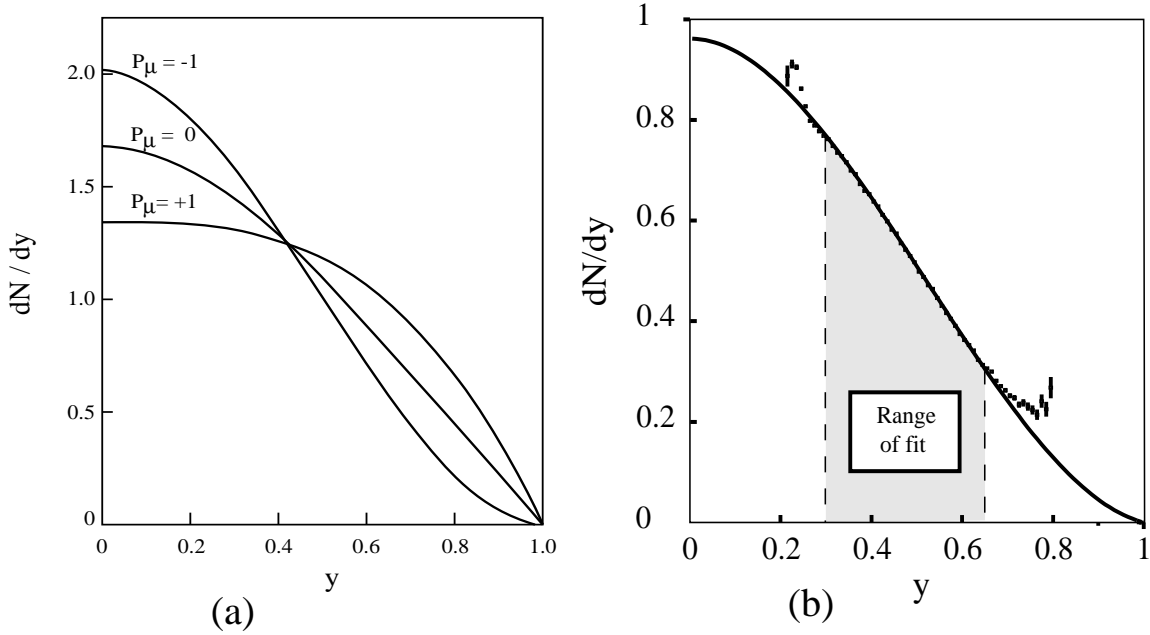

Figure 2.16: *(a) The Michel spectrum as a function of the positron to muon energy ratio y for three longitudinal beam polarizations. (b) Measured Michel spectrum with applied radiative and spectrometer acceptance corrections. The beam polarization is determined using a fit to the data in the region of minimal variation of the acceptance.*

2.5.2 Measurement of the polarization through muon-electron elastic scattering

The second method used in SMC to measure the beam polarization is the muon elastic scattering on a polarized electron target, realized with a magnetized feromagnetic foil, which is a similar method to the M⊘ller scattering used to measure the polarization of an electron beam [86]. The kinematics of the process is described by the variable

$$y = \frac{E_e}{E_\mu} \leq Y = \frac{2m_e E_\mu}{2m_e E_\mu + m_\mu^2} \approx 1 \quad . \tag{2.8}$$

The polarization of the muons is extracted from the experimental counting rate asymmetry for antiparallel ($\uparrow\downarrow$) and parallel ($\uparrow\downarrow$) orientations of the incoming muon and target electron spins [87]:

$$A^{exp}(y) = \frac{N^{\uparrow\downarrow} - N^{\uparrow\uparrow}}{N^{\uparrow\downarrow} + N^{\uparrow\uparrow}} = P_\mu P_e A_{\mu e}(y), \tag{2.9}$$

43

P_e being the target polarization, which is known, P_μ the beam polarization and $A_{\mu e}$ the cross-section asymmetry. In terms of y and Y the cross-section asymmetry is given by:

$$A_{\mu e}(y) = y \frac{1 - y/Y + y/2}{1 - y/Y + y^2/2} \qquad (2.10)$$

The polarimeter setup (Fig.2.15(b)) uses largely the same equipment as used for the muon decay measurement. Additional 1 mm pitch proportional chambers were installed between the shower veto and the analyzing magnet, improving the tracking of the incoming muons and the vertex reconstruction after the magnetized target. After the analysing magnet, the muon and electron trajectories are tracked in a two-arm telescope with a big proportional chamber shared between them. The muon is identified in a scintillator hodoscope, placed behind a 2 m thick iron absorber, the electron is detected in the lead glass calorimeter. The presence of a beam muon, a hit in the lead glass calorimeter depositing energy ≥ 15 GeV and a hit in the muon hodoscope form the event trigger.

The polarized electron target is made of 2.7 mm thick feromagnetic alloy foil, placed in a saturated field of 2.3 T. The foil is inclined by an angle of 25° with respect to the beam direction, which creates a component of the electron polarization parallel to the beam [1]. The field in the magnet is reversed each spill and the inclination of the target is reversed each hour from 25° to -25° and back to compensate for the false asymmetry created by the vertical component of the magnet bending. The cancellation of the false asymmetries is made by averaging the measured asymmetries obtained with the two target orientations. Target electron polarization was determined from the magnetic properties of the target composants and the field of the target magnet [88]. The component of the polarization along the beam direction was found to be $|P_e| = 0.0756 \pm 0.008$.

The largest contributing systematic errors are the uncertainty in the target polarization calculation, background from pair production $\mu^+ \to \mu^+ e^+ e^-$, bremsstrahlung $\mu^+ \to \mu^+ \gamma$ with a pair production $\gamma \to e^+ e^-$ where the electron was not identified, false asymmetries and muon flux normalization. The background was studied using a μ^- beam and was found to have a y dependence which distorts the shape of the measured asymmetry. The measured asymmetry, after applying radiative and background corrections, was fit to the theoretical asymmetry of Eq.2.10 with P_μ left as a free parameter. Fig. 2.17 shows the beam polarization, obtained by comparing the theoretical asymmetry $A_{\mu e}$ and the experimentally measured A_{exp}: $P_\mu = A_{\mu e}/A_{exp} P_e$.

The result for the beam polarization for 190 GeV beam from the scattering method is:

$$P_\mu = -0.78 \pm 0.03 (\text{stat.}) \pm 0.02 (\text{syst.})$$

The $\mu - e$ scattering method proved to be less sensitive to efficiency fluctuations in the experimental setup, shows consistency with the Monte-Carlo simulation and is better understood in terms of corrections to the measurement than the decay method. Therefore, the beam polarization value used later in this thesis as an input to the asymmetry calculations is the number obtained by the scattering method.

---

[1] 25° is the inclination angle at which the magnet yoke is still outside the beam.
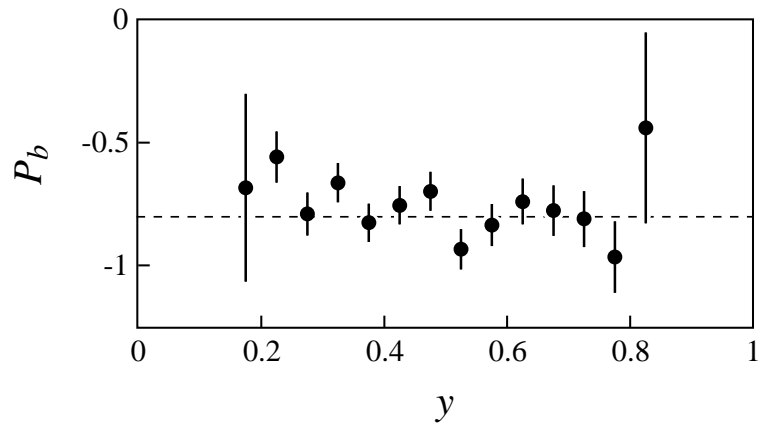
Figure 2.17: *Polarization of the beam as a function of y for beam energy of* 190 *GeV.*
The dotted line is the average value of the beam polarization.

3 Analysis of the experimental data

3.1 Introduction

The path from the raw data, recorded by the SMC spectrometer, to the final physics analysis involves several key steps, which are described below. Generally, the main emphasis was put on obtaining reliable data by online monitoring of important detector parameters and promptly analysing offline the collected samples. All hardware deficiencies, found by both methods were corrected almost immediately. This system of checks allowed fast and efficient physics analysis with a very clean final sample and low amount of data discarded. The following sections deal with the different types of data obtained and their particular use. Discussed are the software packages employed in the data evaluation and the differences introduced in the standard SMC tracking routines, relevant for the A_2 analysis. The input information, needed to obtain the final asymmetries, is also presented.

3.2 Data processing scheme

The first step of the scheme begins with the raw data collected with the spectrometer. There are 4 distinct types of data samples collected:

- Physics data - nominal beam intensity: 4.5×10^7 $\mu/pulse$, the spectrometer is in optimal running conditions, all physics triggers are active.

- Alignment data - low beam intensity: 5×10^5 $\mu/pulse$ (low chamber multiplicity, one particle track only), forward spectrometer magnet off (straight tracks), some spectrometer chambers with special settings, only the relevant alignment trigger is active. The data collected are used to align the spectrometer apparatus with respect to a reference point in the experiment's coordinate system.

- Calibration data - nominal beam intensity, optimal running conditions, only the relevant calibration trigger is active. These data are taken for beam hodoscopes (BHA, BHB), beam momentum station (BMS) and trigger hodoscopes TDC calibration.

- Special data - Various beam intensities, special setting for the spectrometer apparatus, various triggers. The data are taken for high voltage efficiency plateauing of the chambers, investigation of the behaviour of certain parts of the spectrometer as a function of beam intensity, timing of hodoscopes, special efficiency runs, etc.

Figure 3.1 shows the full data analysis chain for the SMC data and the standard data production chain with all the inputs to the various programs.
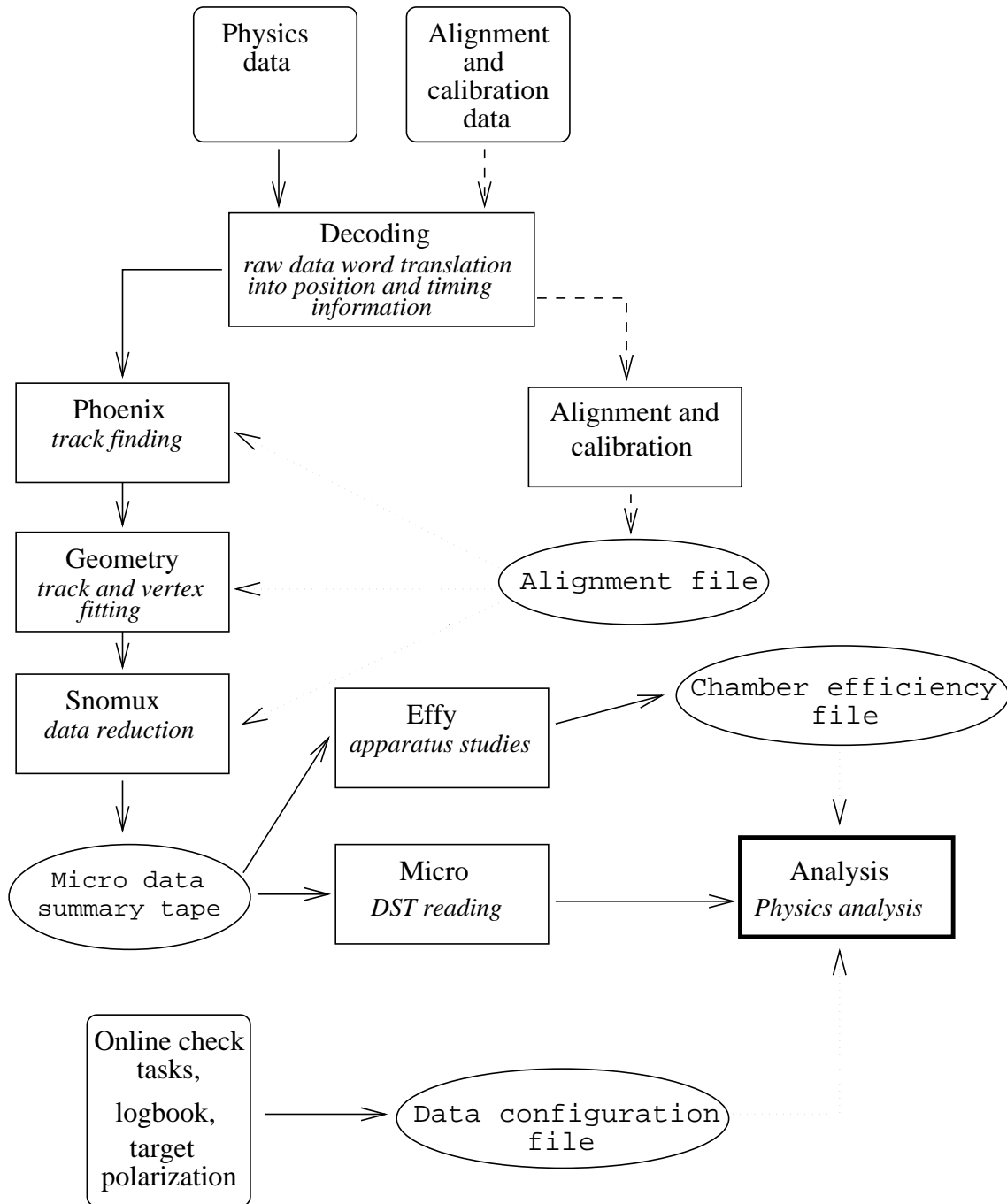

Figure 3.1: *Block scheme of the SMC data analysis chain. The inputs from the experiment are shown in rounded boxes, the analysis software is shown in rectangular boxes and the information files are shown in ellipses.*

3.3 Program packages

The SMC software processing begins with the decoding program. It translates the raw data words from the spectrometer equipment into position (wire number, hodoscope element with signal) and timing (drift and TDC times) information. The program sorts the decoded data by detector type and fills the relevant information banks [1] for subsequent use by the reconstruction software.

The program Phoenix does the initial track segments and track finding. After validating the trigger by checking that there is sufficient information provided by the trigger hodoscopes, it looks for a beam track in the beam momentum station (BMS) and the beam hodoscopes (BH). Once the beam track is found, the deflected muon track is reconstructed first in the section behind the hadron absorber in the ST67 and P67 detectors. This segment is then matched with the segments found in front of the absorber wall in the W45-P45 detector groups and further upstream in the W12-P0E and P123-P0D chambers. The segment closest to the target is provided by the information in the PV1-PV2-P0C group. Any associated tracks which are in the trigger time window and do not penetrate the hadron absorber are identified as hadrons. An event from trigger 1, reconstructed in Phoenix, is shown in Fig.3.2.

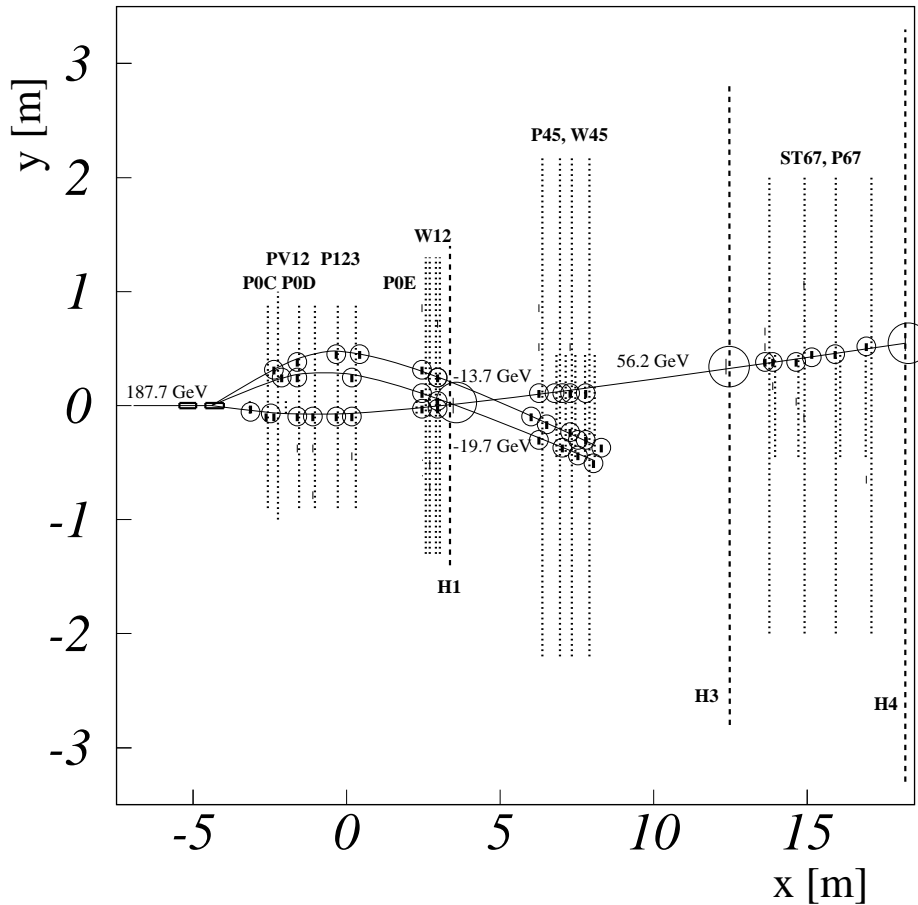Figure 3.2: *Top view (x-y coordinates) of a reconstructed track segments in Phoenix from a typical Trigger 1 event. There are 2 hadron and 1 muon tracks. Hits in the chambers, associated with those tracks are circled. The pads of the trigger hodoscopes H1, H3 and H4 which form the trigger are also shown.*

---

[1]SMC uses ZEBRA [115,89] data manager as an interface between the different software packages

A failure to verify the trigger or reconstruct a track segment in any of the detector groups outlined above leads to the reject of the event. The muon track reconstruction efficiency of the various detector groups is given in table 3.1 and is defined as number of successfully reconstructed tracks over the number of triggers. In this table each efficiency line is a percentage of the line above. Typical number of raw triggers on the input of Phoenix from a physics run is: 12000 Tr.1, 4500 Tr.2, 8000 Tr.14.

Detector Group	Tr.1 (%)	Tr.2 (%)	Tr.14 (%)
TRIGGER HODOSCOPES efficiency	99.9	96.3	99.9
BEAM reconstruction efficiency	97.4	99.2	99.6
ST67/P67 reconstruction efficiency	83.2	69.1	84.3
W45/P45 reconstruction efficiency	93.5	94.3	96.9
W12/P0E reconstruction efficiency	97.2	96.5	95.6
MAGNET reconstruction efficiency	85.5	90.5	87.8
PVP0C reconstruction efficiency	94.2	93.7	92.3
PHOENIX muon reconstruction efficiency	59.3	50.9	63.0

Table 3.1: *Summary table of the Phoenix muon reconstruction efficiency for the physics triggers, divided in detector groups for RUN 16660 in period P2E95.*

The somewhat lower trigger 2 hodoscope efficiency is due to an electronics readout problem, where sometimes a trigger gate was generated and passed to the detectors, but no hits were recorded in the hodoscope pattern units [90]. The ST67-P67 efficiency is lower due to the shortcoming in the efficiency definition - the denominator in the calculation is artificially high, since at this level the trigger is only verified to fulfill the hardware requirement of at least one hit in all trigger planes. Subsequent groups are less affected, because if there is no track segment reconstructed in the ST67-P67 detector group, the event is abandoned. The Magnet group (chambers P1, P2, P3A and P3B) efficiency is lower because not all tracks found behind the magnet continue in the direction of the target and hence cannot be joint with a track segment found upstream which originates in the target.
All of the experiment's hardware and software was constantly improved over the period of running of SMC which resulted in substantial increase of the reconstruction efficiency and subsequently of the data sample for physics analysis.
If all track segments from the muon identification section up to the target are found, the information is passed to the next software package - the Geometry. A more refined trigger check is performed on this level, based on the coincidence matrix pattern of trigger 1 and the geometric layout of trigger 2 and 14. The track segments are joined and the muon identification is made by matching the tracks in the muon section with those in front of the absorber. Geometry performs a refit of the entire track, calculates the kinematic characteristics of the event and determines the interaction vertex in the target volume.

All this information, together with the raw data, is written into a temporary file - the Geometry data summary tape. The table 3.2 summarizes the efficiency of the Geometry software package. For this table the efficiency is defined as number of successful software steps over the number of input events.

The task of the program package Snomux is to reduce the rather substantial data volume after Geometry and to sort and write out in ZEBRA format the final muon data summary tape (μDST) which contains all necessary information for physics analysis. It does not perform any data correction, therefore its efficiency is 100 %. The reduction factor for the data volume from raw data to μDST is 75. This allows all μDST's to be stored on computer hard disks, instead of EXABYTE tapes, which allows for quick and efficient analysis.

There is further data sample reduction on the level of the Micro program, associated with the physics cuts. They are discussed in section 4.8.

Software Group	Tr.1 (%)	Tr.2 (%)	Tr.14 (%)
BEAM reconstruction efficiency	97.0	97.2	96.3
Muon (linker+Spline) rec. efficiency	96.0	95.1	90.0
Muon Trigger Checking efficiency	78.9	94.1	91.2
Muon Vertex efficiency	78.0	80.8	72.4
Global GEOMETRY efficiency	57.3	70.3	57.5

Table 3.2: *Summary table of the Geometry package efficiency, divided in program groups for RUN 16660 in period P2E95.*

3.4 Alignment and calibration procedures

A precise knowledge of the positions of all elements of the spectrometer in the SMC coordinate system is essential for the correct operation of the reconstruction software. The alignment procedure determines the detector positions, relative to each other, to the target and the FSM magnetic field. It consists of two stages, where the first one is the optical surveying of a reference point on each detector group or hodoscope to determine its x position (along the beam) with respect to the zero coordinate point - the center of FSM. Knowing the detector construction parameters, the x position of the individual wire and hodoscope planes is calculated. The second stage consists of the iterative alignment of every chamber and hodoscope plane in y and z coordinates, using alignment data, collected under special conditions [64].

The alignment runs are taken with no magnetic field in the FSM, low muon intensity and with a trigger (Tr.5 and Tr.7) reacting to the muon halo. The first condition is needed in order to be able to predict the track position accurately at the chamber and hodoscope planes, which is easier with straight tracks. The second condition ensures low detector multiplicities to avoid ambiguities in assigning hits to the track. The muon halo is parallel to the beam and therefore at 90 degrees to all detectors in the SMC spectrometer.

In the alignment procedure a track is first reconstructed in a reference detector group, for which the plane and wire positions in the SMC coordinate system are known with high precision from optical survey and detector construction. The reconstructed track is extrapolated to a detector whose position is to be determined. The correction for a given detector plane is calculated from the difference between the extrapolated position of the reference track and the position shown by the plane. This process is repeated for all planes of the SMC detectors.

Since there are several detector groups in the spectrometer, covering different areas of acceptance, it is necessary to align them relative to each other. For example, the P0 chamber group covers the deadened regions of the bigger proportional and drift chambers and the overlap between them is small. The same is true for the triggers, Tr.7 covering the middle and outer regions of the big chambers and Tr.5 covering the active area of the P0 chambers and the beam hodoscopes. Therefore there is no data sample allowing simultaneous alignment. As a remedy to this situation some of the detectors (PV2, P45, P67) have a special HV supply system, which permits the deadened regions to be activated by applying sufficiently high HV. Thus Tr.5 provides a mixed sample for alignment of the central regions of the big proportional chambers, P0 detectors and the beam hodoscopes. The precision of the procedure allows to align the various wire planes to an accuracy of order of 0.5 mm in y and z coordinates, which is better than the plane resolution itself. Since the reconstructed tracks are perpendicular to the planes, it is not possible to extract the x position from the data, therefore it has to be provided accurately by the optical surveying.

Several detectors in the spectrometer require precise timing calibration. Those are the scintillator hodoscopes, equipped with TDC's: BMS, BH, Trigger hodoscopes and the drift chambers W12 and W45. The timing information from the hodoscopes is used to associate the various elements of an event, for example the correlation of the BMS and BH tracks is made purely on a time window basis and an additional correlation is required with the timing, provided by the H3V hodoscopes for Tr.1 events.

The TDC calibration procedure for BMS and BH is performed with data collected with Tr.5 and consists of calculating the offset of each individual channel with respect to a reference zero point. This procedure yields a T_0 offset coefficient for all elements. The H3V hodoscope is calibrated using Tr.7 data and since, because of their length, the H3V strips are equipped with TDC's on both ends, the T_0 offsets are calculated such that the the $T = 0$ time is at the center of the strip, which corresponds to coordinate $z = 0$.

The drift chambers calibration is an iterative procedure, which tunes two characteristic parameters - T_0, which is the maximum drift time originating from a particle passing close to the potential wire and v_d, which is the drift velocity. The procedure starts with an approximated T_0 and v_d. In the region of linear drift field these two paramaters can be extracted from a plot of the distance of the track projection from the signal wire versus the drift time, measured by the drift time recorder (DTR) electronics. On such a plot T_0 is the intercept on the time axis and v_d is the slope. For the areas with a non-linear drift field a polynomial fit is used to describe the deviation of the residual from a straight line. The residual is calculated as a distance between the actual hit in the drift cell and the reconstructed position using the initial T_0 and v_d. The degree of the polynominal depends on the uniformity of the field and gas mixture. The drift chambers calibration procedure yields a set of T_0, v_d and polynominal coefficients for each detector plane.

The alignment and calibration of the whole SMC spectrometer equipment is performed in

general each month during data taking and for a particular detector each time an important parameter has changed, like a HV setting, replacement of a TDC module or when a detector is moved from its original position for repairs.

3.4.1 Corrections to the beam track finding algorithm for the measurement with transverse target polarization

For the period of data taking with transverse target polarization (P2E95) the dipole magnet of the target introduces a kick in the particle trajectory in the (x, y) coordinate plane, which has to be compensated. This is done by a bending magnet (B11) placed before the polarized target (see Fig.2.10). Since the bending occurs in the beam track reconstruction section of the spectrometer, between BHA and BHB/POB detectors, its deflection has to be taken into account in the reconstruction algorithm. Figure 3.3 illustrates the modification to the track reconstruction introduced by B11.
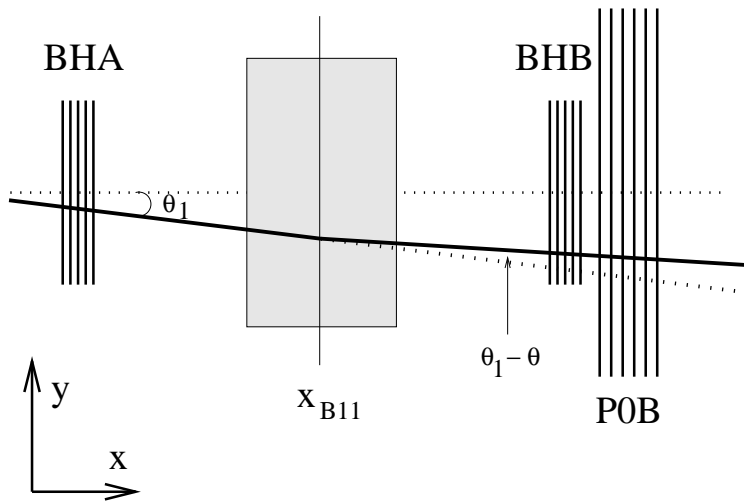

Figure 3.3: *Reconstruction scheme of the beam particle track in period P2E95 with a bending magnet, installed between BHA and BHB/P0B detectors.*

The track parameter for the y projection at BHB/P0B is calculated through a fit, using the two line segments before and after B11

$$y_{B11} = y_{BHA} + (x_{B11} - x_{BHA})tg\Theta_1 \tag{3.1}$$

$$y_{BHB/POB} = y_{B11} + (x_{BHB/POB} - x_{B11})tg(\Theta_1 - \Theta) \tag{3.2}$$

where $x_{BHA/BHB/P0B}$ is the x-position of the y planes of the detectors, x_{B11} is the x-position of the center of B11, Θ_1 is the inclination of the track segment before B11 and Θ is the bending angle of B11, calculated through

$$\Theta = \frac{0.3(\int B\mathrm{dl})}{P_{beam}}. \tag{3.3}$$

For 190 GeV beam, at a current $I = 340.6$ A, the B11 bending power is 1.98 Tm. This corresponds to a bending angle $\Theta = 3.13$ $mrad$.

The test of the new tracking procedure was done by taking calibration data with variable bending power of B11 and no magnetic field in the target in order to use the rest of the P0 chambers for a more accurate track prediction of the segment downstream of B11. For each of the bending values, two differences were calculated: between the hits in the planes of P0B and the predicted impact point, once using the tracking which takes into account the bending in B11 and once using a straight line fit as in the standard programme. The two results are shown in Fig.3.4(a), where the open squares represent the corrected points and the filled squares are the uncorrected points. Figure 3.4(b) shows the residual distribution for the corrected y-projection at plane P0B y_1 minus the actual hit in the plane, together with a gaussian fit to it. The mean is -0.010 ± 0.003 mm, $\sigma = 0.559 \pm 0.002$ mm. For all other planes of P0B these values are similar.

There is no evidence of non-uniformity of the magnetic field of B11 and the correction algorithm for the y-position of the hits in P0B and BHB shows sufficient accuracy, well within the resolution of the detectors.
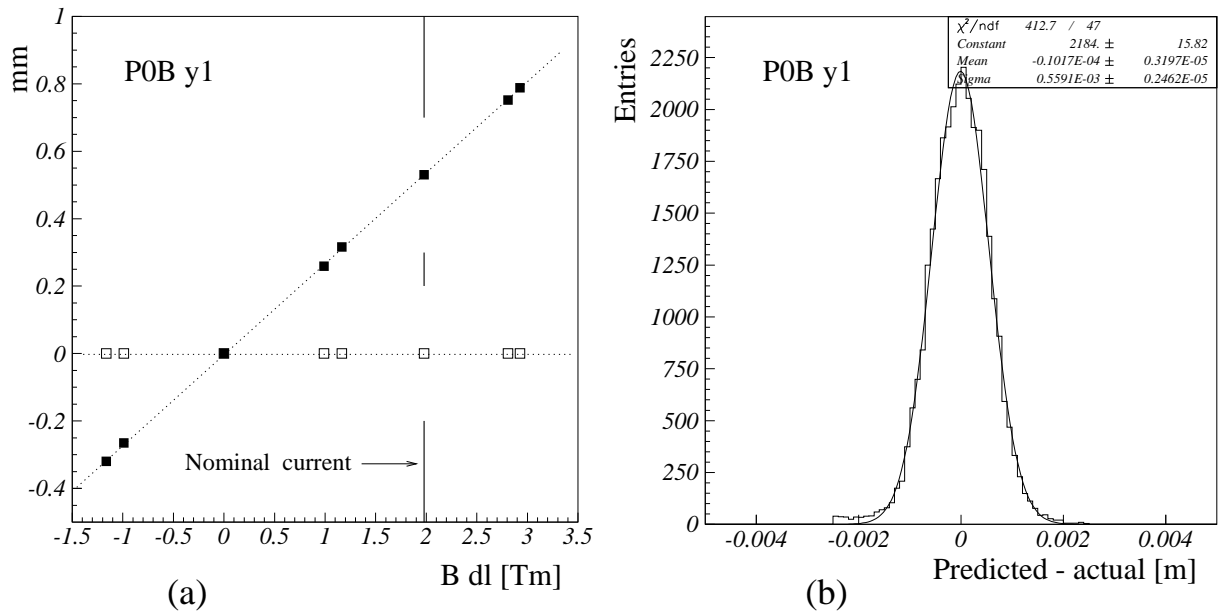

Figure 3.4: *Verification of the correction algorithm for the displacement of the beam track introduced by B11. (a) Open squares represent the points corrected with the algorithm for each $\int B$dl of B11. Filled squares show the uncorrected results from the standard beam track reconstruction algorithm. (b) Residual distribution of predicted - actual position for the nominal bending power of B11 1.98 Tm*

3.4.2 Detector efficiencies

The stability of the spectrometer reconstruction efficiency over time is of a crucial importance for the correct asymmetry measurement. Therefore several programs were developped to study the chamber and trigger efficiency performance. Plane and detector group efficiencies are studied from the information available on the Micro data summary tape (μDST), which contains the reconstructed track information, verified for acceptance,

trigger validity and vertex, together with hit information for the detector planes on its path. The plane efficiency is defined as a ratio of the number of times the plane had a contribution to the track, $N_{success}$, divided by the total number of tracks, N_{total}:

$$\epsilon_{plane} = \frac{N_{success}}{N_{total}}. \tag{3.4}$$

A bias in this definition is introduced if the investigated plane is involved in the reconstructed track. It can be taken out by using track subsets which are reconstructed without the support of the plane. Such a subset is identified by using the minimum plane requirement parameters. These are set of numbers, like a certain minimum number of planes and their orientation, used by the reconstruction software to detect a track in a given detector group. The exclusion of the plane for which the efficiency is calculated is made by verifying that the minimum plane requirement for its detector group is also fulfilled when this plane is not taken into account.

Further refinement of the efficiency calculation is needed since for some of the detectors it is not uniform over the whole sensitive area. Mostly there is a radial dependence with efficiencies decreasing towards the center of the planes. The following efficiencies are calculated:

- for a given detector area - inner region (close to the beam), outer region and the total region.

- radial dependence.

- for each physics trigger.
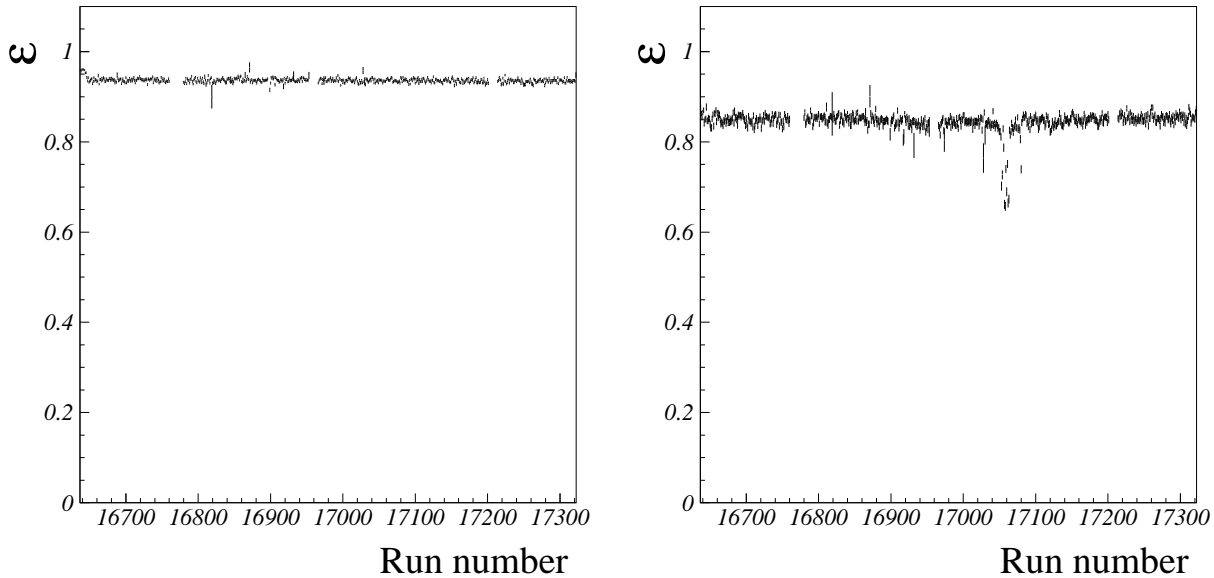
- versus time (run number).

Figure 3.5: *Trigger 1 run dependent global plane efficiencies for the period P2E95 of P0B Y1 (a) and W45 Y1 (b).*

54

Two plane efficiencies of SMC detectors are shown in Fig.3.5: (a) shows the global efficiency of P0C plane Y1, (b) shows the global efficiency of W45 plane Y1. The erratic behaviour between runs 17047 to 17065 is due a faulty HV supply to this plane. Other planes in the detector do not show this dip and the track reconstruction efficiency of the W45 detector group is not affected.

From similar distributions for all detectors the intervals of stable efficiencies are identified and used consequently as an input for appropriate data combination in the asymmetry calculation programs. Runs with unstable efficiencies are not used in the analysis and time intervals which have different efficiency values are not combined together.

Another important application of the chamber efficiencies is using them to estimate changes in the spectrometer acceptance from the changes in the detector groups efficiencies over time. This method is described in section 5.3.2g.

4 Formalism of the $A_\perp$ asymmetry extraction

As outlined in section 1.2.4 the experimentally measured quantity is the cross-section asymmetry $A_\perp(\phi_0)$ constructed from the differential cross-section $\sigma^{\leftarrow\Uparrow}$ for values of the azimutal angle ϕ_0 and $\pi - \phi_0$:

$$A_\perp(\phi_0) = \frac{1}{2}\frac{\Delta\sigma_\perp}{\overline{\sigma}} = \frac{1}{2cos\phi_0}\frac{\sigma^{\leftarrow\Uparrow}(\phi_0) - \sigma^{\leftarrow\Uparrow}(\pi - \phi_0)}{\sigma^{\leftarrow\Uparrow}(\phi_0) + \sigma^{\leftarrow\Uparrow}(\pi - \phi_0)}, \tag{4.1}$$

where $\overline{\sigma}$ is the spin-independent differential cross-section and the azimutal angle is restricted to the interval $-\frac{\pi}{2} \leq \phi_0 \leq \frac{\pi}{2}$.

4.1 Event yields

The first step in the evaluation of the cross-section asymmetry $A_\perp$ is the extraction of event yields N from a given part of the spectrometer. N is defined as the total number of muons, scattered from a target cell into an azimutal angle range ϕ_0 to $\phi_0 + \Delta\phi$ and it is related to $A_\perp$ through:

$$N(\phi_0) = \Phi n_u \sigma_u a \left(1 - f\ P_\mu\ P_t\ cos\phi_0\ A_\perp\right)\Delta\phi_0 \tag{4.2}$$

where Φ is the time integrated muon flux, a is the spectrometer acceptance, P_μ and P_t are the beam and target polarization. The average cross-section for the unpolarized target material σ_u and the total number of nucleons per unit area n_u are given by:

$$\sigma_u = \frac{n_d\overline{\sigma} + \sum_A n_A\sigma_A}{n_u} \qquad n_u = n_d + \sum_A n_A \tag{4.3}$$

The sum runs over all nuclei A in which the unpolarized nucleons are bound, with their correspondent nucleon number n_A and cross-sections σ_A. f in Eq.4.2 is the dilution factor, which accounts for the fraction of events originating from other than the polarizable material in the target. It be discussed in more details in section 4.5.

4.2 Event yields from one target cell

The SMC polarized target consists of two target cells, which are oppositely polarized and their polarization is orthogonal to the muon spin vector. The extraction of $A_\perp$ is done separately for each target cell and is identical for both, therefore the formalism will be discussed for one target cell only.

The observed asymmetry depends only on the azimutal angle ϕ. As presented in Fig.1.2, ϕ is defined as the angle between the plane of the muon and nucleon spin vectors and the plane of the incident and scattered muon momentum vectors. The calculation of ϕ is made with respect to the target polarization vector, which alternates in the coordinate system of the experiment between z(up) and $-z$(down). The event yields calculation takes advantage of the mirror symmetry in the spectrometer acceptance. As it will be explained later in this chapter, this symmetry is also beneficial for the minimization of systematic effects due to reconstruction efficiency instabilities. The yields as a function of the azimuthal angle in the upper and lower part of the spectrometer, before and after the polarization in the target cell is reversed are given by:

$$N_{up}(\phi_0) = \Phi n_u \sigma_u a_{up}(\phi_0) \left(1 - f\ P_\mu\ |P_t|\ cos\phi_0\ A_\perp\right) \tag{4.4}$$

$$N_{lo}(\phi_0) = \Phi n_u \sigma_u a_{lo}(\phi_0) \left(1 + f\ P_\mu\ |P_t|\ cos\phi_0\ A_\perp\right) \tag{4.5}$$

$$N'_{up}(\phi_0) = \Phi' n_u \sigma_u a'_{up}(\phi_0) \left(1 + f\ P_\mu\ |P'_t|\ cos\phi_0\ A_\perp\right) \tag{4.6}$$

$$N'_{lo}(\phi_0) = \Phi' n_u \sigma_u a'_{lo}(\phi_0) \left(1 - f\ P_\mu\ |P'_t|\ cos\phi_0\ A_\perp\right) \tag{4.7}$$

The subscripts signify $_{lo}$ for the lower spectrometer part ($z < 0$), $_{up}$ for the upper spectrometer part ($z > 0$) and *primed* are the quantities after target polarization reversal. The identity $cos(\pi - \phi_0) = -cos\phi_0$ is used in Eq.4.5 and Eq.4.6. The rotation of the target polarization does not influence the acceptance definition of the spectrometer, since it is defined always in its upper or lower part. The calculation of ϕ takes into accounts the polarization direction, therefore only the absolute value of P_t appears in the equations.

Fig.4.1 illustrates the event yields and acceptances definition and its dependence on the azimutal angle ϕ. The beam vector points into the page.

4.3 SMC method of asymmetry evaluation

The system of equations 4.4 to 4.7 contains many unknown quantities and only one of interest: $A_\perp$. To reduce the number of parameters, the redundancy of the system can be used, together with the knowledge of the experimental conditions. Studies of possible extraction [92,93] address the questions of the acceptance stability of the spectrometer with respect to possible false asymmetries, the different analysing power of events in the same x bin due to the varying depolarization d and dilution f factors with Q^2. The Monte-Carlo simulation is used in [91] to study the possible data combination in (x, Q^2) bins and estimate biases, caused by the small number of events in a given bin.

The method for data combination adopted in this thesis is based on the technique of weighting each event with a factor proportional to its analysing power and thus avoiding

the (x, Q^2, ϕ) binning and together with that the necessity to average f, d and $cos\phi$ over the bins. It is called the $fd\cos\phi_0$ method.
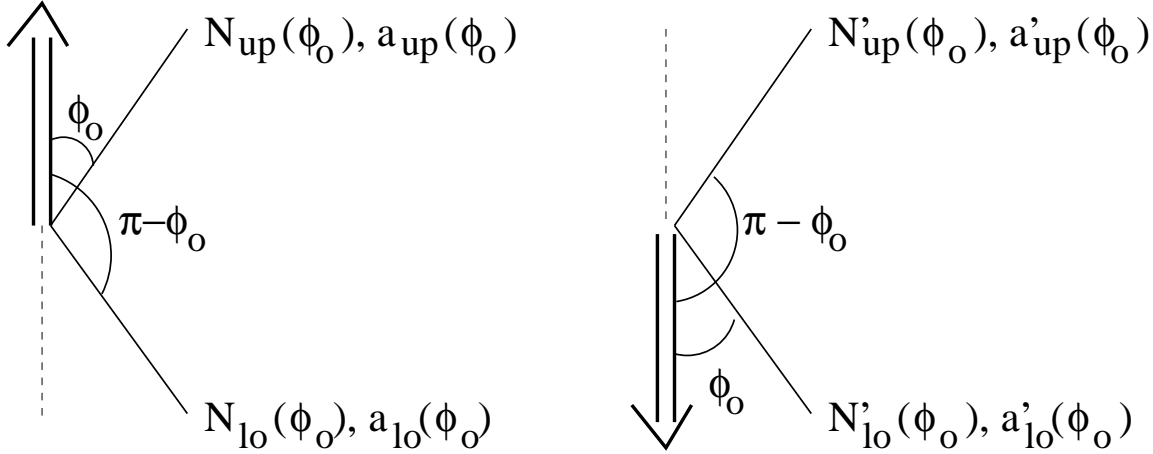

Figure 4.1: *Event yields and acceptances as a function of the azimuthal angle ϕ before polarization reversal (left) and after polarization reversal (right) for the SMC method of extraction of the asymmetry $A_\perp$.*

Through this method the asymmetry $A_\perp$ is exctracted in infinitesimally small x, Q^2 and ϕ bins, such that the f, d and $cos\phi_0$ variations within the bins are small. In practice it is done by weighting the events with their analysing power, which is [23]

$$w = (fd\cos\phi_0)^2. \tag{4.8}$$

The formalism in this case is based on constructing counting rate asymmetries from the ratios of event yields before (A_{N1}) and after (A_{N2}) polarization reversal:

$$A_{N1}(\phi_0) = \frac{N_{up}(\phi_0) - N_{lo}(\phi_0)}{N_{up}(\phi_0) + N_{lo}(\phi_0)} \tag{4.9}$$

$$A_{N2}(\phi_0) = \frac{N'_{up}(\phi_0) - N'_{lo}(\phi_0)}{N'_{up}(\phi_0) + N'_{lo}(\phi_0)}. \tag{4.10}$$

For the moment, we assume that the acceptances in the upper and lower part of the spectrometer are equal.
For one traget half, using Eq.4.9 and Eq.4.4, 4.5, $A_\perp$ before polarization reversal is:

$$\frac{A_\perp}{d} = - \frac{1}{fdP_\mu|P_t|cos\phi_0} A_{N1}(\phi_0). \tag{4.11}$$

Replacing the events by their weight w, the average of the counting rate asymmetry over the event sample, divided by the term $fd\cos\phi_0$, eq.4.9 takes the form:

$$\left\langle \frac{A_{N1}}{fd\cos\phi_0} \right\rangle = \frac{\sum_{up} \sqrt{w_{up}} - \sum_{lo} \sqrt{w_{lo}}}{\sum_{up} w_{up} + \sum_{lo} w_{lo}}. \tag{4.12}$$

58

The sums run over all events in the upper and the lower part of the spectrometer. Analogous weighted averages can be written down for the counting rate asymmetry A_{N2} after polarization reversal. For small counting rate asymmetries the event yields from the upper and lower spectrometer parts are similar and the statistical error on the asymmetry for weighted events is a gaussian: $\sqrt{\sum_{up} w_{up} + \sum_{lo} w_{lo}}$.

$A_\perp$ is calculated through this method by substituting the expression for $\langle A_{N1}/fd\cos\phi_0\rangle$ in Eq.4.11:

$$\frac{A_\perp}{d} = -\frac{1}{P_\mu |P_t|} \frac{\sum_{up}\sqrt{w_{up}} - \sum_{lo}\sqrt{w_{lo}}}{\sum_{up} w_{up} + \sum_{lo} w_{lo}} \tag{4.13}$$

The final asymmetry for one target cell comes from averaging the calculated through eq.4.13 asymmetries before and after polarization reversal with the angle ϕ_0 in the interval $-\pi/2 \leq \phi_0 \leq \pi/2$ for the upper and respectively the lower part of the spectrometer. In the equation below, the previously omitted contribution from the non-equality of the spectrometer acceptances, is also introduced:

$$\frac{A_\perp}{d} = -\frac{1}{2P_\mu\overline{|P_t|}} \left[\left(\frac{\sum_{up}\sqrt{w_{up}} - \sum_{lo}\sqrt{w_{lo}}}{\sum_{up} w_{up} + \sum_{lo} w_{lo}} \right)^{\Uparrow} - \left(\frac{\sum_{up}\sqrt{w_{up}} - \sum_{lo}\sqrt{w_{lo}}}{\sum_{up} w_{up} + \sum_{lo} w_{lo}} \right)^{\Downarrow} \right] - A_{false}. \tag{4.14}$$

The arrows $\Uparrow$, $\Downarrow$ represent the target spin orientation and $\overline{|P_t|}$ is the average target polarization before and after reversal.

To evaluate the false asymmetry contribution to $A_\perp$ the acceptance factors have to be substituted in a similar way in Eq.4.11. The resulting contribution is:

$$A_{false} = -\frac{1}{2fdP_\mu\overline{|P_t|}\cos\phi_0} \left[\left(\frac{a_{up}(\phi_0) - a_{lo}(\pi - \phi_0)}{a_{up}(\phi_0) + a_{lo}(\pi - \phi_0)} \right)^{\Uparrow} - \left(\frac{a'_{up}(\phi_0) - a'_{lo}(\pi - \phi_0)}{a'_{up}(\phi_0) + a'_{lo}(\pi - \phi_0)} \right)^{\Downarrow} \right] \tag{4.15}$$

In the two trivial cases, when $a_{up} = a_{lo}$ and $a'_{up} = a'_{lo}$ or $a_{up}/a_{lo} = a'_{up}/a'_{lo}$ there is no contribution from A_{false}. In reality however, this is not correct, since the acceptance varies with the time, reflecting the changes in the reconstruction efficiency of the spectrometer equipment. Experimentally measured counting rate asymmetries are of the order of 0.5 %, therefore it is crucial to keep the acceptance ratios constant, such that A_{false} is much smaller than the counting rate asymmetries. This is achieved by carefully monitoring various parameters, like chamber efficiencies, beam intensity, etc. and rejecting data for which they fluctuate significantly from their nominal values. The acceptance differences are ignored in the extraction of $A_\perp$ and contributions from A_{false} are studied and included as a systematic error.

The advantages of the $fd\cos\phi_0$ method of asymmetry extraction is its proper treatment of the variations of f, d and $\cos\phi_0$, since it eliminates the necessity of data binning and hence distortions from taking average values of f, d and $cos\phi_0$ within the bins.

4.4 Different ways of event yields combination

The method of extracting the asymmetry from the event yields, described above, is not unique. The extraction formalism in principle allows for various ways of calculating $A_\perp$ from the combinations of event yields from the two target cells or from the upper and

lower part of the spectrometer.

A method, which uses both target cells is sketched in Fig.4.2. The asymmetry is extracted from the event yields $N_{up}(\phi_0)$ from the upstream target cell and $N'_{up}(\pi + \phi_0)$ from the downstream target cell before polarization reversal and $N_{lo}(\pi + \phi_0)$ and $N'_{lo}(\phi_0)$ after polarization reversal. The problem with this method is the fact, that the spectrometer acceptances for the two target halfs a_{up} and a'_{up} are different, as well as a_{lo} and a'_{lo} and they do not cancel.
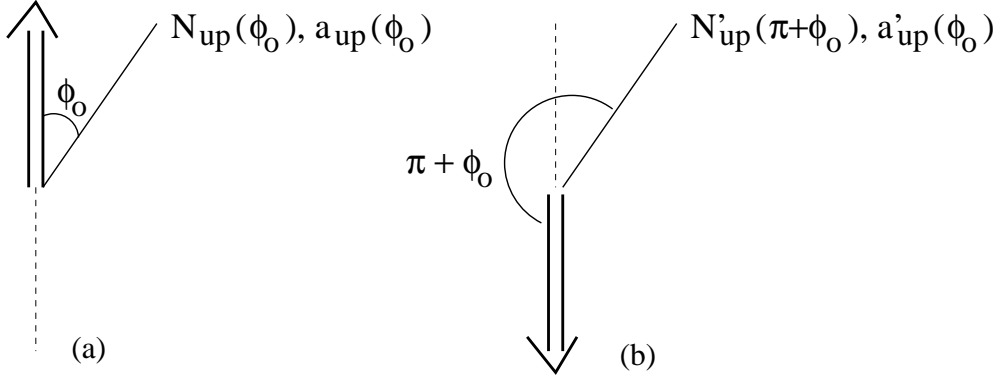

Figure 4.2: *Two targets method of asymmetry evaluation. Event yields and acceptances as a function of the azimuthal angle ϕ before polarization reversal for the upstream target half (a) and downstream target half (b).*

Another way of combining yields is again from one target cell, but from the left and the right part of the spectrometer, as shown in Fig.4.3.
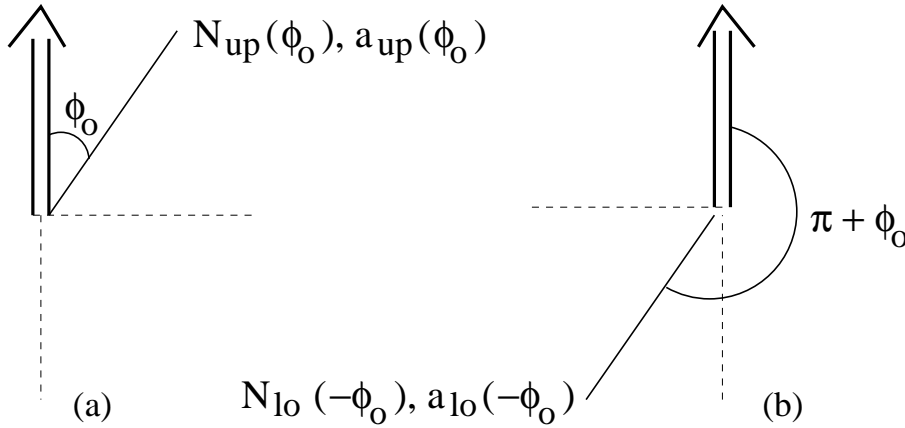
Figure 4.3: *Event yields and acceptances as a function of the azimuthal angle ϕ before polarization reversal for the upper left part (a) and lower right part (b) of the spectrometer.*

The method is equivalent of dividing the azimuthal angle in four intervals instead of two and extracting two asymmetries per target half per polarization orientation. The asymmetries are calculated in the intervals $-\frac{\pi}{2} \le \phi_0 \le 0$ and $0 \le \phi_0 \le \frac{\pi}{2}$, using Eq.4.14.

Chambers in the SMC spectrometer have full up-down and left-right symmetry, which is not the case for the triggers and the bending of the spectrometer magnet. All three physics triggers have up-down, but not left-right symmetry, especially pronounced in Tr.2 and Tr.14 (see Fig.2.8). The spectrometer magnet introduces additional left-right asymmetry. Therefore the event yields from the upper left and lower right or upper right and lower left sections have a difference up to 3 orders of magnitude [70]. Subsequently, the counting rate asymmetries are biased by the geometrical trigger acceptance and it becomes difficult to calculate the spectrometer acceptance ratios and the resulting false asymmetries.

The only method of asymmetry extraction, which has almost equal acceptance in ϕ and $\pi - \phi$ and similar spectrometer and trigger acceptances is described in the previous sections and schematically shown in Fig.4.1. The asymmetry is evaluated for each of the two target cells independently, combining event yields from the upper and lower spectrometer halves before and after polarization reversal. The effect of the small differences in the up/down acceptance cancels if it is constant in time.

4.5 Dilution factor

The target volume contains apart from the polarized nucleons a mixture of other nucleons, which are unpolarized. The dilution factor f takes into account the dilution of the asymmetry due to events, which originate from the unpolarized nucleons. In Eq.4.16 it is defined in terms of the total spin-average cross-sections for the different target nuclei:

$$f = \frac{n_d \overline{\sigma}}{n_d \overline{\sigma} + \sum_A n_A \sigma_A},$$ (4.16)

n is the number of the nuclei and A runs over the non-polarizable elements.
To calculate the dilution factor, the precise target composition has to be known, together with the cross-sections of the different nuclei. A detailed analysis of the materials in the target can be found in [53]. The target consists of deuterated butanol beads with the admixture of chromium(V)-complex and water, the NMR $CuNi$ coils, their teflon C_2F_4 coating and the $^3He/^4He$ cooling mixture surrounding the beads. In addition, due to imperfections in the vertex measurement (vertex uncertainty), some events originate in the target support structure and the microwave system materials and they also contribute to the dilution factor. Table 4.1 lists the relative amounts of all elements present in the polarized deuteron target, normalized to one deuteron nucleon.
This table takes into account the fiducial cuts applied to the data which are chosen to coincide with the dimensions of the target cells in x direction (along the beam) and radially 2 mm inside the target volume. It also accounts for the events which originate from outside the target cells, but are smeared into the regions within the vertex cuts. The choice of vertex cuts and their influence on the dilution factor through vertex uncertainty was studied and is presented in [90].

Nucleus	Nucleons per deuteron
Proton	0.003
Carbon	2.360
Oxygen	0.975
Copper	0.131
Helium-3	0.061
Helium-4	0.255
Sodium	0.010
Chromium	0.023
Fluor	0.080

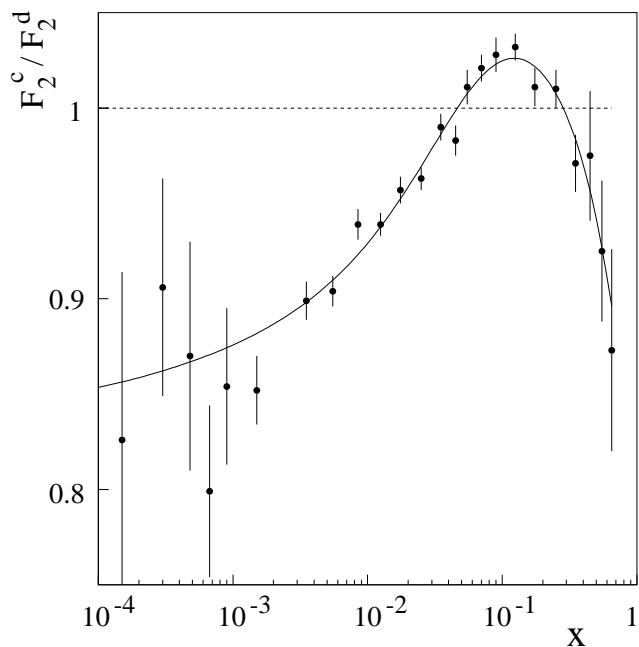Table 4.1: *Unpolarized nucleon content in the traget material, normalized to one deuteron.*

Figure 4.4: F_2^C/F_2^d *structure functions ratio as function of x as measured by NMC. The solid line is a fit to the data.*

If the expression 4.16 is divided by $\overline{\sigma}$ one can use cross-section ratios to calculate f. In case of isoscalar nuclei, the ratio of Born cross-sections per nucleon is equal to the ratio of the structure functions F_2 for the deuteron, apart from a small deviation due to the EMC effect. The F_2^n/F_2^p structure functions ratio as well as the F_2 ratios of various nuclei to deuterium, F_2^A/F_2^d, were measured in several experiments. The most precise results are those of NMC. The results for F_2^n/F_2^p are presented in [94] and for $A = He$, ^6Li, C and Ca in [95,96]. As an example, Fig.4.4 shows the ratio F_2^C/F_2^d, together with the fit to the data, provided by NMC.

The F_2 ratios for nuclei, presented in the target volume, for which no experimental data

exists are obtained using an A-dependent parametrization of the measured ones:

$$\frac{F_2^A}{F_2^d} = C(x) \, A^{\alpha(x)},$$ (4.17)

where the parameters $C(x)$ and $\alpha(x)$ were determined from data published by NMC and SLAC [97].Using this parametrization, the ratio F_2^O/F_2^d was calculated form F_2^C/F_2^d. Similarly, the EMC effect for Cu is extrapolated from the measured ratio F_2^{Ca}/F_2^d.

The cross-section ratios σ_A/σ_d, needed to calculate the dilution factor, are obtained from the structure function ratios using the inverse procedure of the structure functions extraction from the cross-sections:

$$\frac{\sigma_A(x,y)}{\sigma_d(x,y)} = \frac{F_2^A/RC(A,x,y)}{F_2^d/RC(d,x,y)}$$ (4.18)

where $RC(A,x,y)$ are the radiative corrections, obtained using the computer program TERAD [98]. These corrections were calculated over a range of x and y and used to calculate the dilution factor. The resulting f used in the asymmetry calculation is shown in fig.4.5.
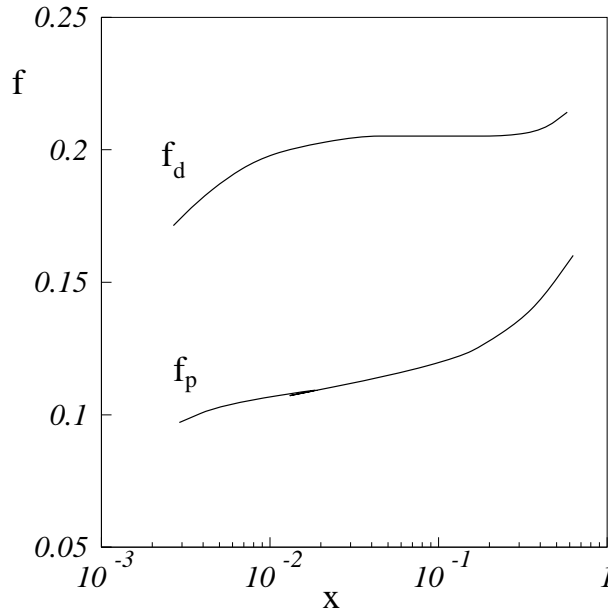
Figure 4.5: *Dilution factor f for proton and deuteron target.*

4.6 Depolarization factor

The depolarization factor d (see eq.4.11), depends on the kinematic variable y, on γ and on the ratio $R = \sigma_L/\sigma_T$. It is defined in equations 1.31 for longitudinally (D) and in equation 1.32 for transversely (d) polarized target nucleons. Fig.4.6 shows the depolarization factors as a function of y at a fixed $Q^2 = 5\text{GeV}^2$.

In the extraction of the asymmetry $A_\perp$ the value of d is calculated for each event, using for R the SLAC parametrization.
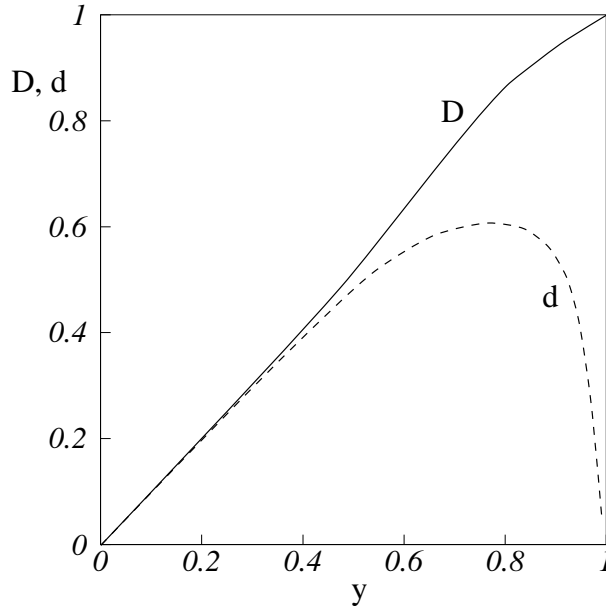

Figure 4.6: *Depolarization factors for longitudinal target polarization (D) and transverse target polarization (d) at $Q^2 = 5\mathrm{GeV}^2$.*

4.7 Parametrization of A_1^d

The A_2^d asymmetry calculation from the results on $A_\perp$ needs as an input the results, obtained on the asymmetry A_1^d. This is provided by an empirical fit to the combined results from SMC on A_1^d and from SLAC E142 on g_1/F_1. Since no Q^2 dependence of the asymmetry is observed in both experiments within the statistical accuracy of the data, it is assumed that A_1 and g_1/F_1 scale and the fit is only x dependent. The kinematics the relation

$$A_1 \approx \frac{A_\parallel}{D(1 + \gamma^2)} \approx \frac{A_1}{1 + \gamma^2} \approx \frac{g_1}{F_1} \qquad (4.19)$$

can be used to justify the direct usage of $\frac{g_1}{F_1}$ for the SLAC data points, since the factor $1 + \gamma^2$ differs from unity by maximum 1.5 %.

The value of A_1^d and a fit to it as a function of x is shown in Fig.4.7. The fit through the SMC points only is compatible with the global fit. The functional form of the fit is

$$A_1 = x^a(1 - e^{-bx}) \qquad (4.20)$$

with parameter values $a = -0.0172 \pm 0.0059$, $b = 0.7721 \pm 0.0527$. The fit probability is $\chi^2/ndf = 1.31$.
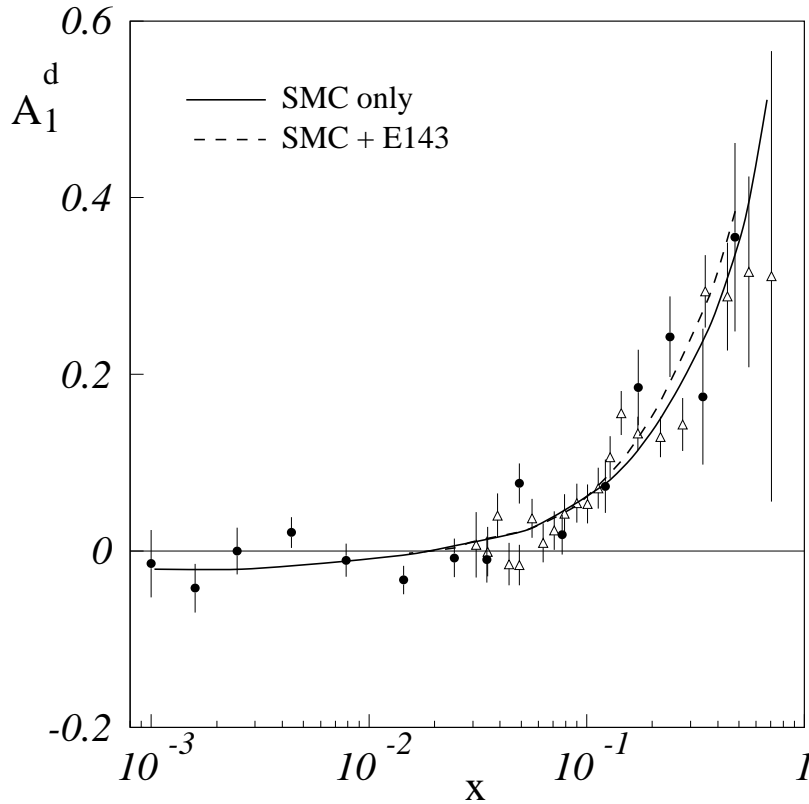
Figure 4.7: *Virtual photon asymmetry A_1^d from SMC (closed circles) and SLAC E143 (open triangles) together with the fit through all data and through SMC points only.*

4.8 Data selection, combination and cuts

The final event sample, which enters in the asymmetry calculation is selected after rigorous tests of its integrity. Initially, the full data sample is produced through the software analysis chain and based on several key distributions data portions wich show abnormal behavior are discarded. The remaining sample is combined in groups and after applying the physics cuts, the asymmetry is extracted. The selection criteria, data combination and physics cuts are described below.

4.8.1 Data selection

The event sample from all triggers after reconstruction and before any cuts contains 4 404 000 events. This represents 80% of the total number of events available on tape, the rest are events from non-physics triggers and trigger 15. The integral period of data taking was separated in six distinct subperiods, defined by the sign of the polarization in the target. In each of the subperiods an almost equal number of events was collected. The data selection is performed on pairs of consecutive subperiods (1+2, 3+4, 5+6) from which the asymmetries are extracted.

The first step in the selection process consists of rejecting bad runs, based on information from the run book, for example when in the first hours of the period the accelerator was unstable, causing fluctuations in the muon intensity. Other straightforward reasons are hardware failures in parts of the spectrometer, detected by the shift crew. Normally, events collected under such conditions exibit after processing an abnormal performance of the apparatus and can also be discarded later.
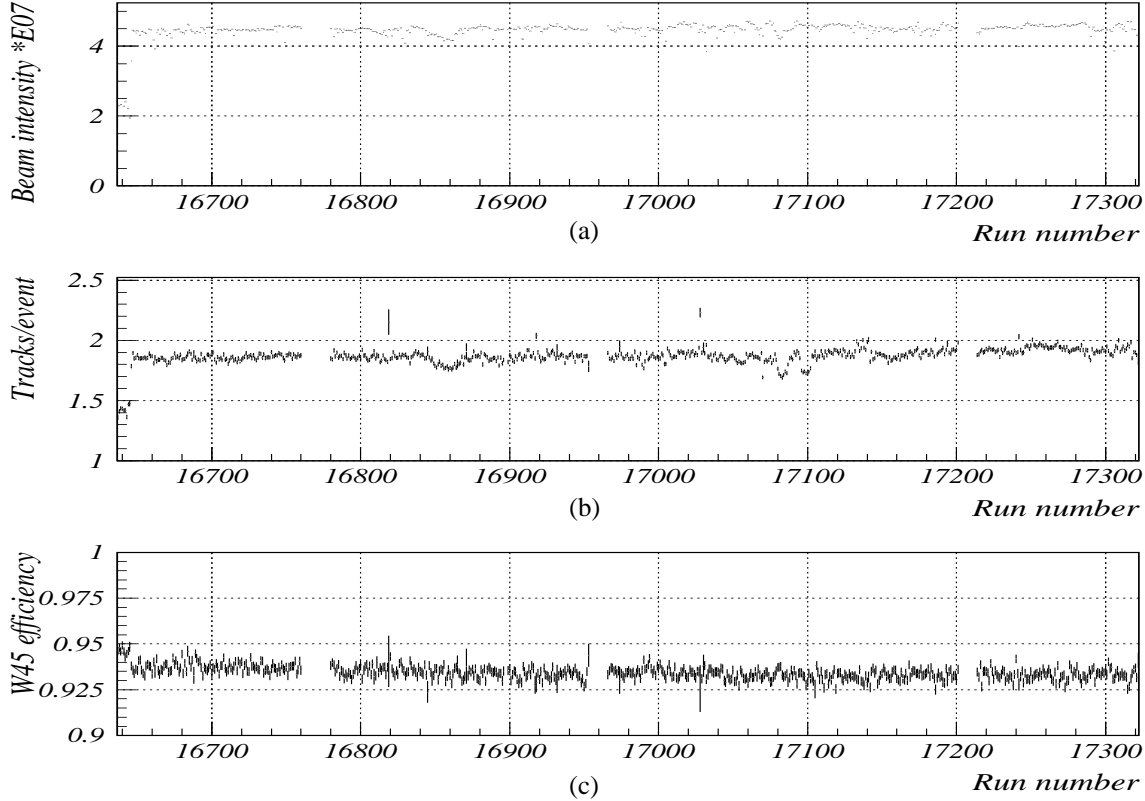
Figure 4.8: *Phoenix run summary plots for period P2E95. (a) Beam intensity, measured by H6 hodoscope, (b) BH track reconstruction efficiency and (c) W45 track reconstruction efficiency.*

The time dependent plots from the reconstruction software summary (Phoenix) represent substantial part of the quantities, on which the data rejection is based. For example:

- Value of the beam intensity and its stability over the data combination period - a variation of about 15% is tolerated.

- Physics triggers reconstruction efficiency - the allowed limits are ±0.5% from the average over the 2 consequtive subperiods.

- Chamber efficiencies stability is evaluated for each individual chamber plane and as a detector group. Different detector groups have different limits on tolerated efficiency variations, but as a general rule, runs with an efficiency variation more than 2% in a given detector are discarded.

66

- Due to specifics of the reconstruction software, the BMS/BH detector group efficiency is particularly succeptible to show efficiency variations stemming from changes in the trigger or the beam. Hence the BMS/BH efficiency is usually an indicator for a problem in another part of the spectrometer.

Fig.4.8 shows distributions of beam intensity, hodoscope (BH) and detector (W45) efficiencies versus run number, which increases monotonically in time, from Phoenix for the entire period P2E95. The gaps in the plots represent periods in which calibration and alignment runs were takes. Certain runs have less events, and therefore less statistical accuracy. All distributions show, that the stability in the period was rather good. The only exception is in the beginning - runs 16637 to 16645 (low beam intensity).

From the total of 625 runs only 18 were rejected, representing a loss of 3% of the data sample.

4.8.2   Data combination

The six subperiods of the period P2E95 are combined in three groups, each containing opposite polarization of the target cells. These groups are used to calculate the asymmetry $A_\perp$ independently for each target cell within one group. Technically, the combination is done using the so called **configuration file**, which contains the list of runs to be evaluated with flags assigning them to the relevant group. This file also contains the mean target polarization for each run, calculated using the parametrization described in section 2.3.3. Schematically, the combination groups are shown in fig.4.9. The arrows represent the orientation of the target cell spins. The approximate number of events in each group before cuts is also shown. Every effort was made that the groups contain balanced number of events in a polarization orientation in order to minimize the additional statistical error due to different number of events. The disbalance in the first group is caused by a problem in the SPS accelerator, resulting in no beam for about half of the time in the subperiod 2. The limited days of data taking imposed strict bounds on the duration of the subperiods between target reversals, therefore the disbalance could not be fully avoided.

Table 4.2 gives an estimation of the additional factor, $\Delta A_\perp$, to the statistical error $\sigma_{A_\perp}$ due to the unequal number of events in each configuration. $\Delta A_\perp$ is zero in a configuration with equal number of events before and after target polarization reversal.

Configuration	Number of events		$\Delta A_\perp [\%]$
1+2	821000	436000	4.8
3+4	722000	972000	1.1
5+6	682000	771000	0.2

Table 4.2: *Additional statistical error $\Delta A_\perp$ in each configuration for period P2E95.*
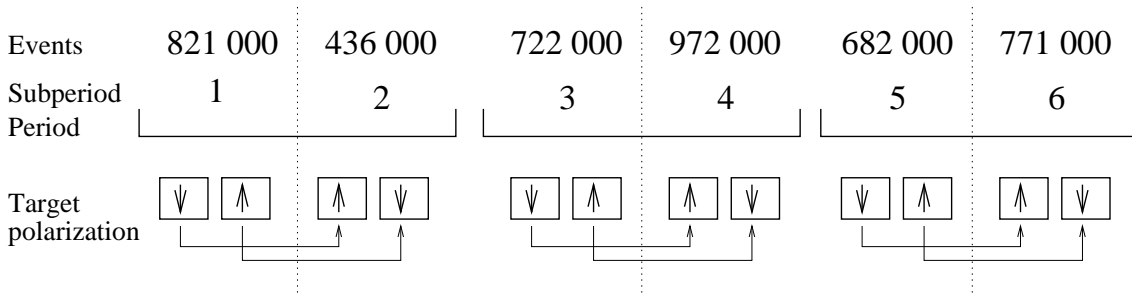
Figure 4.9: *Schematic presentation of the data combination in the six subperiods of period P2E95 into three periods from which the asymmetry is extracted. The number of events before cuts and the target spin orientation is also shown.*

4.8.3 Cuts and binning

The final data manipulation before the asymmetry calculation is the application of a set of cuts defined below and designed to separate the deep inelastic events from the background. The resulting data sample is then divided in x bins in which the asymmetry is calculated.
The cuts applied to the data are:

- Cuts on the vertex: selects events originating in the polarized material from events originating in the target walls, helium coolant, etc. It is choosen such, that it minimizes uncertainties on the dilution factor, caused by vertex uncertainty, weighted against the event loss. In longitudinal direction it coincides with the endcaps of the polarized material holders and has the following values in the SMC coordinate system: **upstream target half** $-5.95m < x < -4.99m$, **downstream target half** $-4.69m < x < -4.09m$. In transverse direction there is a radial cut of $r < 2.3cm$. The vertex distributions in longitudinal and transverse direction, together with applied cuts are shown in fig.4.10.

- Cut on the scattering angle $\Theta > 9mrad$: rejects events with a poor vertex resolution.

- Cut on the energy of the scattered muon $E' > 19$ GeV removes muons originating from hadronic decays of π or K produced in the original muon interaction.

- Cut on the relative energy transfer $y < 0.9$: removes events with large radiative corrections.

- Cut on the energy transfer $\nu > 15$ GeV: limits the relative error on x, which is related to ν as $\Delta x/x = \Delta \nu/\nu$ to $\Delta x/x < 10\%$.

- Cut on the squared four momentum $Q^2 > 0.5$ GeV^2 combined with cut on $x > 0.0015$: defines the perturbative QCD kinematic region of the measurement and also rejects the $\mu - e$ scattering events.

From the 4 404 000 events available for analysis, after cuts 2 822 000 events survive. These events are divided in 5 x-bins in such a way, that the statistical error on the asymmetry A_2 is approximately equal. Table 4.3 lists the x bins together with the events after cuts.
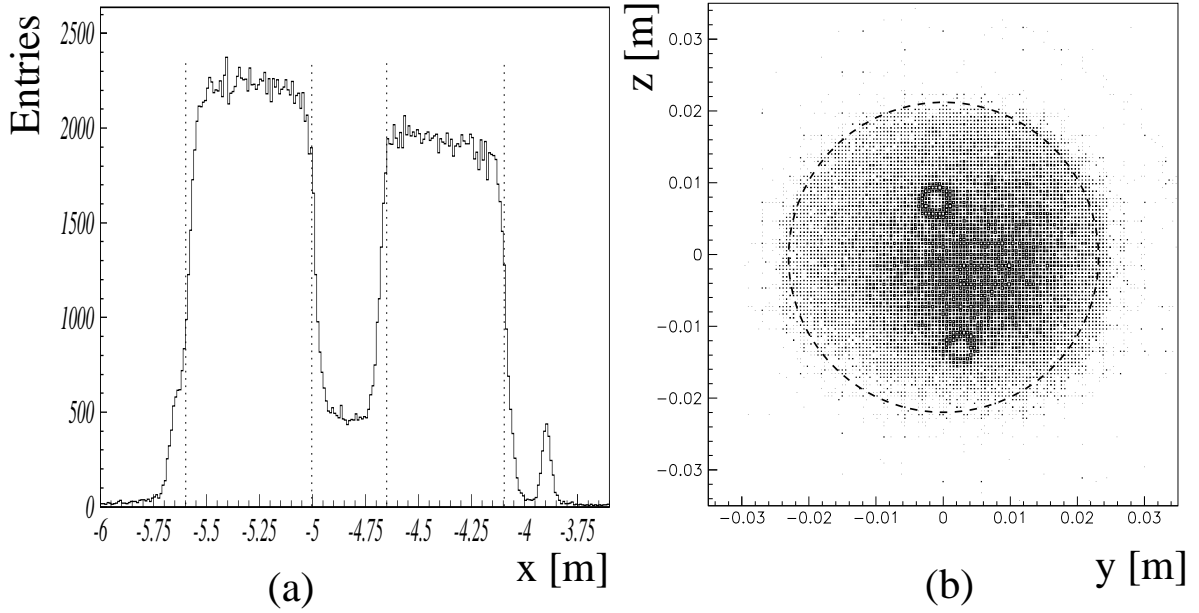
Figure 4.10: *Muon vertex reconstruction in longitudinal direction (a) and transverse direction for a 10 cm slice in x of the downstream target(b). The dotted lines on the plots represent the applied cuts. The two small circles, visible in plot (b) are one of the NMR coils in the target volume. Its presence is taken into account for the dilution factor calculation.*

Number	x bins limits	Number of events
1	0.0015 - 0.005	701 000
2	0.005 - 0.02	682 000
3	0.02 - 0.05	455 000
4	0.05 - 0.12	475 000
5	0.12 - 0.6	509 000

Table 4.3: *List of x-bins used in the A_2 analysis with events in each bin after all cuts applied.*

5 Results on the transverse spin asymmetry

5.1 Introduction

In this chapter the final results on $A_\perp$ for each of the data taking subperiods and for the full sample are presented. The assumptions made in extracting A_2 from $A_\perp$ are discussed and used to calculate the value of A_2^d. Also presented are the sources of systematic errors on the final result for A_2^d.

5.2 The transverse cross-section asymmetry $A_\perp$

The asymmetry $A_\perp/d$ from each of the data taking subperiods is extracted, using the event yield combination through the $fd\cos\phi_0$ method, described in section 4. In total there are six independent measurements of $A_\perp/d$ - three from each polarization configuration and three from the upstream and downstream target cells. Table 5.1 and figure 5.2 show the results on $A_\perp/d$ for each of the measurements with its statistical error in the five $x-bins$, defined in table 4.3. Data cuts and event sample entering the calculation are presented at the end of the previous chapter.

To evaluate the compatibility of the results, a χ^2 test was done of the values of $A_\perp/d$ for each period and independently for the upstream and the downstream target cell. The test shows that all pairs are statistically compatible, and therefore can be combined. A weighted mean of the configurations is then calculated for the target cells and the same compatibility test performed on the remaining combination $A_\perp/d$ *upstream* and $A_\perp/d$ *downstream*. Their combination yields the $A_\perp^d/d$ from all periods, which is then used to calculate the virtual photon-deuteron asymmetry A_2^d.

Table 5.3 lists the results of the combined asymmetries and in graphical form these results are presented in fig.5.4.

conf. / x-bins	$A_\perp$ / d upstream target cell			$A_\perp$ / d downstream target cell		
	↓↑	↓↑	↓↑	↑↓	↑↓	↑↓
1 <.0029>	0.0887 ± 0.1386	0.0930 ± 0.1264	0.0309 ± 0.1231	-0.0188 ± 0.1296	-0.045 ± 0.1157	-0.0918 ± 0.1173
2 <.0108>	-0.0485 ± 0.1235	0.1024 ± 0.1134	-0.1913 ± 0.1102	-0.0850 ± 0.1187	0.0404 ± 0.1069	-0.0021 ± 0.1076
3 <0.0333>	-0.0052 ± 0.1610	0.2501 ± 0.1473	0.2184 ± 0.1429	0.3222 ± 0.1574	-0.0051 ± 0.1435	0.0949 ± 0.1436
4 <.0801>	0.2090 ± 0.2046	0.0411 ± 0.1884	0.1739 ± 0.1821	-0.0339 ± 0.1981	0.1011 ± 0.1799	0.1555 ± 0.1796
5 <.2278>	0.1714 ± 0.2868	0.0275 ± 0.2665	0.0785 ± 0.2578	-0.3212 ± 0.2745	0.0432 ± 0.2483	-0.1810 ± 0.2510

Figure 5.1: *Results for $A_\perp/d$ with statistical errors from the individual subperiods for the upstream and downstream target cells. The numbers in the first column represent the $x - bins$ with their mean value. The arrows are the spin orientation in the target cells.*
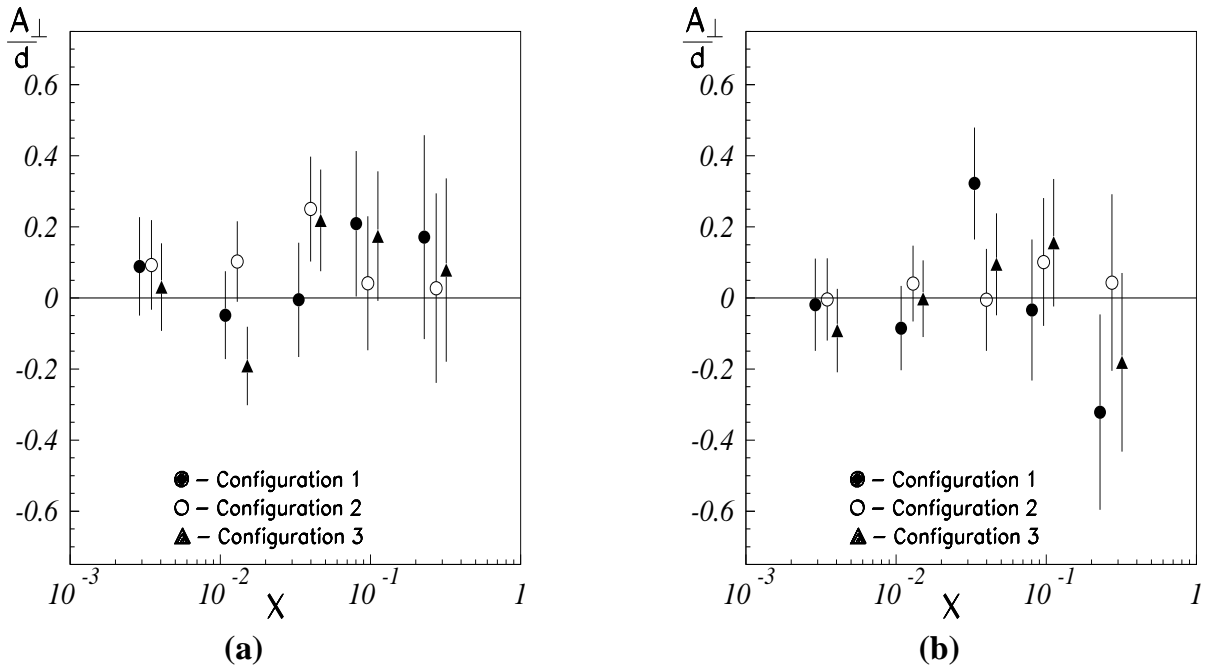

(a)

(b)

Figure 5.2: *Results for $A_\perp/d$ from the individual subperiods for the upstream (a) and the downstream (b) target cells. The different values of $A_\perp/d$ in each x-bin are slightly shifted in x to allow a clear graphical display.*

cell x-bins	$A_\perp / d$		
	upstr.	downstr.	combined
1 <.0029>	0.0691 ± 0.0744	-0.0393 ± 0.0695	0.0112 ± 0.0680
2 <.0108>	-0.0486 ± 0.0666	-0.0109 ± 0.0639	-0.0290 ± 0.0548
3 <0.0333>	0.1648 ± 0.0865	0.1263 ± 0.0853	0.1450 ± 0.0629
4 <.0801>	0.1386 ± 0.1103	0.0810 ± 0.1070	0.1090 ± 0.0829
5 <.2278>	0.0885 ± 0.1556	-0.1418 ± 0.1485	-0.0321 ± 0.1100

Figure 5.3: *Results for $A_\perp/d$ with statistical errors for the upstream, downstream target cells and combined.*
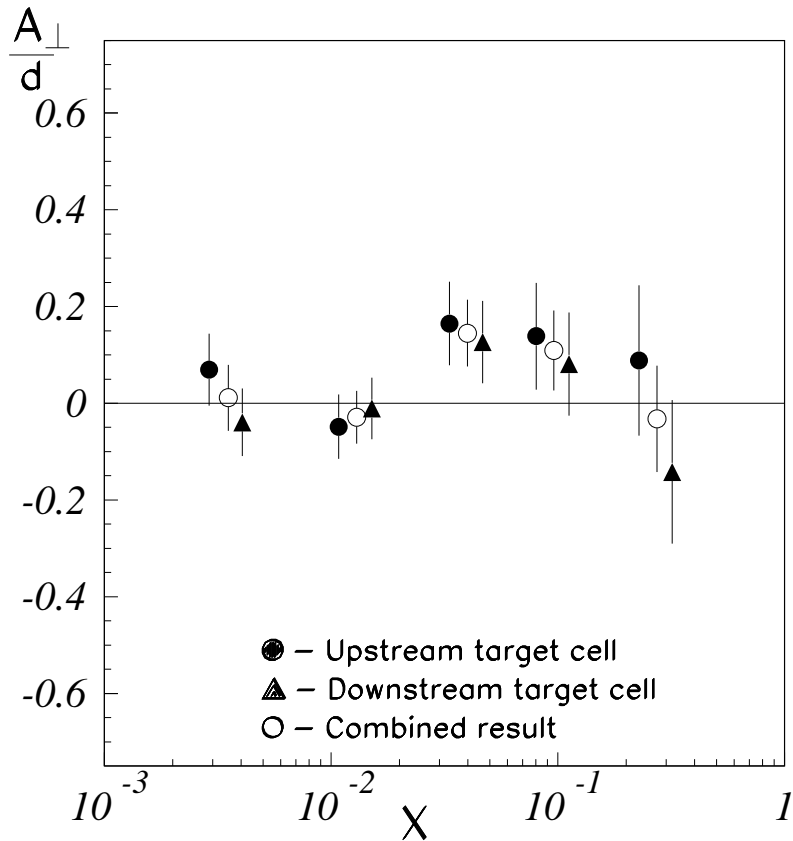

Figure 5.4: *Results for $A_\perp/d$ for the combined periods in the upstream and the downstream target cells and their weighted mean. The points of the weighted mean $A_\perp/d$ is at the mean x of the bins.*

5.3 The virtual photon-deuteron asymmetry A_2^d

Before calculating the asymmetry A_2^d as a function of the scaling variable x only, several assumptions have to be made to eliminate the explicit dependence of A_2 on Q^2 through the factors $\xi\eta$ and the twist-3 contribution from g_2 structure function (see section 1.2.4).

5.3.1 Results on A_2^d

The virtual photon-deuteron asymmetry A_2^d is calculated from the combined results from all three data taking periods. For each x-bin, $A_\perp/d$ is averaged over Q^2. Additional inputs are the parametrization of A_1^d, described in section 4.7 and the mean values of the kinematical factors ξ and η for each x-bin. They are obtained during the calculation of $A_\perp$. Table 5.1 and figure 5.5 show the results on A_2^d with statistical errors as function of x. Also shown are the average values of Q^2 for each x-bin. The influence of the asymmetry A_1 is suppressed by the multiplicative factor ξ (see eq.1.30), which in the kinematical region of SMC is close to zero and therefore the values of A_2^d closely follow those of $A_\perp/d$.
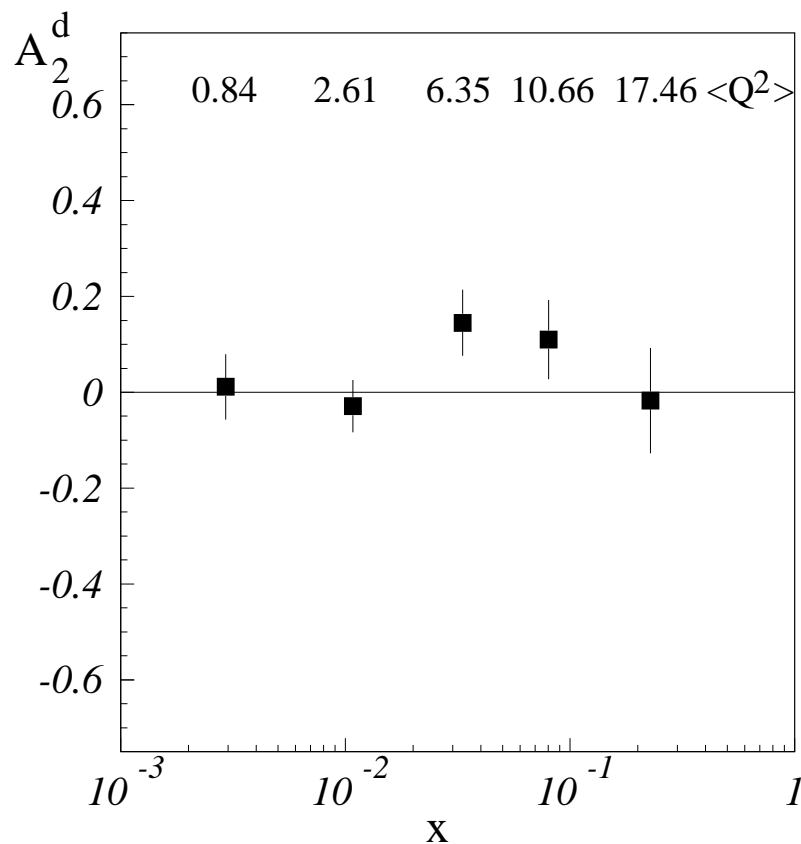

Figure 5.5: *Virtual photon-deuteron asymmetry A_2^d as a function of x. Only statistical errors are shown.*

x bin	$\langle x \rangle$	A_2^d	$\langle Q^2 \rangle$ GeV^2
0.0015 - 0.005	0.0029	0.0112 $\pm$ 0.0680	0.84
0.005 - 0.02	0.0108	-0.0290 $\pm$ 0.0548	2.61
0.02 - 0.05	0.0333	0.1450 $\pm$ 0.0692	6.35
0.05 - 0.12	0.0801	0.1100 $\pm$ 0.0829	10.66
0.12 - 0.6	0.2278	-0.0170 $\pm$ 0.1100	17.46

Table 5.1: *Results on the virtual photon-deuteron asymmetry A_2^d with its statistical error for the 5 x-bins. Listed is the average Q^2 in each x-bin.*

5.3.2 Systematic errors on A_2^d

Following is a discussion on the sources of systematic error on the measurement of A_2^d.

5.3.2a Beam polarization

The sources of errors on the measurement of the muon beam polarization are described in section 2.5 and in the references therein. The value of the statistical and systematic error on the polarization are 3 % and 2 % respectively and in the final number used in this analysis, $P_\mu = -0.78 \pm 0.036$, they are combined in quadrature. The contribution of the uncertainty on the beam polarization measurement to the systematic error on A_2^d is presented in table 5.2.

$\langle x \rangle$	A_2^d	$\sigma_{stat.}$	Δ_{P_b}
0.0029	0.0112	$\pm$ 0.0680	$\pm$ 0.00047
0.0108	-0.0290	$\pm$ 0.0548	$\pm$ 0.00121
0.0333	0.1450	$\pm$ 0.0692	$\pm$ 0.00604
0.0801	0.1100	$\pm$ 0.0829	$\pm$ 0.00458
0.2278	-0.0170	$\pm$ 0.1100	$\pm$ 0.00071

Table 5.2: *Systematic error on A_2^d due to uncertainty in the beam polarization measurement.*

5.3.2b Target polarization

The target polarization error contributes to the systematic uncertainty on A_2 as a multiplicative factor to the asymmetry. It is obtained from the error of the polarization measurement combined with the error on the interpolation, through which the polarization is calculated in the transverse spin mode (see section 2.3.3). In table 5.3, the values of

74

the systematic error on A_2 due to the target polarization measurement uncertainty are presented.

$\langle x \rangle$	A_2^d	$\sigma_{stat.}$	Δ_{P_t}
0.0029	0.0112	$\pm$ 0.0680	$\pm$ 0.00046
0.0108	-0.0290	$\pm$ 0.0548	$\pm$ 0.00122
0.0333	0.1450	$\pm$ 0.0692	$\pm$ 0.00609
0.0801	0.1100	$\pm$ 0.0829	$\pm$ 0.00462
0.2278	-0.0170	$\pm$ 0.1100	$\pm$ 0.00072

Table 5.3: *Systematic error on A_2^d due to uncertainty in the target polarization measurement.*

5.3.2c Radiative corrections

As introduced in section 4.5, to calculate the one photon exchange cross-section, related to the structure functions from the measured scattering cross-sections, a correction taking into account a higher order QED processes has to be applied. The spin-independent radiative corrections are important for the calculation of the dilution factor f, where contributions from scattering from unpolarized material in the target volume are taken into account.

Spin dependent radiative corrections enter in the case of polarized lepton-nucleon scattering. The asymmetry is calculated from the full measured scattering cross-section, which is a combination of the single photon exchange cross-section with other various spin-dependent cross-sections. Simplified formula of the contributions of the different cross-sections to the asymmetry is:

$$A_{1\gamma} = \frac{1}{\beta} A_{measured} - \frac{\sigma_{tail}}{\sigma_{1\gamma}} A_{tail}. \tag{5.1}$$

The subscripts 1γ and *tail* refer to the one photon exchange and radiative tail, which includes inelastic, quasi elastic (scattering on nucleons) and elastic scattering. The coefficient *beta* is $\beta = \frac{\sigma_{1\gamma}}{\sigma_{1\gamma} + \sigma_{tail}}$. It is calciulated on a event by event basis and is included in the dilution factor f. The second term in eq.5.1 which enters as additive correction to the measured asymmetry $A_2/d = A_{measured} - \Delta A$, is calculated using the program POLRAD developed by Shumeiko and collaborators [109]. As an input this program requires a parametrization of the experimental asymmetry. In this analysis, since no reliable parametrization of A_2 exists, the Wilczek-Wandzura model was used to calculate asymmetry A_2^{WW} from g_2^{WW} and that was used as input. The resulting radiative corrections are extremely small: from 0.00001 to maximum 0.0008, a factor 10^{-3} smaller than the observed asymmetry, therefore they were ignored.

To estimate the error on the asymmetry, associated with the radiative corrections, they were recalculated assuming 100 % error on A_2^{WW} and the difference is used as a systematic uncertainty. It is listed in table 5.4.

$\langle x \rangle$	A_2^d	$\sigma_{stat.}$	Δ_{RC}
0.0029	0.0112	± 0.0680	± 0.00009
0.0108	-0.0290	± 0.0548	± 0.00008
0.0333	0.1450	± 0.0692	± 0.00072
0.0801	0.1100	± 0.0829	± 0.00079
0.2278	-0.0170	± 0.1100	± 0.00096

Table 5.4: *Systematic error on A_2^d due to uncertainty in the calculation of the polarized radiative corrections.*

5.3.2d   Uncertainty on R

The structure function R is contained in the depolarization factor d. Its values and the error are obtained from the parametrization R_{1990}. The contributions to the systematic uncertainty on A_2 are calculated, using the error provided by the parametrization and are given in table 5.5.

$\langle x \rangle$	A_2^d	$\sigma_{stat.}$	Δ_R
0.0029	0.0112	± 0.0680	± 0.00016
0.0108	-0.0290	± 0.0548	± 0.00182
0.0333	0.1450	± 0.0692	± 0.00232
0.0801	0.1100	± 0.0829	± 0.00161
0.2278	-0.0170	± 0.1100	± 0.01920

Table 5.5: *Systematic error on A_2^d due to uncertainty on the parametrization R_{1990}.*

5.3.2e   Dilution factor

The error in the calculation of the dilution factor f has contributions from several sources. The main uncertainty is due to the cross-section ratios, for which the errors on the published F_2 ratios were used. The contribution of the different materials in the target volume (mainly the NMR coils) and the amount of $^3He/^4He$ mixture, which was estimated from the packing factor of the target beads, was also taken into account.

An additional error in the calculation of the dilution factor comes from the vertex reconstruction uncertainty. Effects are bigger for small scattering angles, which are correlated with small x and Q^2 values. They were studied with a Monte-Carlo simulation [90], which generates vertices as a function of the amount and density of the material in and around the target cells and smears them assuming Gaussian and Lorentzian distributions. The width of the distribution depends on the error of the vertex fit along the beam axis (x_{SMC}) and on the scattering angle Θ. The simulated vertex distribution is then compared with

the one obtained from the data for the same Θ and iteratively the width of the smearing is adjusted until the best χ^2 of the two distributions is found.

The additional error to f found by this method is 1 % for $\Theta > 20$ $mrad$ up to 3.3 % for $9 < \Theta < 15$ $mrad$.

Taking into account all relevant contributions, the uncertainty in the dilution factor is calculated as function of x for the average Q^2 of the x-bins. The contribution of this uncertainty on the systematic error on A_2 is shown in table 5.6.

$\langle x \rangle$	A_2^d	$\sigma_{stat.}$	Δ_f
0.0029	0.0112	$\pm$ 0.0680	$\pm$ 0.00021
0.0108	-0.0290	$\pm$ 0.0548	$\pm$ 0.00052
0.0333	0.1450	$\pm$ 0.0692	$\pm$ 0.00261
0.0801	0.1100	$\pm$ 0.0829	$\pm$ 0.00220
0.2278	-0.0170	$\pm$ 0.1100	$\pm$ 0.00561

Table 5.6: *Systematic error on A_2^d due to uncertainty on the dilution factor f.*

5.3.2f Empirical fit to A_1^d

The systematic error due to the fit is estimated by using a refitted A_1^d with a variation of the parameters a and b within their errors (see section 4.7) to recalculate A_2^d. The biggest difference of the values on the asymmetry A_2 are used as a systematic uncertainty. They are listed in table 5.7.

$\langle x \rangle$	A_2^d	$\sigma_{stat.}$	$\Delta_{A_1^d}$
0.0029	0.0112	$\pm$ 0.0680	$\pm$ 0.00111
0.0108	-0.0290	$\pm$ 0.0548	$\pm$ 0.00161
0.0333	0.1450	$\pm$ 0.0692	$\pm$ 0.00192
0.0801	0.1100	$\pm$ 0.0829	$\pm$ 0.00121
0.2278	-0.0170	$\pm$ 0.1100	$\pm$ 0.00314

Table 5.7: *Systematic error on A_2^d due to uncertainty on the fit of A_1^d.*

5.3.2g Acceptance variations

Acceptance variations of the spectrometer are generating the false asymmetries term A_{false} (see eq.4.14, which is minimized by maintaining the efficiency of the spectrometer chambers stable over time and thus having the ratio of acceptances $(a_{up}/a_{lo})/(a_{up}^{'}/a_{lo}^{'})$ close to unity. The acceptance ratios and their contribution to the asymmetry calculation are explained in section 4.2.

In the measurement of A_2 the challenge was to have constant spectrometer efficiency over a time period of one data set, from which the asymmetry $A_{\perp}/d$ is calculated, of the order

of 65 hours. To evaluate A_{false}, a method used in the calculation of the false asymmetries for A_1 was taken with certain modifications.

While the main contributing factor to the false asymmetry in the calculation of A_1 are differences in the spectrometer acceptance of the upstream and downstream target cells between target polarization reversals, in the case of A_2 it is between the upper and lower part of the spectrometer for one target cell and within the time interval of the data set. A study of the efficiencies of the different chambers in their upper and lower part was performed on the data available from the μDST's with the program packages, discussed in section 3.4.2. Only data, which is used for asymmetry calculation was considered. The study was done in the following steps:

- Investigation of plane efficiencies ratios $\epsilon_{up}^{plane}/\epsilon_{lo}^{plane}$ for deviations from unity for all detectors in the spectrometer versus time and in three chamber regions - inner, outher and full (see section 3.4.2). Special attention was given to the Z planes, since electronics failure in this coordinate affects the upper or lower part of the plane separately. The data was combined in such a way, that the statistical error on each point was below 1 %. For some planes and regions this condition required efficiencies to be calculated from up to three runs (1.5 hour period of data taking).

- Investigation of detector group (detector groups definitions are given in sections 2.4.4 and 2.4.5) efficiency ratios $\epsilon_{up}^{detector}/\epsilon_{lo}^{detector}$ for group of runs, where the plane efficiency ratios shows deviations form unity. This group is divided in subgroups in an attempt to isolate the time period in which the change of efficiency of a given detector occurs. Subsequently, the runs in which a detector with efficiency different from the nominal one is found are removed from the data sample.

Typical ratios from the studies outlined in the first bullet are shown in fig.5.6 for the plane Z_2 of drift chamber W2 for the upstream target cell and for plane Z_2 of proportional chamber P0D for the downstream target cell, both for the full period of data taking. The plots shows, that the stability of the ratios is very good and does not change over time. Similar results were obtained for all detectors in the spectrometer.

The detector group efficiency ratios were studied in the same way as the plane ratios with efficiencies of one group studied against the other detectors. Since all planes within detector groups have stable efficiencies after applying the cuts determined from the plane efficiency studies, this study was redundant, but nevertheless served as a cross-check of the efficiency evaluating software.
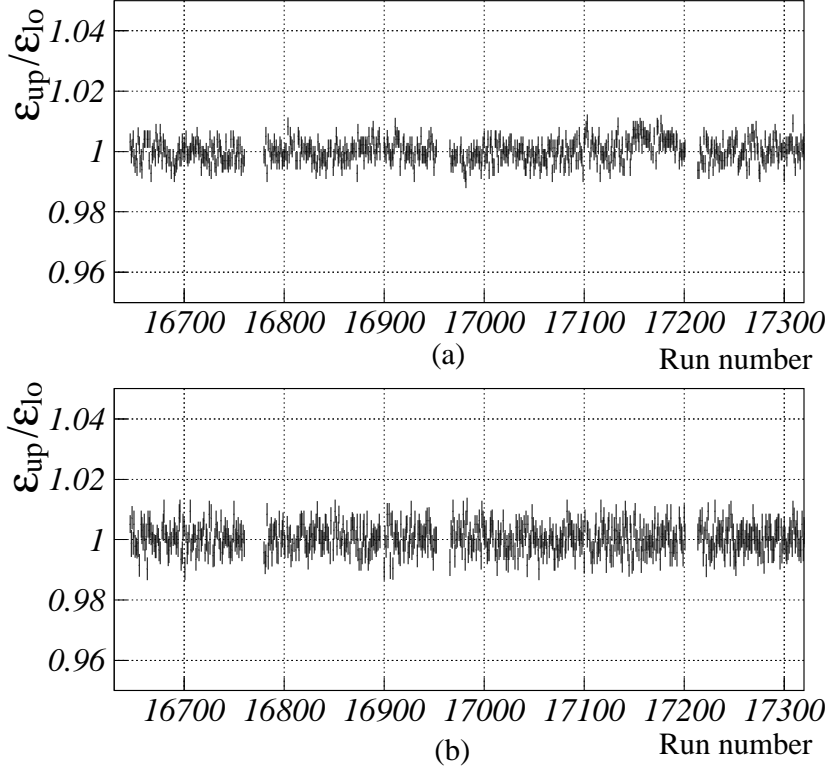
Figure 5.6: *Efficiency ratios $\epsilon_{up}^{plane}/\epsilon_{lo}^{plane}$ for plane Z_2 of W2 (a) and for plane Z_2 of P0D (b) for the full period of data taking P2E95.*

The false asymmetry is calculated with the program FALSIES, which was originally developed for A_{false} studies of the asymmetry A_1. It uses spectrometer data for one target configuration. Variations of the detector efficiencies, which are allowed by the applied cuts within the configuration period are applied to this data sample through a random number generator, which eliminates a hit in a plane of a given detector from the reconstructed track with a probability, determined by the efficiency difference. This difference is obtained through studies of the detector efficiencies before and after polarization reversal for a given data set, used to calculate the physics asymmetry A_1. The track is reevaluated, taking into account the minimum plane requirements of a given detector group and rejected, if these requirements are not met, due to insufficient number of planes with hits. This way, a second set of data which simulates the detector acceptance after polarization reversal is obtained. Both sets combined are used to recalculate the asymmetry. The only parameter changed with this data manipulation is the acceptance of the spectrometer, the polarization of the target is equal and therefore the expected physics asymmetry is zero, therefore the calculated asymmetries are only A_{false}. It is important to note, that the statistical errors in this calculation are smaller, that those of the physics asymmetry since the events are correlated. The error on A_2 is proportional to $\sqrt{\frac{1}{N_{up}+N_{lo}}}$, while due to

the correlations, the error on A_{false} is proportional to $\sqrt{\frac{1}{N_{up}}\left(\frac{N_{up}}{N_{up}^{'}}-1\right)+\frac{1}{N_{lo}}\left(\frac{N_{lo}}{N_{lo}^{'}}-1\right)}$,

where $N_{up}, N_{lo}, N_{up}^{'}$ and $N_{lo}^{'}$ are the event yields in the upper ant the lower part of the

spectrometer for one target cell, before and after the chamber efficiency modification.

To calculate A_{false} for the asymmetry A_2, the program was modified to simulate different efficiencies in the upper and lower part of the spectrometer. To estimate the changes in the efficiencies to be applied, the detector plane efficiency ratios were averaged over time for one target polarization orientation. Figure 5.7 shows the result of the average $\epsilon_{up}^{plane}/\epsilon_{lo}^{plane}$ for the six data groups and for the same detector planes as in fig.5.6.
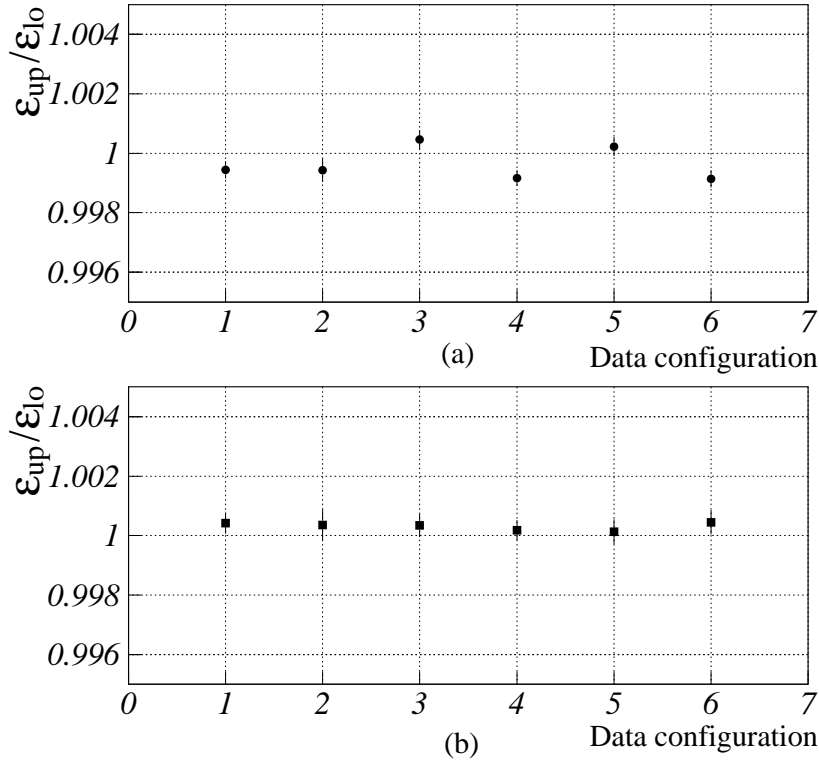

Figure 5.7: *Average efficiency ratios $\epsilon_{up}^{plane}/\epsilon_{lo}^{plane}$ for plane Z_2 of W2 (a) and for plane Z_2 of P0D (b) versus data group.*

From these and similar results for all planes in the spectrometer chambers the maximum deviations of the efficiency ratio from unity for the planes was obtained. For example in plane Z_2 of W2, the maximum difference between periods 3 and 6 is 0.15 % and for plane Z_2 of P0D it is 0.05 % between periods 5 and 6. Then the data set 4, which has the most events was modified in the following way: the maximum differences were applied as lower efficiency to the upper part of the detectors, whereas the lower parts were left intact, thus simulating a change in the acceptance ratio. This set is processed through the software chain, which tests the plane requirements of the detector groups and eventually discards tracks, which have too few hits. The two resulting sets - without modification and with modified ratio is produced through the asymmetry evaluating program. Figure 5.8 shows the principle of data modification and combination.
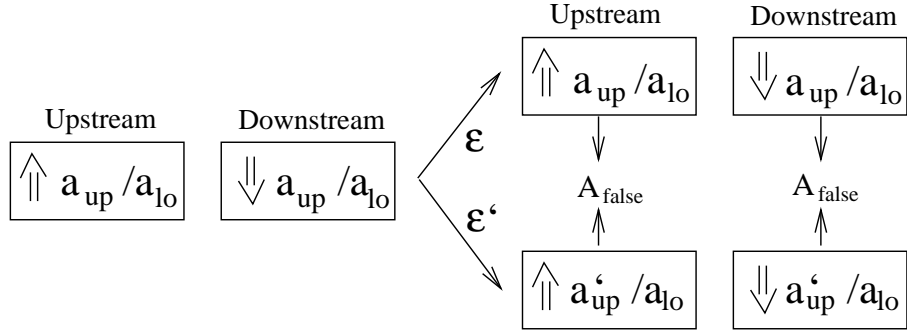
80

Figure 5.8: *Modifications to the acceptance ratio a_{up}/a_{lo} for false asymmetry evaluation in one data set. The acceptance ratios of the upstream and the downstream target cells are not identical.*

The calculated false asymmetries are shown in fig.5.9 for both target cells. As systematic error on the asymmetry A_2 in each x bin the value equal to A_false plus twice its error is taken. The resulting contribution is listed in table 5.8.

$\langle x \rangle$	A_2^d	$\sigma_{stat.}$	$\Delta_{A_{false}}$
0.0029	0.0112	$\pm$ 0.0680	$\pm$ 0.00420
0.0108	-0.0290	$\pm$ 0.0548	$\pm$ 0.00416
0.0333	0.1450	$\pm$ 0.0692	$\pm$ 0.00468
0.0801	0.1100	$\pm$ 0.0829	$\pm$ 0.00509
0.2278	-0.0170	$\pm$ 0.1100	$\pm$ 0.00695

Table 5.8: *Systematic error on A_2^d due to variations of the spectrometer acceptance (A_{false}).*

5.3.2h   Background polarization

This uncertainty takes into account the contamination of the target material with other polarizable nuclei. The degree of deuterization is 99.4 % and the correction to the deuteron asymmetry is calculated, assuming proton polarization twice higher than the deuteron through

$$A_{2,BP}^d = \frac{P_H}{P_d} \frac{n_H}{n_d} \frac{\sigma_H}{\sigma_d} A_{2,WW}^p, \tag{5.2}$$
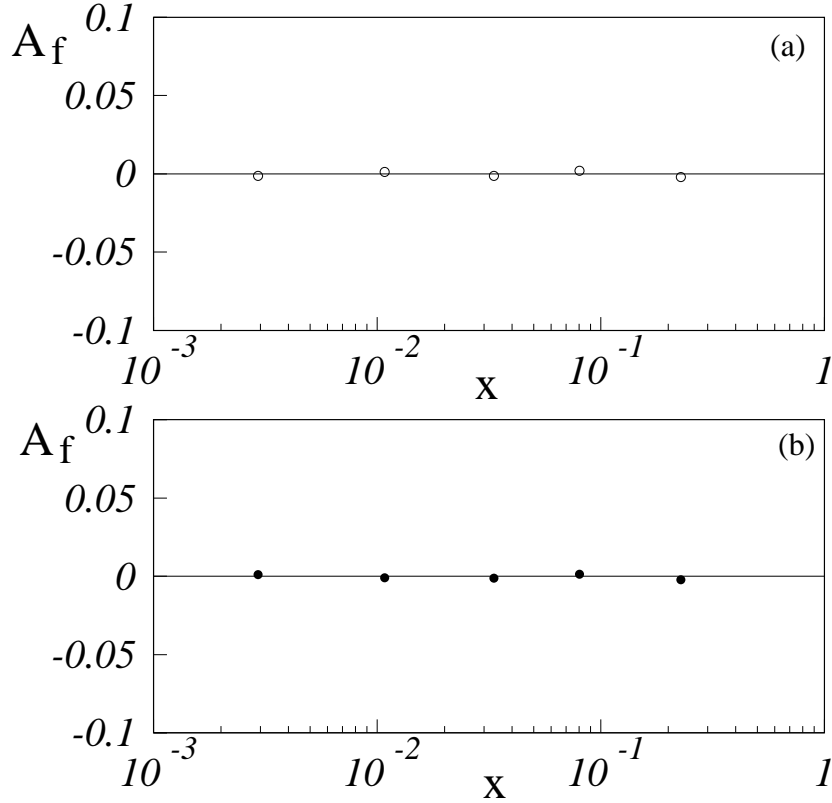
Figure 5.9: *False asymmetry from acceptance variations in the upper and lower part of the spectrometer for the upstream (a) and the downstream (b) target halfs. The vertical scale is chosen such, that the statistical error on the physics asymmetry will stretch between the upper and the lower edge of the scale.*

$\langle x \rangle$	A_2^d	$\sigma_{stat.}$	Δ_{BP}
0.0029	0.0112	± 0.0680	± 0.00011
0.0108	-0.0290	± 0.0548	± 0.00012
0.0333	0.1450	± 0.0692	± 0.00013
0.0801	0.1100	± 0.0829	± 0.00021
0.2278	-0.0170	± 0.1100	± 0.00022

Table 5.9: *Systematic error on A_2^d due to background polarization.*

where the cross-sections ratios are taken from NMC [94] and $A_{2,WW}^p$ are the Wilczek-Wandzura values for A_2^p. Other nuclei (Carbon, Sodium and Chromium) are presented in very small amounts and the biggest correction from is from Carbon which amounts

to additional 0.1 %. The final uncertainty is calculated as multiplicative factor of the relative error $\Delta^d_{2,BP}/A^d_{2,BP}$ to the asymmetry A^d_2 and is listed in table 5.9.

5.3.2i Total systematic error

Figure 5.10 shows the relative contribution of each of the uncertainties to the total systematic error on A^d_2. Combined in quadrature, the errors are given in table 5.10 as function of x and compared to the statistical accuracy of the measurement. In all bins they amount to additional uncertainty to the total error (statistical and systematic errors added in quadrature) from 0.16 % in the lowest x bin to 1.9 % in the highest.
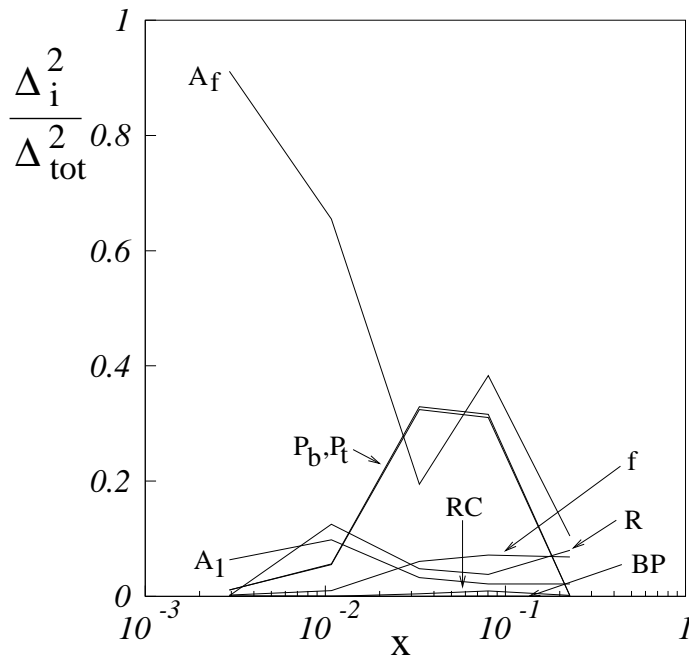

Figure 5.10: *Relative contribution of the sources of systematic error to the total systematic uncertainty in the five x bins of the measurement of A^d_2.*

$\langle x \rangle$	A^d_2	Stat.	Syst.	Total error
0.0029	0.0112	± 0.0680	± 0.00440	± 0.0681
0.0108	-0.0290	± 0.0548	± 0.00514	± 0.0550
0.0333	0.1450	± 0.0692	± 0.01061	± 0.0700
0.0801	0.1100	± 0.0829	± 0.00882	± 0.0834
0.2278	-0.0170	± 0.1100	± 0.02145	± 0.1121

Table 5.10: *Statistical and systematic error of the A^d_2 measurement.*

5.3.3 Comparison of A_2^d to the positivity limit.

To evaluate the positivity bound $|A_2| \leq \sqrt{R}$, a parametrization of the ratio of the longitudinal to transverse virtual photon absorption cross-section $R(x, Q^2)$ is used at the mean values of x and Q^2 of each point. The parametrization R_{1990} was obtained by Withlow *et. al* [101] from measurements of σ_L / σ_T and is widely adopted for calculations, involving R. Figure 5.11 shows the data on A_2^d together with the positivity limit $\sqrt{R}$ calculated using R_{1990}. The errors of the parametrization are not shown. They are below 7% throughout the fitted interval.
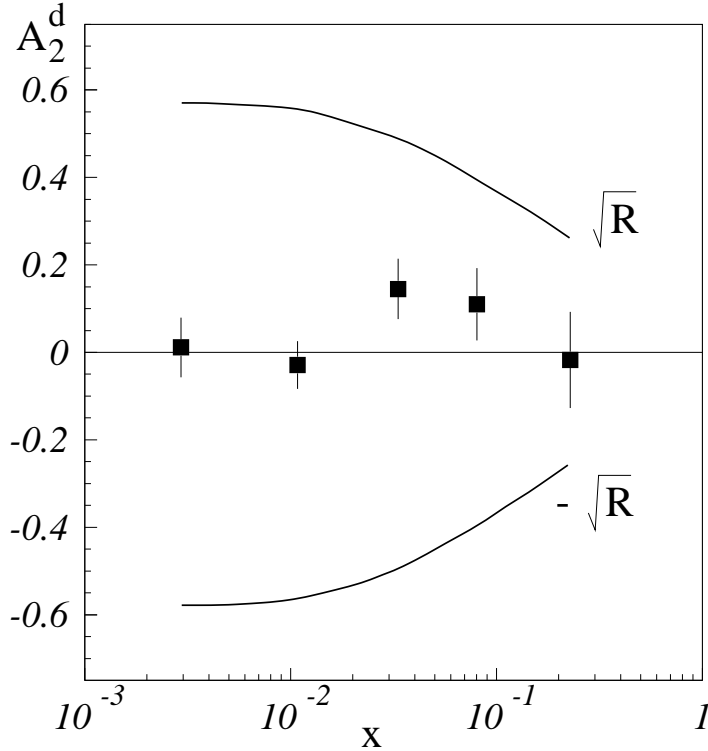

Figure 5.11: *Asymmetry A_2^d (closed points) with positivity limit, evaluated at the Q^2 of the points (solid line). Only the statistical errors for A_2^d are shown.*

All measured values are significantly smaller than the positivity bound, allowing to set a lower limit for A_2^d, which then can be subsequently used to reduce the systematic uncertainty in the calculation of the first moment Γ_1^d of the structure function g_1^d, stemming from the neglect of A_2. This result already fulfills the motivation for the measurement of A_2^d to reduce the systematic uncertainty introduced by using $\sqrt{R}$ as estimate for A_2. One can go further using the published SLAC E143 experiment data on A_2^d. Therefore a more general approach to use the two sets was adopted. The results from SMC and SLAC were combined together to set a limit on A_2^d.

5.3.4 A choice of a scaling quantity

While the asymmetry A_1 is Q^2 independent, A_2 has an explicit Q^2 dependence (see eq.5.3), which cannot be measured with the present data. Using eq.1.28, which relates A_2 to the

experimentally measured cross-section asymmetries $A_\perp$ and $A_\parallel$ and eq.1.33 for the relation of the structure function g_2 to the asymmetries A_1 and A_2, one can write:

$$A_2(x, Q^2) = \frac{2Mx}{\sqrt{Q^2}} \frac{g_1(x, Q^2) + g_2(x, Q^2)}{F_1(x, Q^2)} \tag{5.3}$$

The Q^2 dependence in the denominator of eq.5.3 can be directly taken away by multiplying both sides with $\sqrt{Q^2}$, making $\sqrt{Q^2}A_2$ a scaling quantity.
To eliminate the twist-3 contributions to g_2 one can use the Wandzura-Wilczek model (see sec.1.2.7). Starting from eq.1.51 and using the following equation 1.52, in which the twist-3 term $\overline{g_2}$ is neglected we have:

$$g_2(x, Q^2) = g_2^{WW}(x, Q^2) + \overline{g_2}(x, Q^2) = -g_1(x, Q^2) + \int_x^1 g_1(t, Q^2) \frac{dt}{t} + \overline{g_2}(x, Q^2) \tag{5.4}$$

Then the last term in eq.5.3 can be written as:

$$\frac{g_1(x, Q^2) + g_2(x, Q^2)}{F_1(x, Q^2)} = \frac{\int_x^1 g_1(t, Q^2) \frac{dt}{t}}{F_1(x, Q^2} + \frac{\overline{g_2}(x, Q^2)}{F_1(x, Q^2)} \tag{5.5}$$

The first term is proportional to $\frac{g_1}{F_1} \approx \frac{A_\parallel}{D}$, for which no Q^2 dependence has been observed within the statistical accuracy of the available data. Figure 5.12 shows the most recent compilation of the data from CERN SMC [99] and SLAC E143 [100] experiments on the asymmetry A_1^d versus x for different Q^2. Furthermore, if we assume that the second term in eq.5.5 does not introduce Q^2 dependence, we can use $\sqrt{Q^2}A_2(x)$ as a scaling quantity and calculate A_2^d from $A_\perp/d$ averaging over Q^2 in each x-bin.
While the assumption of Q^2 independence of g_1/F_1 is substantiated with experimental data and theoretical predictions [103], the hypothesis of $\overline{g_2}/F_1$ being also Q^2 independent is motivated purely within the scope of the present work, taking into account the statistical precision of the measurement. The Q^2 evolution of the twist-3 part $\overline{g_2}$ is model-dependent (BAG model [41], QCD calculations [38]) and the expected effects are of different magnitude.
Using $\sqrt{Q^2}/A_2$ as a scaling quantity allows for comparison and combination of sets of data, taken at different average Q^2. This will be later applied when a comparison of SLAC and SMC data on A_2 is made.
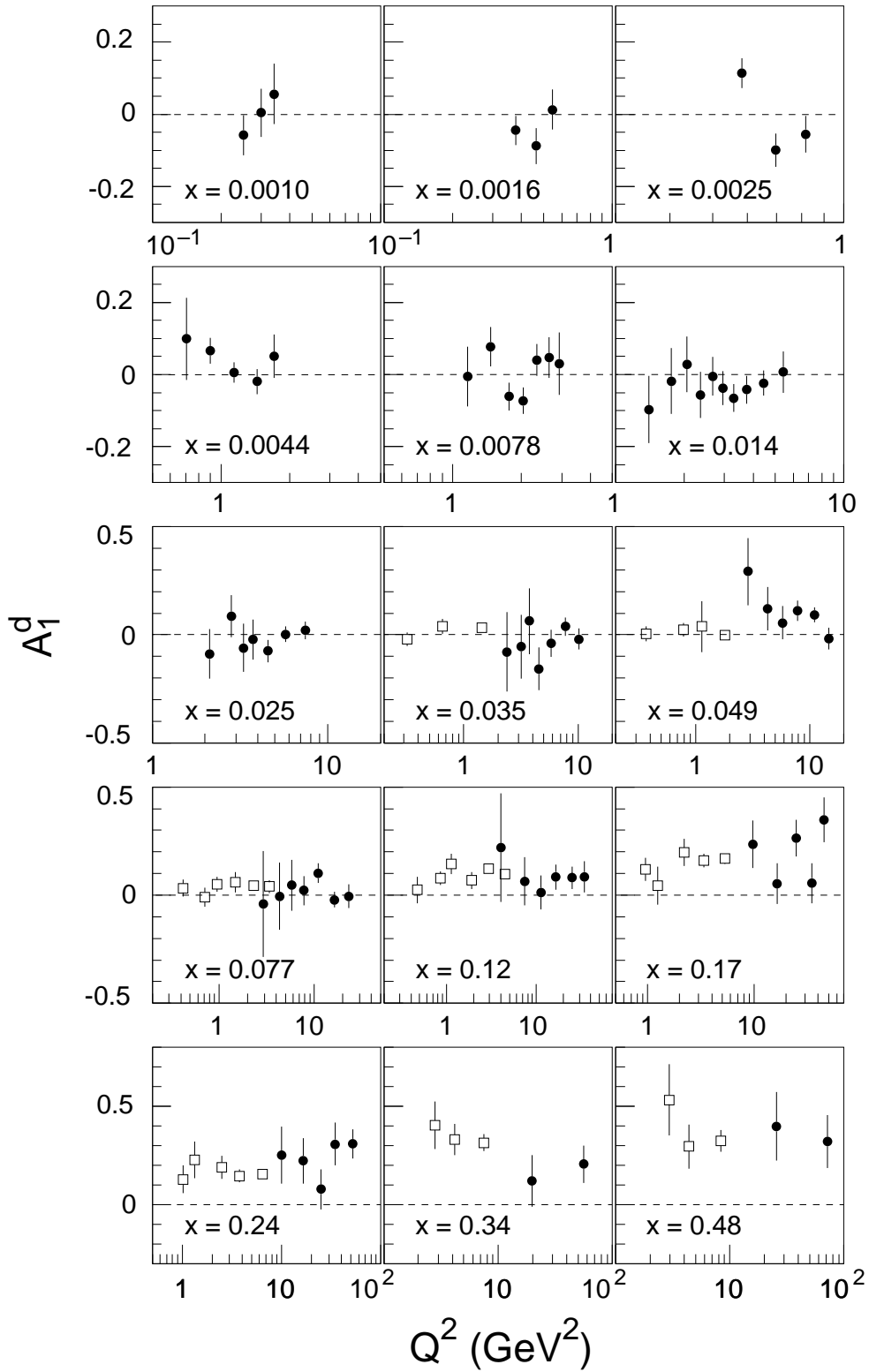
Figure 5.12: *Virtual photon-deuteron asymmetry A_1^d as a function of x and Q^2 from SMC (closed circles) and SLAC E143 (open squares). Only statistical errors are shown.*

5.3.5 Comparison and combination of SMC and SLAC data on A_2^d.

A_2^d was also measured by the SLAC E143 collaboration [102]. The measurement was done by scattering longitudinally polarized electron beam ($E_{beam} = 29$ GeV) off transversely polarized deuterated amonnia target. While it has superior statistical precision, compared to the SMC measurement, it is performed in a more limited x-range ($0.03 < x < 0.8$) and has different average Q^2 in the x-bins ($1.3 < Q^2 < 10$ GeV^2). Figure 5.13 shows a comparison of the SMC and SLAC E143 acceptance in $x - Q^2$ plane after kinematical cuts applied.
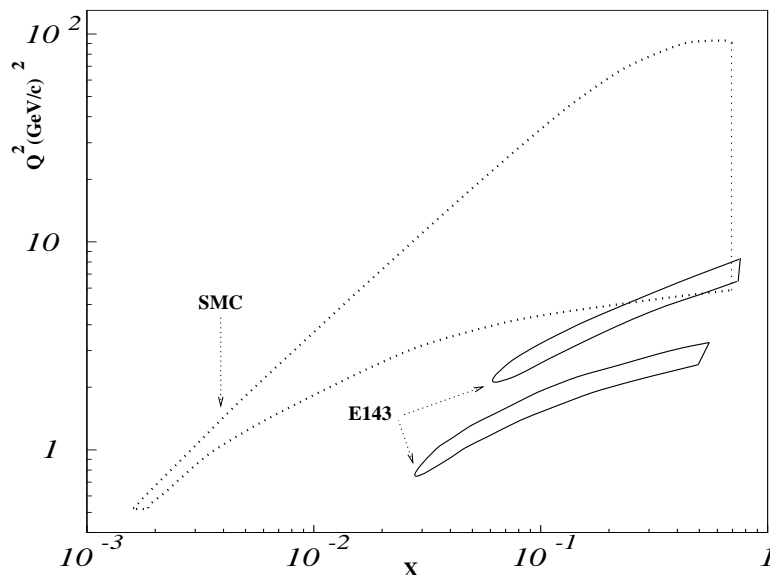

Figure 5.13: *Kinematical limits of SMC and SLAC E143 experiments after cuts. The two bands of SLAC represent the kinematical coverage of the two spectrometer arms: 4.5° - lower band, 7° - upper band.*

The SMC and SLAC data are shown in fig.5.14 and the SLAC data points are listed in tables 5.11 for the 7° spectrometer and 5.12 for the 4.5° spectrometer.

x bin	$\langle x \rangle$	A_2^d	$\langle Q^2 \rangle$ GeV^2
0.075 - 0.120	0.100	$0.0250 \pm 0.046 \pm 0.010$	3.76
0.120 - 0.193	0.154	$-0.007 \pm 0.036 \pm 0.011$	4.97
0.193 - 0.310	0.242	$-0.042 \pm 0.043 \pm 0.015$	6.36
0.310 - 0.498	0.382	$-0.002 \pm 0.073 \pm 0.014$	7.75
0.498 - 0.799	0.584	$0.2170 \pm 0.183 \pm 0.028$	8.84

Table 5.11: *Results on the virtual photon-deuteron asymmetry A_2^d for the 7° spectrometer arm of SLAC E143 experiment with statistical and systematic errors and average Q^2 of the bins.*

x bin	$\langle x \rangle$	A_2^d	$\langle Q^2 \rangle$ GeV^2
0.029 - 0.047	0.038	$0.070 \pm 0.045 \pm 0.008$	1.49
0.047 - 0.075	0.060	$-0.025 \pm 0.028 \pm 0.006$	2.01
0.075 - 0.120	0.095	$0.007 \pm 0.032 \pm 0.010$	2.60
0.120 - 0.193	0.152	$0.004 \pm 0.045 \pm 0.015$	3.21
0.193 - 0.310	0.242	$0.079 \pm 0.072 \pm 0.019$	3.77
0.310 - 0.498	0.379	$-0.077 \pm 0.145 \pm 0.017$	4.22
0.498 - 0.799	0.594	$0.344 \pm 0.390 \pm 0.044$	4.55

Table 5.12: *Results on the virtual photon-deuteron asymmetry A_2^d for the 4.5° spectrometer arm of SLAC E143 experiment with statistical and systematic errors and average Q^2 of the bins.*
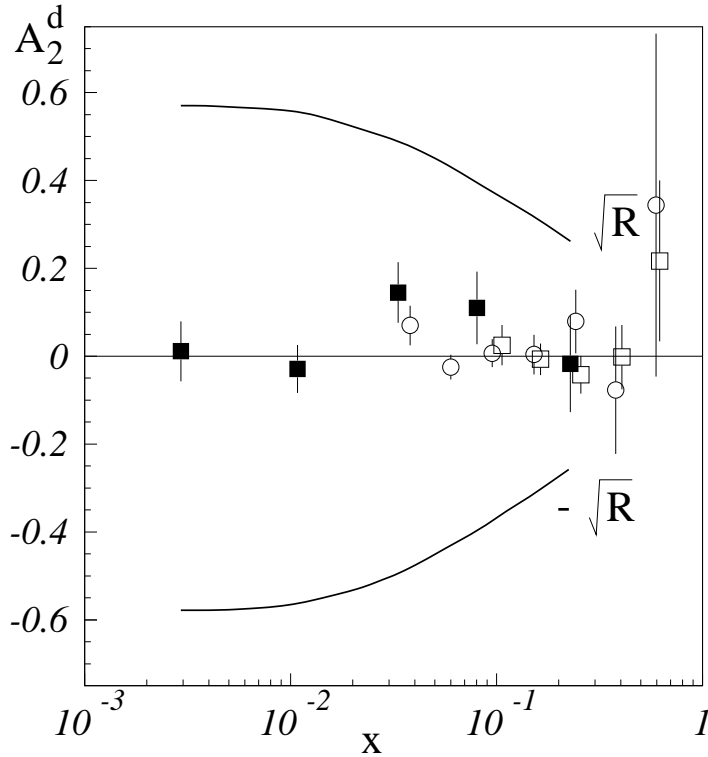

Figure 5.14: *Asymmetry A_2^d from SMC (closed rectangles) and SLAC E143 (open circles - 4.5° spectrometer and open rectangles - 7° spectrometer) at the average Q^2 of the corresponding x-bins. The solid line represents the positivity limit calculated at Q^2 of the SMC points. All data are with statistical errors only.*

Since A_2^d has Q^2 dependence, a more appropriate combination of the sets can be made, using the hypothesis, that $\sqrt{Q^2}A_2$ is independent of Q^2. This assumption also allows for

rescaling of A_2 to a common Q^2, which is suitable for the subsequent use in the error estimation of Γ_1^d, which is commonly presented at a fixed Q^2. Fig.5.15 shows the SMC and SLAC E143 points scaled to $Q^2 = 5$ GeV^2 through $\sqrt{Q^2}A_2(Q^2) = \sqrt{5 \text{ GeV}^2}A_2(5 \text{ GeV}^2)$.
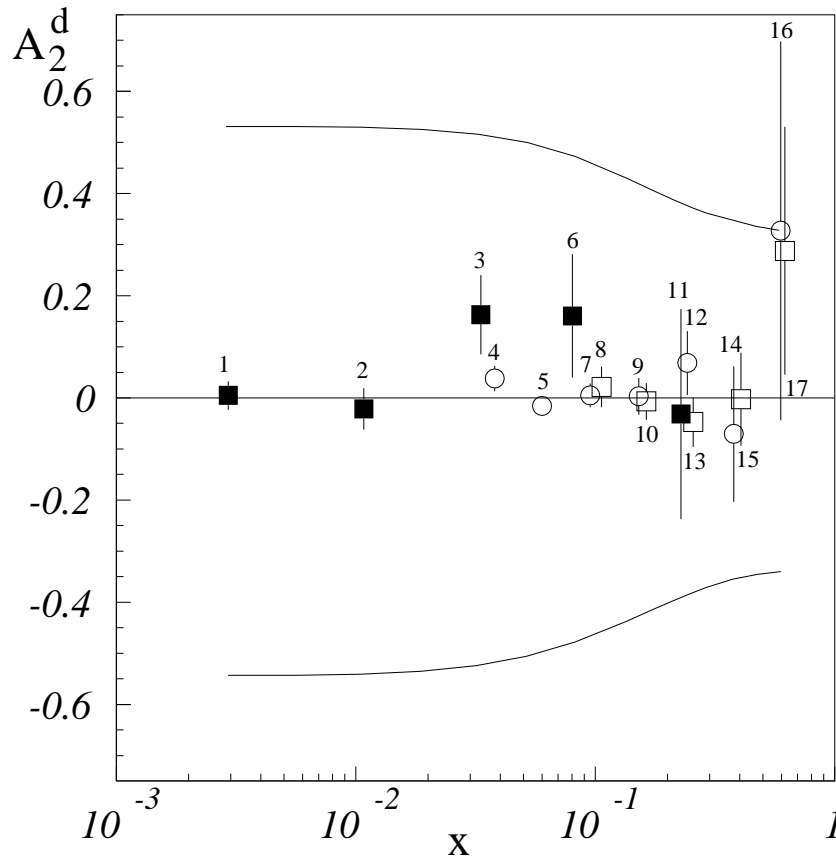

Figure 5.15: *Asymmetry A_2^d from SMC (closed rectangles) and SLAC E143 (open circles - 4.5° spectrometer and open rectangles - 7° spectrometer) scaled to a common $Q^2 = 5$ GeV^2. The solid line is the positivity limit calculated at the same Q^2. All data are with statistical errors only. The numbers above the points show the bin combination - see Fig.5.16.*

The results from both experiments are compatible within errors in the overlapping x-region and consistent with zero. There is no violation of the positivity limit and all data below $x = 0.5$ are much lower than $\sqrt{R}$. A fit with the hypothesis $A_2 = 0$ to all points yields $\chi^2 = 18.42$ for 16 degrees of freedom, which gives the fit probability better than 34%.

The rescaled points can be combined together by making a weighted average. The result of such average is shown in fig.5.16. Only statistical errors are used. The solid line on the plot shows a new limit on A_2^d calculated from the absolute value of the asymmetry with a 95 % confidence level.

In the whole covered interval $0.0015 < x < 0.7$ the value of A_2^d is below 0.1, 19% of the $\sqrt{R}$ in the low x region and 28% of $\sqrt{R}$ for $x > 0.4$.
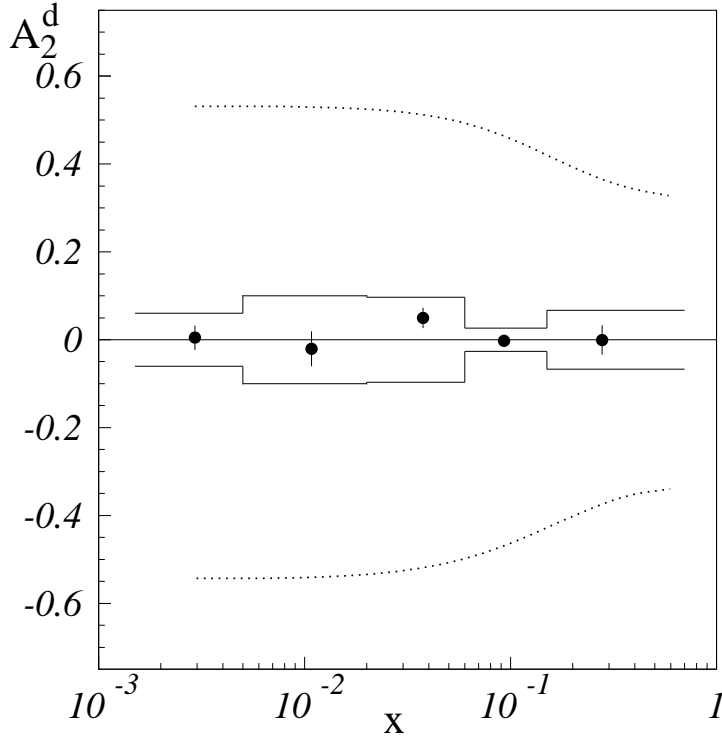
Figure 5.16: *Combined asymmetry A_2^d form SMC and SLAC E143 experiments at $Q^2 = 5$ GeV^2. The solid line is a limit of A_2 from the data points with 95 % confidence level. The dotted line is the positivity limit. The following bins from fig.5.10 are combined in this plot: bin 1 - bin 1; bin 2 - bin 2; bin 3 - bins 3 and 4; bin 4 - bins 5 to 10; bin 6 - bins 11 to 15.*

5.3.6 Impact of the results on the evaluation of Γ_1.

As outlined in section 1.2.4 the spin-dependent structure function g_1 has the following relation to the virtual photon-nucleon asymmetries:

$$g_1 = \frac{F_1}{1+\gamma^2}(A_1 + \gamma A_2)$$

and in its calculation the approximation $g_1 \approx \frac{F_1}{1+\gamma^2}(A_{\parallel}/D)$ is used, justified by the suppression of A_2 by the small factor γ. Subsequently this neglect is taken into account by including it as a systematic errors on the first moment $\Gamma_1 = \int g_1(x)\mathrm{dx}$.

The experimental results on A_2^d [99] allow for a considerable reduction of the systematic error on Γ_1^d due to the neglect of A_2. From the limit set by the SMC results on A_2^d alone, the error becomes 0.0011 and the combined SMC and SLAC data brings it down to 0.0005. The latest number is a factor 8 reduction over the estimate stemming from using the positivity constraint $|A_2| \leq \sqrt{R}$.

In the first SMC publication on g_1^d [104] the calculation of the systematic uncertainty due the neglect of A_2^d was done through the only available source at the time - the positivity

90

condition $|A_2| \le \sqrt{R}$. The value of the error is 0.0041, wich is the second biggest source of uncertainty behind the error from the spectrometer acceptance variations 0.0130. The acceptance variation error at the time of this publication was overestimated and in subsequent analyses it was reduced by a factor of 10, thus enhancing the error due to the neglect of A_2, which became the biggest source of systematic uncertainty. The total systematic error, without the neglect of A_2 is 0.0142 and the contribution of the A_2 is additional 8 %. The SMC measurement of A_2^p in 1994 [105] showed asymmetries compatible with zero and also much lower than the positivity bound $\sqrt{R}$. Using a limit set by this analysis, the error on Γ_1^p form the neglect of A_2^p was reduced from 0.017 [106] to 0.004 [107].

The result on A_2^p can also be used in the measurement on the deuteron structure function g_1^d [108], applying as a limit the available data on A_2^p and assuming $|A_2^n| \le \sqrt{R}$ through the following relation:

$$|A_2^d| \le (1 - 1.5\omega_D)\frac{A_2^p + \frac{F_2^n}{F_2^p}\sqrt{R}}{1 + \frac{F_2^n}{F_2^p}} \tag{5.6}$$

This leads to a reduction of the error on Γ_1^d due to the neglect of A_2 to 0.0025, still the biggest single source of systematic uncertainty, with the errors from all other sources being 0.0058.

Table 5.13 shows the evolution of the error on Γ_1 due to the neglect of A_2 in all publications of the SMC with the estimate of the error evaluated from the available limits at the time of the publication.

Year	Measurement	Error due to A_2	Total syst.error	Estimate coming from
1993 [104]	d	0.0041	0.0200	$|A_2| \le \sqrt{R}$ (deuteron)
1994 [106]	p	0.0017	0.0114	$|A_2| \le \sqrt{R}$ (proton)
1995 [108]	d	0.0025	0.0063	eq.5.6 (A_2^p measured)
1996 [107]	p	0.0004	0.0088	measurement of A_2^p
1997 [99]	d	0.0005	0.0037	measurement of A_2^d

Table 5.13: *Evolution of the systematic error on Γ_1 due to the neglect of A_2 in various measurements of the SMC.*

Table 5.14 lists the contributions of systematic errors to the integral $\Gamma_1^d = \int_0^1 g_1(x, Q_o^2)\mathrm{d}x$ for the SMC experiment at $Q_o^2 = 10$ GeV^2. Explanation of the derivation of the different items in the table can be found in sources [53], [71] and [91]. The error from the neglect of A_2^d to the value of the total uncertainty is the smallest source: $\Delta_{A_2}^2/\Delta_{tot}^2 = 0.018$.

Error source	$\Delta \Gamma_1^d$
Beam polarization	0.0015
Acceptance variation	0.0014
Momentum calibration	0.0014
Target polarization	0.0013
Uncertainty on F_2	0.0012
Kinematic resolution	0.0010
Extrapolation at low x	0.0009
Extrapolation at high x	0.0009
Radiative corrections	0.0008
Dilution factor	0.0006
Proton background	0.0006
Neglect of A_2	0.0005
Total systematic error	0.0037

Table 5.14: *Systematic errors on* Γ_1^d *at* $Q_o^2 = 10$ GeV^2.

5.4 The structure function g_2.

5.4.1 Evaluation of the structure function.

Evaluation of the structure function g_2 is made through the asymmetries A_2 and A_1 using:

$$g_2 = \frac{F_1}{2Mx} \left(\sqrt{Q^2} A_2 \left(1 - \frac{\gamma(\gamma - \eta)}{1 + \gamma^2} \right) - \frac{A_\parallel}{D} \left(\frac{2Mx}{1 + \gamma^2} \right) \right). \tag{5.7}$$

This relation is obtained using eq.1.33 and the scaling quantity $\sqrt{Q^2} A_2$ and $A_\parallel/D$. The unpolarized structure function F_1 is calculated through eq.1.14, from the available NMC parametrization [19].

The calculated values of g_2^d are given in table 5.15 and in fig.5.17.

$\langle x \rangle$	g_2^d	Stat.
0.0029	61.90	$\pm$ 375.00
0.0108	-29.00	$\pm$ 54.90
0.0333	28.10	$\pm$ 13.30
0.0801	4.60	$\pm$ 3.65
0.2278	-0.18	$\pm$ 0.59

Table 5.15: *The structure function g_2^d, calculated at the mean Q^2 of the x bins.*

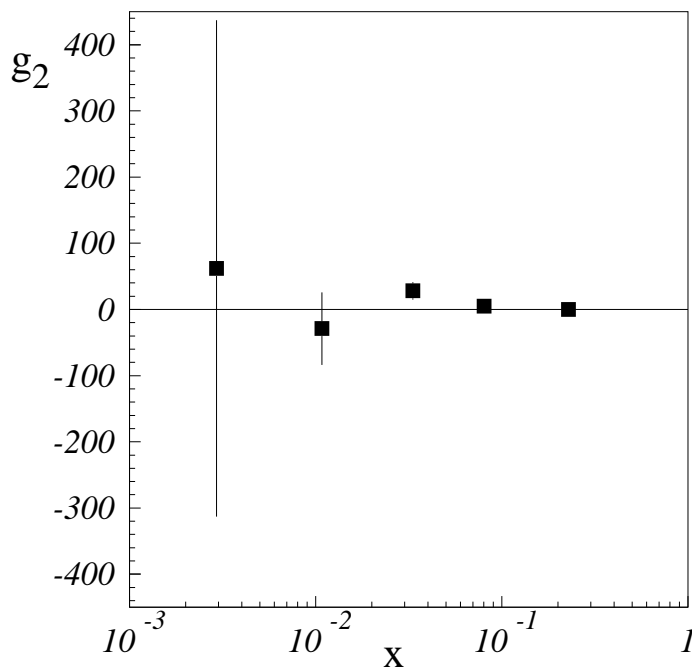Throughout the measured interval, g_2 is compatible with zero.

Figure 5.17: *Structure function g_2^d at the mean Q^2 of the x bins. Only statistical errors are shown.*

5.4.2 Comparison of the results on g_2 to theoretical models

The discussed in section 1.2.7 Wandzura-Wilczek relation predicts the values of g_2 when the twist-3 components are neglected. In this case, g_2^{WW} is determined by g_1 and gives the expectation values for the twist-2 components of g_2:

$$g_2^{WW}(x, Q^2) = -g_1(x, Q^2) + \int_x^1 g_1(t, Q^2)\frac{dt}{t} \tag{5.8}$$

To compare the structure function g_2 with the predicted values for g_2^{WW} it is more instructive to work with xg_2 and xg_2^{WW} respectively. Figure 5.18 shows the two structure functions. g_2^{WW} is calculated from all available data on g_1. The result does not permit to make significant comparison to the model for the magnitude of possible twist-3 contributions to g_2. In order to be able to test the Wilczek-Wandzura model, the statistical sample has to be equivalent to the one used to obtain the structure function g_1 - a factor 15 increase over the available statistics.
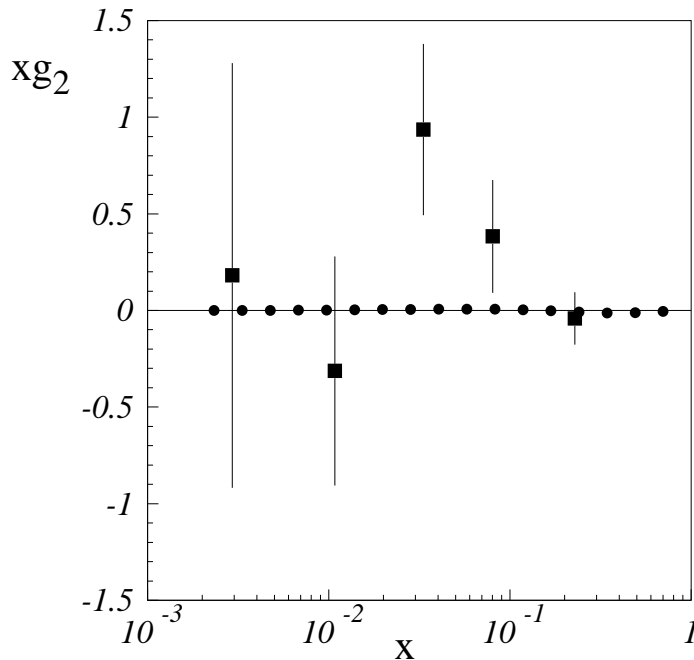

Figure 5.18: *Structure function xg_2^d (closed squares) and twist-2 contribution from xg_2^{WW} (closed circles).*

The Burkhard-Cotthingam sum rule predicts, that the first moment of g_2 vanishes:

$$\Gamma_2(Q^2) = \int_0^1 dx\ g_2(x, Q^2) = 0. \tag{5.9}$$

The value of Γ_2 for the measured x interval is:

$$\int_{0.0015}^{0.6} dx\ g_2(x, Q^2 = 5\ \mathrm{GeV}^2) = 1.05 \pm 1.64. \tag{5.10}$$

While the result is compatible with the theoretical prediction, in order to test the sum rule the unmeasured x-regions of g_2 have to be properly extrapolated. There is no unambiguous

extrapolation procedure within the currently available theoretical models, some of which expect a divergence of g_2 at low x. Since the sum rule validity relies on g_2 obeying Regge theory at low x such a divergence will invalidate it.

The available theoretical OPE-based calculations (see section 1.2.7) predict the sum rules for the second moment of the structure function g_2. The twist-3 matrix element d_3^d can be calculated from the data, using relation 1.58 for $n = 3$ and for a common Q_0^2:

$$d_3^d(Q_0^2) = 2 \int_0^1 dx \ x^2 \left[g_1^d(x, Q_0^2) + \frac{3}{2} g_2^d(x, Q_0^2) \right] \tag{5.11}$$

Using the SMC results on g_1^d and g_2^d scaled at $Q_0^2 = 5$ GeV^2 the value for $d_3^d(Q_0^2)$ only in the measured x interval $0.0015 < x < 0.6$ is:

$$d_3^d(Q_0^2 = 5 \text{ GeV}^2) = 0.0062 \pm 0.0117 \tag{5.12}$$

No attempt was made to extrapolate g_2 in the unmeasured region due the absence of a clear procedure, as outlined above. The value for d_3^d is compatible with the SLAC E143 result, given in table 1.1 ($d_3^d = 0.0039 \pm 0.0092$), within its larger statistical error.

5.5 Conclusions

This thesis presents a description of the measurement of the spin-dependent transverse virtual photon asymmetry A_2^d carried out by the Spin Muon Collaboration at CERN. The results show, that A_2^d is significantly smaller than its positivity bound $|A_2| \leq \sqrt{R}$ in the covered x interval and is compatible with the values obtained by the SLAC E143 collaboration [102] in the overlapping x region. Scaled to a common Q_0^2 and combined together, both results reduce the systematic error on the first moment Γ_1 of the spin-dependent structure function g_1^d by a factor of 5 - from 0.0025 (using the best possible estimate) to 0.0005 - the smallest source of systematic uncertainty on Γ_1^d.

The statistical accuracy of the measurement does not permit to draw conclusions on the interesting subject of higher twist contributions, which carry information on the quark-gluon correlations and quark mass contributions and enter in leading order in the definition of the structure function g_2. The results are compatible with the Wilczek-Wandzura model, which predicts a negligible amount of twist-3 contributions and with the Burkhardt-Cottingham sum rule, which states, that the first moment of g_2 vanishes. In order to test these models a significantly higher, at least a factor of 15, than the SMC statistical sample is necessary.

6 Appendix

6.1 Reconstruction efficiency variations in the SMC spectrometer

For the SMC method of asymmetry extraction, changes of the spectrometer acceptance during measurement create false, unphysical asymmetries, which distort the physics asymmetry. The changes in the acceptance are caused by the unstable reconstruction efficiencies of the detectors. The resulting systematic uncertainty under unfavorable conditions may completely smear out the small physics asymmetry. To avoid contributions from false asymmetries, the experimental apparatus acceptance must be stable for a reasonably large amount of time. The minimum is the duration between two target polarization reversals, which is about 10 hours, more favorable for the analysis is stability in the order of several days. In the SMC spectrometer this goal is achieved by installing big number of detectors with high and constant efficiency and sufficient plane redundancy, more then required by the track reconstruction software. Nevertheless, the fluctuations of the efficiency cannot be completely eliminated and for a certain detector groups they can be of intolerable magnitude, if not appropriate measures are taken.

The types of detectors used in the SMC spectrometer are proportional and drift chambers and streamer tubes. Variations of their efficiency can be created in general by several factors, for example, unstable high voltage supplies, changes of the gas mixture components, electronics readout instabilities, chemical deposits on the sense wires (anode ageing) and changes of the gas density. Electronics components, responsible for the first three factors, have become more reliable during the recent years and in general their parameters are stable within few *ppm*. The ageing processes are difficult to anticipate and control, but are typically slow. On the other hand, the gas density depends on external factors - ambient temperature and atmospheric pressure - both of which can fluctuate in a short time intervals within a wide range and are uncontrollable in SMC. Gas density variations shortens or lengthens the mean free path of the electrons in the ionization avalanche which results in higher or lower signal amplitude on the anode wire. The signal amlitude changes also with the high voltage (HV) applied to the chamber. As high voltage plateau of a chamber one defines that range of HV, in which the signal amplitudes are always above threshold. The lower end of the plateau is the HV, for which signals start to fall below threshold and the upper end is the HV, beyond which the chamber cannot be operated safely any more. Increase or decrease of the HV within the HV plateau does not change the value of the efficiency, therefore there is a flat region (plateau) on the efficiency-HV graph. Normally, the plateauing of a chamber is performed in a short time interval,

during which the external factors are relatively stable and then it only reflects the HV dependence of the signal amplitude. From the measured efficiency curve a HV value is chosen for the detector operation, normally in the middle of the plateau. In reality, the external conditions change with time and this subsequently changes the signal amplitude distribution for a given HV. For the efficiency plateau curve this results in shifting the curve to the left or the right on the same HV scale, without changing its shape. It will be shown later, that the differences of the mean of the amplitude distribution can be as big as 45 % for typical fluctuations of the ambient temperature and atmospheric pressure in the experimental area. This may shift the efficiency plateau so much that the applied voltage is insufficient.

For most of the detectors in the SMC spectrometer the high voltage setting and plane redundancy is such, that they are insensitive as a group to a single plane efficiency fluctuations. There are two detector systems, however, which show strong dependence of the reconstruction efficiency on the change of the HV plateau due to varying gas density - the P123 proportional chambers and the ST67 streamer tubes. In P123 the unstable reconstruction efficiency is due to the low redundancy and the particular plane requirements of the track reconstruction software. In ST67 the problems are due to the necessity to operate the chambers at the lower edge if their HV plateau, otherwise they would age too much.

6.2   Efficiency stabilization system for the ST67 streamer tubes

To adress the problem of the varying chamber efficiencies one has to introduce a system, which is sensitive to the variations of the ambient temperature and pressure and minimizes their effect on the signal amplitude distributions. Such a detector was developed and applied to the ST67 streamer tubes. The original idea came from the CHARM II experiment [111], where similar setup was used for their streamer tubes.

The efficiency stabilization system operates on the principle, that for a given gas density, the amplitude distribution from a wire is constant and depends only on the applied high voltage. Therefore, any changes in the gas density, resulting in a different distribution can be corrected by changing the high voltage. Having a constant distribution results in a stable chamber efficiency, since the readout electronics threshold cut-off is constant. In other words, instead of attaching the operation of the chamber to one high voltage point, it is attached to a constant mean signal amplitude, which determines the efficiency.

Fig.6.1 shows the main components of the stabilization detector. It consists of two streamer tubes of the exact same construction as the ST67 tubes but with only 30 cm length. The signal is read out from the anode wire through a pick-up capacitor and is fed into a CAMAC amplitude to digit converter (ADC). The gate for the ADC is provided by a coincidence between two scintillators, sandwhiching the streamer tubes. The whole system is located close to the ST67 modules in the muon halo and so it experiences essentially the same environmental conditions. A PC-compatible computer reads the ADC via CAMAC. One data gathering cycle consists of recording of a 10000 signals from the streamer tubes 1 and 2. A pedestal is determined by measuring the signal amplitude distributions using a gate from a pulser, which is not correlated with the physics trigger. From the aqcuired distribution the mean amplitude is calculated and after a proper pedestal subtraction it

is compared to a nominal value. A picture of the amplitude distribution with the injected pedestal, the cuts used for the calculation of the mean and its allowed fluctuation is shown in Fig.6.2.
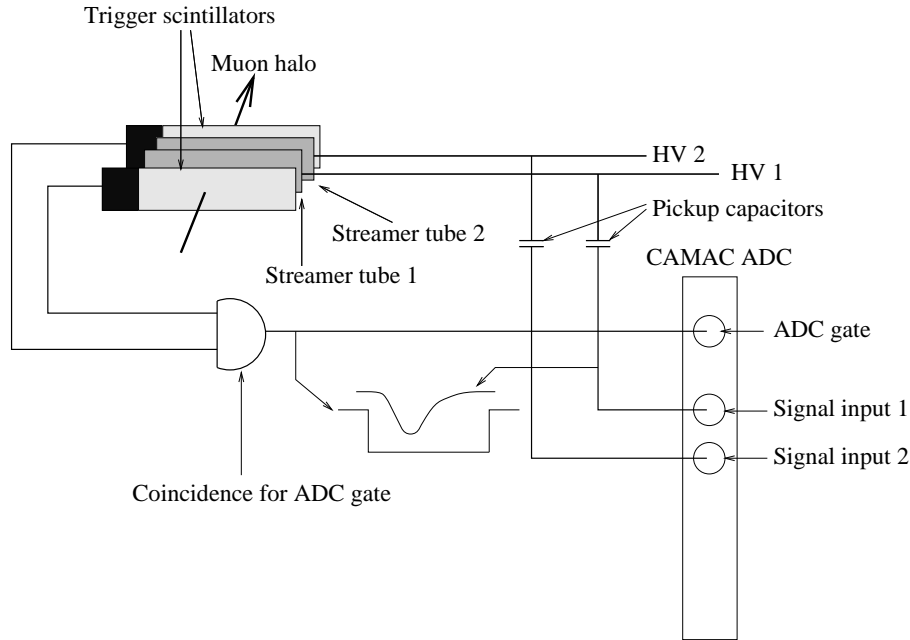

Figure 6.1: *Schematic layout of the efficiency stabilization system for the ST67 streamer tubes detector.*
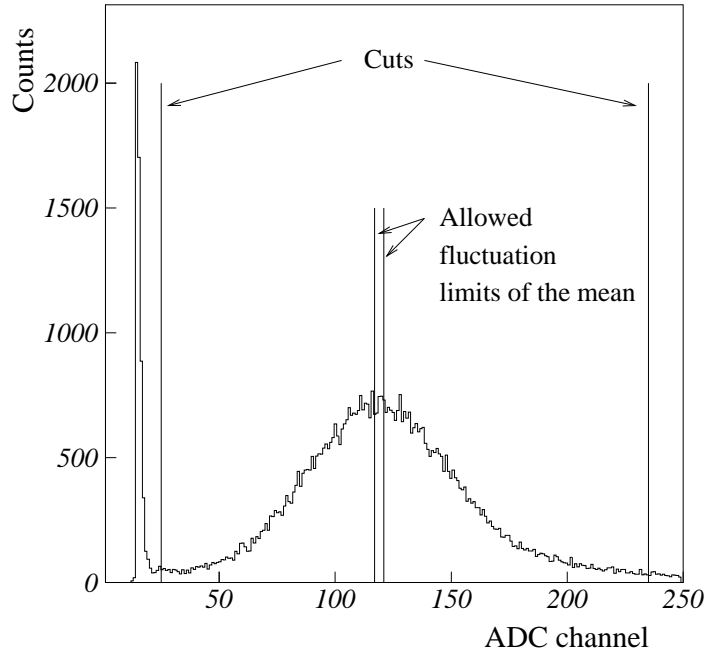

Figure 6.2: *Amplitude distribution from the efficiency stabilization system streamer tube 1. This distribution was used in year 1995 to tune the parameters of the analysis program in terms of nominal value, pedestal position and cuts for the mean value calculation.*

98

If the difference between the mean value of the distribution and the preset nominal value is bigger than 0.8 % in either direction, the PC sends a correction request to the experiments' slow-control computer, together with the difference between the nominal and the measured mean. The slow-control computer calculates and applies a HV correction to the whole ST67 array which causes the mean amplitude to change towards the nominal value. This is done once every 20 minutes. In order to avoid oscillations the applied HV change is only 2/3 of that which would be needed to bring the mean back to the nominal value in one correction cycle. After the proper action is taken, the computer sends an acknowledgment and a new measurement is started on the PC.

Performance of the stabilization system

To show the effect of the stabilization, the influence of temperature and pressure variatons on the amplitude distribution was studied with the same experimental setup, later used for the stabilization system. The studies were done separately for various temperatures (atmospheric pressure is kept constant) and for various pressures (temperature is kept constant). For all measurements the high voltage setting was the same - 4630 V, close to the HV at which the ST67 chambers were operated initially. Limits for the temperature and pressure variations were set by the usual fluctuations of these two variables in the experimental hall. Typically for the pressure it is ± 25 $mbar$ and for the temperature ± 6 $^O C$ around the yearly summer average of 970 $mbar$ and 22 $^O C$ respectively. Resulting distributions for three different overpressures at the same temperature are shown in Fig.6.3(a) and for three different temperatures at the same atmospheric pressure are shown in Fig.6.3(b).
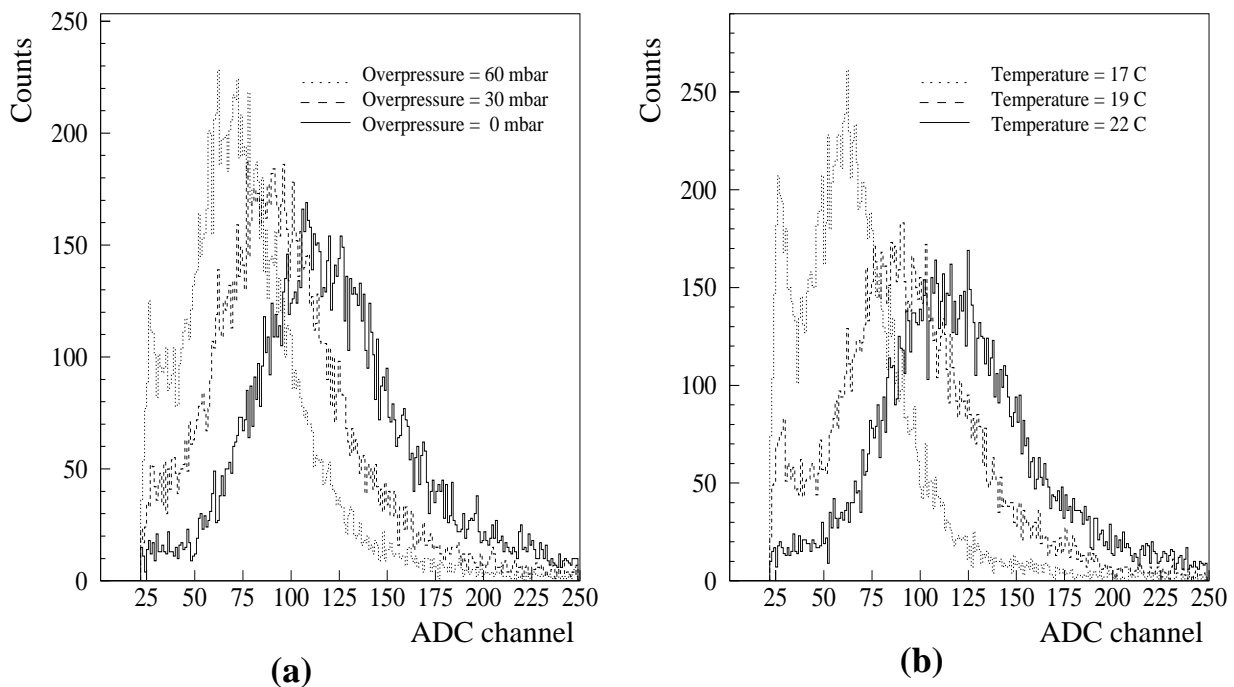

(a) **(b)**

Figure 6.3: *Temperature and pressure dependence of the signal amplitude distributions from the efficiency stabilization system streamer tube 1: (a) different overpressure at constant temperature, (b) different temperatures at constant atmospheric pressure.*

99

The overpressure was varied by closing a needle valve, connected to the gas output of the streamer tube and measured with a precision manometer. The temperature was varied by placing the setup in a isolated box, cooled down with chilled water. It was measured with a digital thermometer, placed inside the streamer tube. A clear trend towards lower amplitudes is seen on the histograms as the pressure increases or the temperature decreases. 50 $mbar$ pressure increase results in 35 % decrease in the mean amplitude, temperature drop of 5 ^{O}C results in 45 % decrease. The effect of such variations on the efficiency of the ST67 detector, if operated at constant high voltage are considerable.

Since the introduction of the stabilization system, there were no visible changes due to the weather on the detector efficiency. Fig.6.4 shows the efficiency of the detector, evaluated with the track reconstruction software, together with the variations of the temperature, atmospheric pressure and the high voltage adjustments. These parameters are plotted versus time and cover the period P2E95 (19 days of data taking). Plots for other time periods show similar behaviour. The last 250 hours of the period are characterized by stable atmospheric pressure, therefore the HV adjustment closely follows the temperature fluctuations. One can see, that the HV variation is as big as 115 V. The resulting plane efficiency variation in case of constant gas density, estimated from the ST67 plateau curve (Fig.2.13) at the mean high voltage for the period 4635 V is about $6-7$ %, which results in approximately $3-3.5$ % variation of the overall ST67 track reconstruction efficiency. The same efficiency variation is expected for constant HV 4635 V and the gas density varying as observed. The variation is avoided, because of the feedback loop. The efficiency is stabilized by the system to better than 1 %, which has been shown in [112] to be sufficient for the stability requirements of the experiment.

Several security features are built into the setup in order to prevent it from misadjusting the high voltage. The correct performance of the monitor tube is ensured by comparing its response to that of the control tube. A minimum amount of 10000 events collected in a 10 minute time interval is required for the amplitude distribution. The absolute pedestal position is monitored and compared to a distribution from a constant current generator. In case of incorrect measured values of any of the abovementioned parameters, no adjustment is attempted and a warning is send to the experiment operator. As a final precaution, if all of the safety features fail to detect eventual problem, a minimum and maximum high voltage limits are imposed on the HV power supply.

The successful performance of the efficiency stabilization system for the ST67 detector led to the implementation of a second similar system for the P123 magnet chambers.
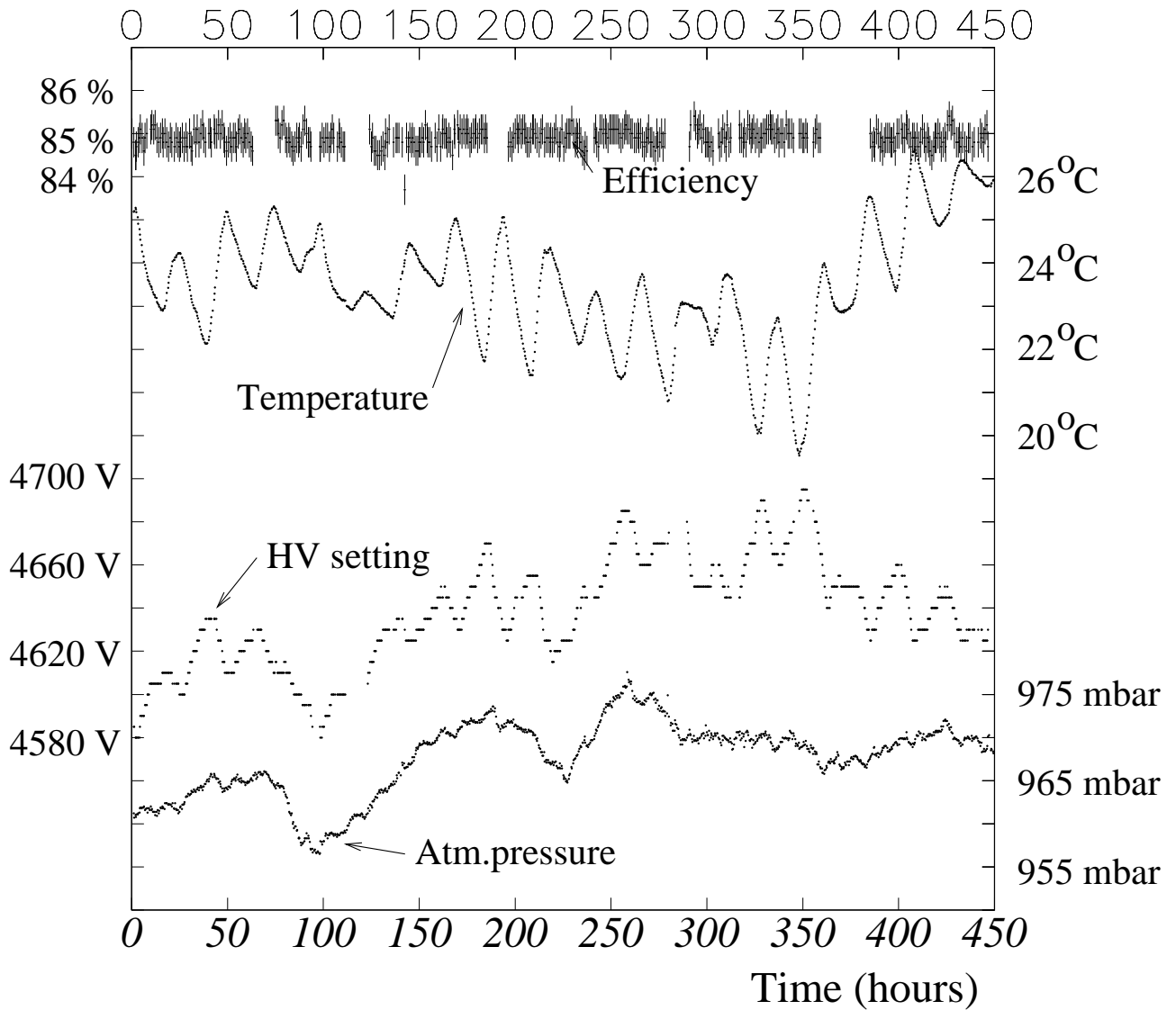
Figure 6.4: *Summary of the ST67 efficiency stabilization system operation for the period P2E95. The efficiency of the detector and the HV setting are on the left axis, the ambient temperature and atmospheric pressure are on the right axis.*

6.3 Efficiency stabilization system for the P123 chambers

The setup used to stabilize the P123 detector efficiency is based on the same principle as for the ST67 stabilization. A special monitor chamber with identical parameters as the magnet chambers was built. It has the same anode wire spacing and diameter and

cathode gap. The chamber was placed in the FSM, only 20 cm downstream from the module P3. This is necessary, since the temperature in the magnet is about $6^{\circ}C$ higher than in the rest of the hall and has a different fluctuation cycle.

Placing the chamber in the strong magnetic field of the FSM makes it difficult to use a standard scintillation detector trigger. Therefore a ^{55}Fe radioactive γ-source was used as an event and trigger source at the same time. Two of the wires from the monitor chamber are connected to a fast analog amplifiers. The signal from one of the wires is split after the amplifier through a linear fan-out. One of the outputs of the fan-out is fed directly to a CAMAC ADC, the other is amplified $10\times$, discriminated and delayed and provides a signal gate for the ADC. The data acquisition from the ADC is performed by the same PC-compatible as for the ST67 system. 7-minute data sampling provides ≈ 25000 events for a signal amplitude distribution. A pedestal is injected into the distribution, using a high frequency pulser, uncorrelated with the ^{55}Fe events. After applying cuts, the mean of the distribution is calculated and its value with subtracted pedestal is compared to a preset nominal mean. If the measured value differs by more than 1.5 % from the nominal value, the high voltage of the system is increased or decreased in steps of 5 V, until the difference is compensated. The comparison cycle and HV adjustment are repeated each 20 minutes.

Events from the radioactive source induce signal only on one wire at a time, allowing the use of the second wire as a filter for correlated noise. Any signal from this wire, coinciding in time and having the same polarity (electronics pickup) shuts down the ADC gate. Additional safeguard against distortions in the spectra is collecting data only in the pauses between the muon spill, since the charge deposit from muons disturbes the measurement.

Typical signal amplitude distribution from one datataking cycle is shown in Fig.6.5(a), together with the injected pedestal and the applied cuts.

Prior to the installation of the monitor chamber in the FSM, series of tests were done to determine the mean of the distribution correlation to external factors - temperature and pressure. The setup had a better handle on the pressure measurement. The chamber was overpressured through its gas supply up to 60 $mbar$ over the atmospheric pressure. For each overpressure point an amplitude distribution was obtained and its mean value calculated. At the same pressure point, the HV of the system was raised, until the mean of the distribution became equal to the initial mean at overpressure 6 $mbar$. All measurements were done in a short time interval, about 1 hour, thus assuring a constant temperature and atmospheric pressure. In this way, the relation between the pressure and the compensating HV was measured. It is shown in Fig.6.5(b). For the overpressure of 50 $mbar$, the compensating HV is 120 V, which corresponds to a plane efficiency change of the magnet chambers array of 5%. According to the study, presented in [70], with the magnet setup using only three chambers, this corresponds to a change of the value of the first moment of the structure function g_1 - Γ_1 of $\approx 2\%$ - the biggest single source of systematic error in the experiment. Of course, it is unlikely to have such a dramatic fluctuations of the external factors. Reasonable scenarios, with a duration of one configuration for the asymmetry calculation (about 10 hours), predict that the effect of the pressure and the temperature on the efficiency of the magnet chambers will yield an effect on the value of Γ_1 of $\approx 0.2\%$, which is still one of the biggest systematic errors.

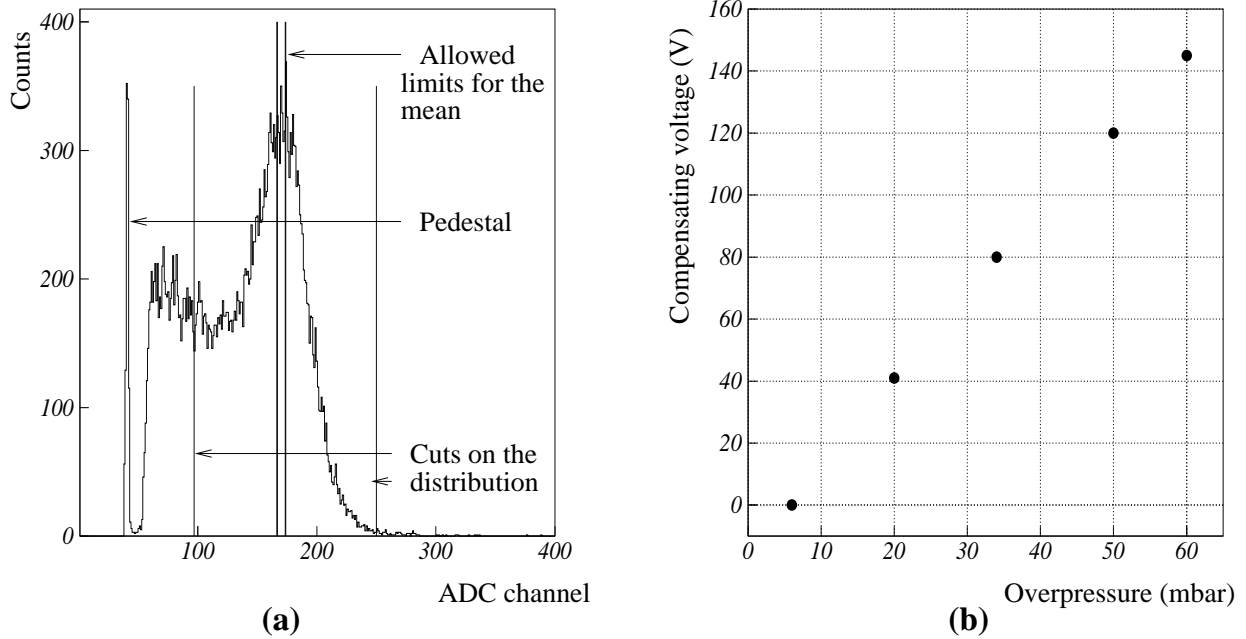**(a)**   **(b)**

Figure 6.5: $(a)^{55}Fe$ *signal amplitude distribution from the monitor chamber of the magnet efficiency stabilization system. The injected pedestal and the lower and upper cuts on the spectrum are also on the picture. The magnet chambers are operated in the region of limited proportionality, therefore the spectrum does not show the separation between the 5.9keV and the 6.4keV ^{55}Fe peaks.*
(b)High voltage needed to compensate the overpressure applied to the gas system of the monitor chamber.

After the installation of the fourth chamber (P1B), the redundancy of the magnet chambers array became sufficient, such that the total reconstruction efficiency does not depend on the changes in the plane efficiencies for the duration of one configuration. This way, the effect of the efficiency stabilization performed by the system becomes invisible, however it assures higher security in case of a malfunction of one of the chambers. In such event, the data taking may continue, until a suitable pause in the beam, for example an accelerator maintenance, during which the chamber can be repaired.

Figure 6.6 shows a summary performance plot of the efficiency stabilization system for the P123 chamber array for the data taking period P2E95. The sharp temperature decrease, observed around 62 hours, 120 hours and 280 hours are due to the FSM being switched off for periods with no data taking or for alignment and calibration runs.
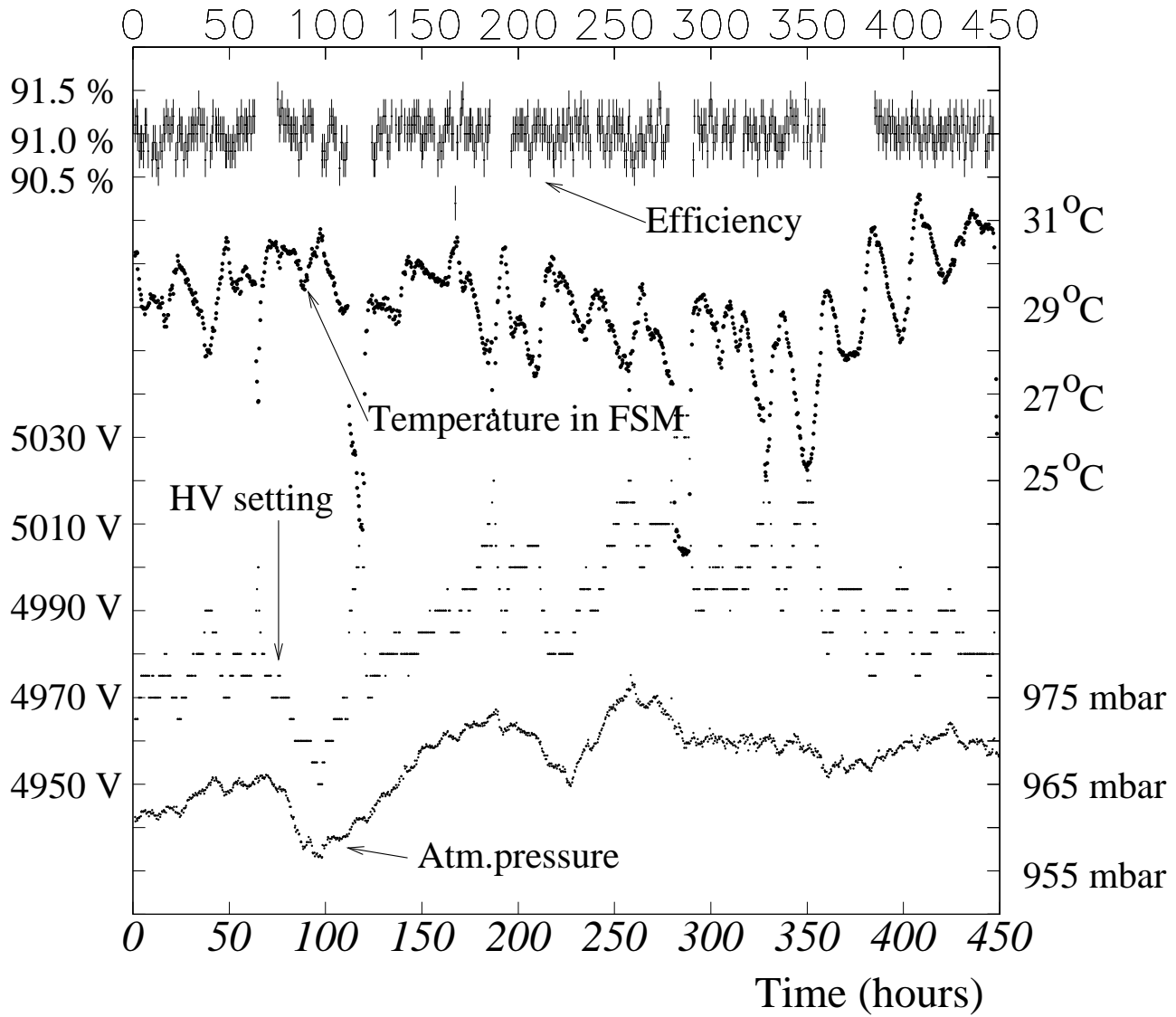
Figure 6.6: *Summary of the P123 efficiency stabilization system operation for the period P2E95. The efficiency of the detector and the HV settings are on the left axis, the ambient temperature and atmospheric pressure are on the right axis.*

Acknowledgements

First and foremost I would like to thank my thesis advisor, Professor Arnold Staude, for giving me the opportunity to participate in a modern physics experiment - the Spin Muon Collaboration and teaching me the intricacies of detector operation and physics analysis.

Dr. Alain Magnon and Dr. Gerhard Mallot, our two contactmen, have put an enormous effort and dedication to coordinate the experiment and make it such a success, both during the data taking and as physics results. My work with them was a pleasure and a real learning experience.

Jens Vogt, my fellow student, demonstrated without a shadow of a doubt, that there is no computer system wich cannot be crashed and restarted time and again, without losing the readiness for a coffee and the presence of mind. Under his competent supervision the SUN computer cluster operated without a glitch for everybody.

The strong presence and efforts of my colleagues Mayda Velasco, Axel Steinmetz, Matthias Grosse Perdekamp, Damon Fasching and all other SMC students Akio, Andreas, Brian, Chris, Ernst, Gonzalo, Juan, Jörg, Lucas, Maarten, Miguel, Naoki, Peter, Steve, made the work at any time meaningful and pleasant.

Always ready to answer questions and discuss physics were Dr. Ricardo Piegaia and Dr. Ulrich Stiegler.

My special thanks to Matthias Haase and Horst Herbert for making important parts of the spectrometer operate flawlessly by their great ability to design and construct complex equipment in extremely short time.

This work is dedicated to Boriana, for her love and understanding.

7 Summary

This thesis presents the work on the extraction of the transverse spin asymmetry A_2 in muon-deuteron deep inelastic scattering by the Spin Muon Collaboration (SMC). The analysis is based on data with longitudinally polarized muon beam and transversely polarized deuteron target.

The main goals of the SMC are to measure with high precision the structure functions $g_1(x, Q^2)$ of the proton and the neutron (through the deuteron) and the first moments of these structure functions $\Gamma_1 = \int g_1(x) \mathrm{dx}$. During the evaluation of these moments, it was realized, that the dominant systematic error is due to the unknown magnitude of the asymmetry A_2, which enters in the calculation of the structure function g_1 through the relation:

$$g_1 = \frac{F_1}{1 + \gamma^2}(A_1 + \gamma A_2)$$

The best possible estimate of the contribution of A_2, without a direct measurement is through the positivity limit $|A_2| \leq \sqrt{R}$. Calculated in this way, the systematic error on the integral $\Gamma_1 = \int g_1(x) \mathrm{dx}$ due to A_2 is 0.0041, whereas the total systematic error is 0.0142.

A primary objective of the measurement of the transverse spin asymmetry is to reduce considerably this error source. The results from the measurement, presented in this work, show that the asymmetry A_2^d is much smaller, than its positivity limit and throughout the measured interval in x ($0.0015 < x < 0.6$) is compatible with zero. Using these results brings the contribution of A_2^d to the error on the moment Γ_1^d to 0.0011 and a combination of the SMC results with a measurement from the SLAC E143 experiment allows for a further reduction to a value of 0.0005, a factor of 8 gain from the initial contribution. Thus the value of the systematic error, due to the neglect of A_2 becomes the smallest systematic error on the first moment Γ_1^d of the structure function g_1^d.

A comparison of the structure function g_2^d, evaluated from the asymmetry A_2^d to the exsisting theoretical models - Wilczek-Wandzura realtion, Burkhard-Cotthingam sum rule - shows that although in the measured interval it is compatible with zero and therefore within the model expectations, the predictive power, especially at low x is insufficient. In order to investigate the magnitude of the tranverse spin effects on g_2, the statistical sample would have to be increased at least a factor of 15, which will make it equivalent to the sample used to evaluate the structure function g_1.

Bibliography

[1] M. Breidenbach *et al.*, Phys. Rev. Lett. **23** (1969) 935.

[2] B. D. Bjorken, Phys. Rev. **179** (1969) 1547.

[3] M. Gell-Mann, Phys. Lett. **8** (1964) 214.
G. Zweig, **CERN-TH/401** (1964), **CERN-TH/412** (1964).

[4] J. Ellis, R. L. Jaffe, Phys. Rev. **D 9** (1974) 1444; Phys. Rev. **D 10** (1974) 1669.

[5] M. J. Alguard *et al.* Phys. Rev. Lett. **37** (1976) 1261.

[6] G. Baum *et al.* Phys. Rev. Lett. **51** (1983) 1135.

[7] D. L. Antony *et al.* Phys. Rev. Lett. **71** (1993) 959.

[8] K. Abe *et al.* Phys. Rev. Lett. **74** (1995) 346; Phys. Rev. Lett. **75** (1995) 25.

[9] R. D. Ball, S. Forte, G. Ridolfi, Phys. Lett **B378** (1996) 255.

[10] M. Glück, E. Reya, M. Stratmann, W. Vogelsang, Phys. Rev **D53** (1996) 4775.

[11] T. Gehrmann, W. S. Stirling, Phys. Rev **D53** (1996) 6100.

[12] F. E. Close, 'An Introduction to Quarks and Partons', Academic Press, London (1979).

[13] D. Griffiths, 'Introduction to Elementary Particles', John Willey & Sons, New York (1987).

[14] A. V. Manohar, UCSD/PTH 92-10 (1992).

[15] C. Itzykson, J. B. Zuber, 'Quantum Field Theory', McGraw-Hill, New York (1980).

[16] U. Stiegler, SMC internal note, **SMC/94/18** (1994).

[17] P. Hoodbhoy, R. L. Jaffe, A. Manohar, Nucl. Phys **B312** (1989) 571.

[18] C. G. Callan, D. Gross, Phys. Rev. Lett. **22** (1969) 156.

[19] The NMC, P.Amaudruz *et. al.*, Phys. Lett. **B295** (1992) 159 and **CERN-PPE/92-124**.

[20] L. W. Whitlow *et. al.*, Phys. Lett. **B295** (1990) 193.

[21] Donald H. Perkins, 'Introduction to High Energy Physics', 2-nd edition, Adison-Wesley Publishing Company, Inc. (1982).

[22] U. Stiegler, Habilitationsschrift, (1995).

[23] G. K. Mallot, Habilitationsscrhift, (1996).

[24] M. G. Doncel, E. de Rafael, Nuovo Cimento **4A** (1971) 363.

[25] M. Lacombe *et. al.* Phys. Rev. **179** (1980) 861.

[26] R. P. Feynman, Phys. Rev. Lett. **23** (1969 1415.

[27] B. D. Bjorken, E. A. Paschos, Phys. Rev. **185** (1969) 1975.

[28] G. L. Kane, J.Pumplin, W. Repko, Phys. Rev. Lett. **41** (1978) 1689.

[29] B. L. Ioffe, V. A. Khoze, L. N. Lipatov, 'Hard Processes' (North-Holland, Amsterdam, 1984) Vol. 1.

[30] A. V. Efremov, O. V. Teryaev, Yadr. Fiz. **39** (1984) 1517.

[31] M. Anselmino, A. Efremov, E. Leader, Phys. Rep. **261** (1995) 1.

[32] R. P. Feynman, 'Photon-Hadron Interactions' Benjamin, Reading, MA, 1972.

[33] R. G. Roberts, G. G. Ross, Technical report **RAL-TR-95-057** (1995).

[34] R. L. Jaffe, X. Ji, Phys. Rev. **D43** (1991) 724.

[35] K. G. Wilson, Phys. Rev. bf 179 (1969) 1499.

[36] J. Kodaira, Y. Yasui, T. Uematsu, Preprint KUCP-71 HUDP-9411 (1994).

[37] S. A. Larin, CERN preprint, **CERN-TH-7208/94** (1994).

[38] E. Stein *et al.*, UFTP preprint 366 (1994).

[39] I. I. Balitsky, V. M. Braun, A. V. Kolesnichenko, Phys. Lett. **B242** (1990) 245, (Erratum) **B318** (1994) 684.

[40] X. Song, J.S. McCarthy, Phys. Rev. **D49** (1994) 3169.

[41] M. Stratmann, Z. Phys. **C60** (1993) 763.

[42] S. Wandzura, F. Wilczek, Phys. Lett. **B72** (1977) 195.

[43] H. Burkhardt, W. N. Cottingham. Ann. Phys. **56** (1970) 453.

[44] R. L. Heimann, Nucl. Phys. **B64** (1973) 429.

[45] A. V. Efremov, O. V. Teryaev, Sov. J. Nucl. Phys. **39** (1984) 962.

[46] K. Abe *et al.*, SLAC-PUB-95-6982 (1995).

[47] M. Arneodo (Thesis) , Princeton University (1992).

[48] R. Clifft and N. Doble, CERN Preprint, **SPSC/74-12** (1974).

[49] R. Piegaia (Thesis), Yale University (1988).

[50] The Spin Muon Collaboration (SMC), NIM **A343** (1994) 363.

[51] D. Brahy and E. Rossa, **CERN-SPS/EA/78-11** (1978).

[52] I. G. Bird (Thesis), Vrije Universiteit Amsterdam (1992).

[53] L. Klostermann (Thesis), Delft University (1995).

[54] S. Bültmann (Thesis), Bielefeld University (1996).

[55] N. Hayashi (Thesis), Nagoya University (1994).

[56] C. M. Dylua (Thesis), UCLA (1996).

[57] D. Krämer, NIM **A356** (1995)79.

[58] Yu. Kisselev, T. Niinikoski, **CERN-PPE/96-146** (1996).

[59] J. Kyynäräinen, C. Özben, SMC internal note, **SMC/95/42** (1995).

[60] D. Krämer, SMC internal note, **SMC/95/32** (1995).

[61] W. de Boer, CERN Yellow report, **CERN/74-11** (1974).

[62] W. Flauger, **CERN-EP/79-25** (1979).

[63] F. Sever, P. Shanahan, SMC internal report, **SMC/92/16** (1992).

[64] U.Stiegler, SMC internal report, **SMC/95/15** (1995).

[65] R. P. Mount, NIM **187** (1981) 401.

[66] Kjell Janson (Thesis), Uppsala (1991).

[67] D. Miller, M. Velasco, R. Windmolders, private communication.

[68] J. B. Lindsay *et al.*, **CERN 74-12** (1974).

[69] C. Best and A. Osborne, EMC internal report, **EMC/78/26**.

[70] M. Velasco (thesis), Northwestern University (1995).

[71] M. G. Perdekamp (thesis), UCLA (1995).

[72] L. Van Konigsveld, H. Verweij and V. Senko, Documentation of the D.T.R System, **CERN-EP/247-A4** (1977).

[73] L. Pinsky, ST67 Readout Electronics writeup (1994).

[74] CAEN Short form Catalog, CAEN(1995) 56.

[75] CAEN Short form Catalog, CAEN(1995) 28.

[76] M. Haase and R. Sinha, HV system for P67 (report) (1993).

[77] P. Ponting, CERN preprint, **CERN EP/80-01** (1980).

[78] C. Iselin, HALO simulation, **CERN Yellow report/74-17** (1974).

[79] N. Doble *et al.*, NIM **A343** (1994) 351.

[80] K. L. Brown *et al.*, TRANSPORT, **CERN Yellow report/80-04** (1980).

[81] L. Michel, Proc. Phys. Soc. **A63** (1950) 514

[82] C. Bouchiat, L. Michel, Phys. Rev **106** (1957) 170

[83] S. Eichblatt (thesis), RICE university (1996).

[84] F. Marie (thesis), Univ. Claude Bernard Lyon I (1994).

[85] The SMC (B. Adeva *et al.*), NIM **A343** (1994) 363.

[86] W. Brefeld *et al.* Nucl. Inst. and Meth. in Phys. Res. 228 (1985) 228; J. Arrington *et al.*, NIM **A311** (1992) 39.

[87] A. M. Bincer, Phys. Rev. 107 (1957) 1434.

[88] E. Burtin (thesis), Universite de Paris-Sud, U.F.R scientifique d'Orsay (1996).

[89] NA47 Zebra banks, **SMC/92/4** (1992).

[90] A. Steinmetz (thesis), Johannes-Gutenberg-Universität Mainz (1996).

[91] P. Shanahan (thesis), Northwestern university, Evanston Il (1995).

[92] M. Rodriguez (thesis), Universidad de Santiago de Compostela, Spain (1994).

[93] N. de Botton, SMC internal note, **SMC/94/1** (1994).

[94] The NMC (P. Amaudruz *et. al.*), Nucl. Phys. **B371** (1992) 3.

[95] The NMC (P. Amaudruz *et. al.*), Nucl. Phys. **B441** (1995) 3.

[96] The NMC (M. Arneodo *et. al.*), Nucl. Phys. **B441** (1995) 12.

[97] The E-139 collaboration (J. Gomez *et. al.*), Phys. Rev. **D49** (1994) 4348.

[98] A. Akhundov, D. Bardin, N. Shumeiko, Sov. J. Nucl. Phys. **26** (1977) 660 and **44** (1986) 988.

[99] The SMC (D. Adams *et. al.*, Phys. Lett **B369**(1997) 338.

[100] E143 Collaboration (K. Abe *et. al.*, Phys. Lett **B364**(1995) 61.

[101] L. W. Withlow *et. al.*, Phys. Rev. Lett. **B250** (1990) 193.

[102] E143 Collaboration, K. Abe *et. al.*, Phys. Rev. Lett. **76** (1996) 587.

[103] G. Altarelli, P. Nason and G. Ridolfi, Phys. Lett. **B320** (1991) 152.

[104] The SMC (B. Adeva *et. al.*, Phys. Lett. **B302** (1993) 533.

[105] The SMC (D. Adams *et. al.*) Phys. Lett. **B336** (1994) 125.

[106] The SMC (D. Adams *et. al.*) Phys. Lett. **B329** (1994) 399.

[107] The SMC (D. Adams *et. al.*) Phys. Rev. **D56** (1997).

[108] The SMC (D. Adams *et. al.*) Phys. Lett. **B357** (1995) 248.

[109] T. V. Kukhto, N. M. Shumeiko, Nucl. Phys **B219** (1983) 412
I.V. Akushevich, N. M. Shumeiko, J. Phys. **G20/4** (1994).

[110] The COMPASS collaboration, Proposal, CERN/SPSLC/96-14.

[111] A. Staude, J. Vogt, Private communication and
J. Vogt, Diplomarbeit, LMU München (1991).

[112] J. Saborido (thesis), Universidad de Santiago de Compostela, Spain (1996).

[113] CMZ Manual, CodeME S.A.R.L, St. Genis (1991).

[114] CERN Program Library Long Writeups **I102** (1991).

[115] CERN Program Library Long Writeups **Q100/Q101** (1993).

Curriculum Vitae

Latchezar Betev

Personal information:

Born 22/06/1966 in Sofia, Bulgaria

Married, 1 child

Parents: Mother: Vera Nikolaeva Karabacheva, Father: Botio Lalev Betev

Education:

1973-1981	Primary school, Sofia, Bulgaria
1981-1994	Secondary school, Sofia, Bulgaria Grade: excellent
1986-1991	Sofia University 'Kiril and Metodii', Physics faculty, Sofia, Bulgaria
	Academic qualification: Master of science; Diploma work grade: excellent

Research positions:

1992-1996	Ludwig-Maximilians-Universität München, Wissenschaftlische
.	Angesteller, work on spin-dependent structure functions.
1997-2000	University of California, Los Angeles, Research associate, work on
.	particle yield measurements in p+p, p+A and Pb+Pb reactions.
2001-present	Institut Für Kernphysik, Frankfurt, Research associate, work on
.	particle yield measurements in p+p, p+A and Pb+Pb reactions.